



MARMARA UNIVERSITY
INSTITUTE FOR GRADUATE STUDIES
IN PURE AND APPLIED SCIENCES



**SYNTHESIS AND CHARACTERIZATION
OF MAGNETIC PHOTOCATALYSTS FOR
HYDROGEN GENERATION**

SEDA YILMAZ

MASTER THESIS

Department of Chemical Engineering

Thesis Supervisor

Prof. Dr. Atıf Koca

Thesis CO- Supervisor

Doç. Dr. Özge Kerkez Kuyumcu

ISTANBUL, 2019



MARMARA UNIVERSITY
INSTITUTE FOR GRADUATE STUDIES
IN PURE AND APPLIED SCIENCES



**SYNTHESIS AND CHARACTERIZATION OF
MAGNETIC PHOTOCATALYSTS FOR
HYDROGEN GENERATION**

SEDA YILMAZ

(524516011)

MASTER THESIS

Department of Chemical Engineering

Thesis Supervisor

Prof. Dr. Atıf Koca

Thesis CO- Supervisor

Doç. Dr. Özge Kerkez Kuyumcu

ISTANBUL, 2019

MARMARA UNIVERSITY
INSTITUTE FOR GRADUATE STUDIES IN PURE AND
APPLIED SCIENCES

Seda YILMAZ, a Master of Science student of Marmara University Institute for Graduate Studies in Pure and Applied Sciences, defended his thesis entitled “**Synthesis and Characterization of Magnetic Photocatalysts For Hydrogen Generation**”, on June 24, 2019 and has been found to be satisfactory by the jury members.

Jury Members

Prof. Dr. Atif KOCA (Advisor)

Marmara University(SIGN)

Assistant Prof Dr. Yaşar Andelip AYDIN (Jury Member)

Marmara University(SIGN)

Assistant Prof Dr. Gülşen ALBAYRAK ARI (Jury Member)

Istanbul University(SIGN)

APPROVAL

Marmara University Institute for Graduate Studies in Pure and Applied Sciences Executive Committee approves that Seda YILMAZ be granted the degree of Master of Science in Department of Chemical Engineering, Chemical Engineering Program on June 26 2019. (Resolution no: 2019/13-02)

Director of the
Institute Prof. Dr. Adı

Prof. Dr. Bulent EKICI
Enstitü Müdürü

MARMARA ÜNİVERSİTESİ
FEN BİLİMLERİ ENSTİTÜSÜ

Marmara Üniversitesi Fen Bilimleri Enstitüsü Yüksek Lisans Öğrencisi Seda YILMAZ'ın "Synthesis and Characterization of Magnetic Photocatalysts For Hydrogen Generation" başlıklı tez çalışması, 24 Haziran 2019 tarihinde savunulmuş ve jüri üyeleri tarafından başarılı bulunmuştur.

Jüri Üyeleri

Prof. Dr. Atıf KOCA

(Danışman)

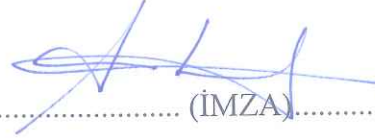


Marmara Üniversitesi

(İMZA).....

Dr. Öğr. Üyesi Yaşar Andelip AYDIN

(Üye)



Marmara Üniversitesi

(İMZA).....

Dr. Öğr. Üyesi Gülşen ALBAYRAK ARI (Üye)

İstanbul Üniversitesi

(İMZA).....



ONAY

Marmara Üniversitesi Fen Bilimleri Enstitüsü Yönetim Kurulu'nun ²⁶06/2019 tarih ve ^{2019 / 13.02} sayılı kararı ile Seda YILMAZ'ın Kimya Mühendisliği Anabilim Dalı, Kimya Mühendisliği Programında Yüksek Lisans derecesi alması onanmıştır.

Fen Bilimleri Enstitüsü Müdürü

Prof. Dr. Adı SOYADI

ACKNOWLEDGEMENT

I would like to thank to Allah to help me finishing my work possible. In this work, several people helped me during my research. And I am really grateful for their contributions to this study.

Firstly, I am truly indebted to my supervisor, Prof. Dr. Atif KOCA, for his support, guidance, helpful criticism, suggestion and helpful supports in all possible ways throughout this research.

I am really thankful my second supervisor, Özge KERKEZ KUYUMCU, valuable guidance, supportive reviews, complementary thoughts and spent her time for my study, withstand my indecision and I will always be indebted to her.

Many thanks to my guiding friend and teacher Ms.Duygu AKYÜZ for her illuminating ideas, unpredictable recommendations and I never forget the moments her supported me in the unpredictable point. I am really appreciative to her for helping me about my research and for her time which spent for me.

I also would like to thank “The Scientific and Technological Research Council of Turkey, (TUBITAK) for their financial help and support under the Project number 116M567 titled as “Photoelectrochemical-Photocatalytic Hydrogen Evolution Reactions (PEPCHER)” for Pure Hydrogen Production. My dearest gratitude to my team which includes Prof. Dr. Atif KOCA, Prof. Dr. Cevat SARIOĞLU, Prof. Dr. Fatma KARACA, Ms. Duygu AKYÜZ, Rana Muhammad Zunain Ayaz, Irem TANIŞIK, Özlem UĞUZ.

I sincerely thank my colleague and friend all throughout the thesis process worked with me and helped me in every moment, supporting me every step in my study, Rana Muhammad Zunain AYZ, I am sincerely thankful to him. I truly owe him a lot to complete my research and I can never forget.

Finally, I would like to thank to my mother Ms. Birgül YILMAZ and my father Mr. Faruk YILMAZ, who architected my career and are always consistent source of motivation for me and their prayers always helped me supported me whenever I am in the hour of need.

June, 2019

Seda YILMAZ

TABLE OF CONTENTS	
ACKNOWLEDGEMENT	ii
TABLE OF CONTENTS	iii
LIST OF SYMBOLS	v
LIST OF ABBREVIATIONS	vi
LIST OF FIGURES	vii
ABSTRACT	x
1 INTRODUCTION.....	14
1.1 HETEROGENEOUS PHOTOCATALYSIS FOR ENERGY AND ENVIRONMENT PROBLEMS	15
1.2 ALTERNATIVE ENERGIES AND HYDROGEN	17
1.2.1 Hydrogen Production Methods.....	19
• Hydrogen Production from Fossil Fuels	19
• Hydrogen Production from Renewable Sources	20
1.3 PHOTOCATALYTIC WATER SPLITTING	21
1.4 PHOTELECTROCHEMICAL WATER SPLITTING.....	23
1.4.1 Basic Working Principle of Photoelectrochemical Cell Mechanism	24
1.4.2 Basic Factor That Affecting the Photo-electrochemical Water Splitting .	25
• Crystallinity	25
• Temperature	25
• Size	25
• Band Gap.....	26
• pH Dependency	26
• Light	26
1.4.3 Activity Calculations	26
1.5 PHOTOCATALYSTS FOR WATER SPLITTING.....	27
1.5.1 UV Light Active Photocatalysts	27
1.5.2 Visible Light Active Photocatalysts	28
1.5.3 Magnetic Photocatalysts	31
1.6 PHOTOCATALYTIC DYE DEGRADATION	33
1.6.1 Effect of the Working Parameters	35
1.7 LITERATURE REVIEW	36

2	MATERIALS AND METHOD.....	39
2.1	MATERIALS.....	39
2.1.1	Materials for Preparation of Photocatalysts.....	39
2.1.2	MaterialsforMethylene Blue Degradation.....	39
2.1.3	Materials for Photoelectrochemical Measurements.....	39
2.2	METHOD.....	40
2.2.1	The Fabrication of Core Composites.....	40
2.2.2	The Fabrication of Fe ₃ O ₄ @TiO ₂ Composites.....	41
2.2.3	The Fabrication of NiFe ₂ O ₄ @TiO ₂ Composites.....	42
2.2.4	X-Ray-Diffraction Analysis.....	43
2.2.5	UV-Visible Diffuse Reflectance Spectroscopy (UV-DRS) Analysis.....	43
2.2.6	Scanning Electron Microscopy Analysis (SEM).....	44
2.2.7	Energy Dispersive X-Ray Spectroscopy (EDS) Analysis.....	44
2.2.8	Raman Spectroscopy Analysis.....	45
2.2.9	Photoelectrochemical Activity Measurements.....	46
2.2.10	Photocatalytic Methylene Blue Degradation Analysis.....	48
3	RESULTS AND DISCUSSON.....	51
3.1	X-Ray Diffraction (XRD) Analysis Results.....	51
3.2	UV-Visible Diffuse reflectance Analysis Results.....	54
3.3	Scanning Electron Microscopy (SEM) Analysis Results.....	58
3.3.1	Energy Dispersive X-Ray Spectroscopy (EDS) Analysis.....	60
3.4	Raman Spectroscopy Results.....	61
3.5	Photoelectrochemical Activity Measurement Results.....	64
3.5.1	Linear Sweep Voltammetry Results.....	66
3.5.2	Chronoamperometry Analysis Results.....	68
3.5.3	Mott-Schottky Analysis Results.....	69
3.6	Photo-catalytic Methylene Blue Degradation Results.....	72
4	CONCLUSION.....	78
	REFERENCES.....	84
	ÖZGEÇMİŞ.....	89

LIST OF SYMBOLS

C_{MB} : Methylene Blue Concentration (mole/L)

C_{MB_0} : 0. time methylene blue concentration (mol/L)

C_{MB_t} : Methylene blue concentration at time t (mole/L)

$^{\circ}C$: Degree Celsius

E_{fb} : Flat Band Potential

E^0 : Reduction Potential

e_{CB}^- : Produced electron charge at conduction band

E_g : Band Gap Energy (eV)

h : Planck Constant

h_{VB}^+ : Produced hole charge at valence band

k : Reaction rate constant

MPa: Mega Pascal Pressure

M: Molarity

η : H₂ production efficiency

R: Reflectance

R^2 : Correlation Coefficient

t: Time

T: Temperature

ν : Frequency

LIST OF ABBREVIATIONS

CB: Conduction Band

EDS: Energy Dispersive X-Ray Spectroscopy

FWHM: Full Width Half Maximum

ITO: Indium Titanium Oxide glass substrate

IR: Infrared Region

MB: Methylene Blue

PEC: Photoelectrochemical Cell

RHE: Reference Hydrogen Electrode

RhB: Rhodamine

SEM: Scanning Electron Microscopy

TEA: Triethanoleamine

TISOP: Titanium iso propoxide

UV: Ultraviolet Region

XRD: X-Ray Diffraction

V: Voltage

VB: Valence Band

LIST OF FIGURES

Figure 1.1: Scope of Heterogeneous Photocatalysis Applications.....	16
Figure 1.2: Illustration of basic scheme of photosynthesis and photocatalytic water splitting as artificial photosynthesis[11].	17
Figure 1.3: Distribution of the Hydrogen Production Resources for Conventional Production Method[13].....	18
Figure 1.4: a) Schematic illustration of water splitting process to generate hydrogen under solar energy[11]; b) The basic principle of photocatalytic water splitting on photocatalyst surface[19]	22
Figure 1.5: Photocatalytic water splitting principle on top of the semiconductor surface	23
Figure 1.6: Schematic diagram of the photoelectrochemical cell reactions.....	25
Figure 1.7: Band edge positions some of semiconductor materials[10]	29
Figure 1.8: Ordering of the materials according to the magnetic behaviors	31
Figure 1.9: Degradation mechanism of the magnetic core@shell photocatalyst Fe ₃ O ₄ @TiO ₂ with graphene oxide modification[41]	33
Figure 1.10: Illustration of the photocatalytic dye degradation on the photocatalyst surface.....	35
Figure 2.1: UV-Visible Diffuse Reflectance Spectroscopy Instrument	44
Figure 2.2: Raman Scattering Mechanism[57]	45
Figure 2.3: Raman Spectroscopy Instrument	46
Figure 2.4: Three electrode photoelectrochemical cell reaction system under the visible light ($\lambda > 400$ nm).....	48
Figure 2.5: Photocatalytic Methylene Blue Degradation Reaction System	50
Figure 3.1: XRD pattern of the Fe ₃ O ₄ photo-catalyst	52
Figure 3.2: XRD pattern of the TiO ₂ , NiFe ₂ O ₄ @TiO ₂ and Fe ₃ O ₄ @TiO ₂ photo-catalyst (A: Anatase phase; R: Rutile phase).....	54
Figure 3.3: UV-DRS spectra and Tauc plots of the photocatalyst TiO ₂ , Fe ₃ O ₄ @TiO ₂ , Fe ₃ O ₄ @TiO ₂ -Ni ²⁺ synthesized by vapor thermal method.....	55
Figure 3.4: UV-DRS spectra and Tauc plots of the photocatalyst TiO ₂ , Fe ₃ O ₄ @TiO ₂ , Fe ₃ O ₄ @TiO ₂ -Ni ²⁺ synthesized by non-thermal method	56
Figure 3.5: UV-DRS spectra and Tauc plots of the photocatalyst TiO ₂ , NiFe ₂ O ₄ @TiO ₂ and NiFe ₂ O ₄ @TiO ₂ -Ni ²⁺ synthesized by vapor thermal method.....	57
Figure 3.6: UV-DRS spectra and Tauc plots of the photocatalyst TiO ₂ , NiFe ₂ O ₄ @TiO ₂ and NiFe ₂ O ₄ @TiO ₂ -Ni ²⁺ synthesized by non-thermal method	58
Figure 3.7: SEM images of the Fe ₃ O ₄ @TiO ₂ and Fe ₃ O ₄ @TiO ₂ -Ni ²⁺ photo-catalyst, respectively	59
Figure 3.8: SEM images of the NiFe ₂ O ₄ @TiO ₂	59
Figure 3.9: EDS Analysis result of the Fe ₃ O ₄ @TiO ₂ -Ni ²⁺ photocatalyst.....	60

Figure 3.10: SEM images for the EDS Analysis performed for the $\text{Fe}_3\text{O}_4@\text{TiO}_2\text{-Ni}^{2+}$ photocatalyst	61
Figure 3.11: Raman spectra of the Fe_3O_4	61
Figure3.12: Raman spectra of the TiO_2 , $\text{Fe}_3\text{O}_4@\text{TiO}_2$, $\text{Fe}_3\text{O}_4@\text{TiO}_2\text{-Ni}^{2+}$, $\text{NiFe}_2\text{O}_4@\text{TiO}_2$ and $\text{NiFe}_2\text{O}_4@\text{TiO}_2\text{-Ni}^{2+}$ prepared by vapor thermal method.....	62
Figure3.13: Raman spectra of the TiO_2 , $\text{Fe}_3\text{O}_4@\text{TiO}_2$, $\text{Fe}_3\text{O}_4@\text{TiO}_2\text{-Ni}^{2+}$, $\text{NiFe}_2\text{O}_4@\text{TiO}_2$ and $\text{NiFe}_2\text{O}_4@\text{TiO}_2\text{-Ni}^{2+}$ prepared by non-thermal method.....	63
Figure3.14: Chronoamperometry analysis of the $\text{Fe}_3\text{O}_4@\text{TiO}_2$ photo-catalyst in the medium of methanol, Na_2S , and NaOH	65
Figure3.15: Chronoamperometry analysis of the $\text{ITO/Fe}_3\text{O}_4@\text{TiO}_2$ photo-catalyst at 15, 25, 30layerthickness. Used electrolyte 0.1M Na_2S at 0V vs. RHE	65
Figure3.16: Effect of annealing temperature on the $\text{ITO/Fe}_3\text{O}_4@\text{TiO}_2$ photo-catalyst.....	66
Figure 3.17: Linear Sweep Voltammetry Analysis under the visible light illumination. Electrolyte 0.1M Na_2S for vapor thermal method photocatalyst.....	67
Figure 3.18: Linear Sweep Voltammetry Analysis of the $\text{Fe}_3\text{O}_4@\text{TiO}_2$, $\text{Fe}_3\text{O}_4@\text{TiO}_2\text{-Ni}^{2+}$, $\text{NiFe}_2\text{O}_4@\text{TiO}_2$ and $\text{NiFe}_2\text{O}_4@\text{TiO}_2\text{-Ni}^{2+}$ samples prepared by non-thermal method under the visible light illumination and light on-off conditions. (Electrolyte 0.1M Na_2S).....	68
Figure3.19: Photo-current response of the $\text{Fe}_3\text{O}_4@\text{TiO}_2$, $\text{Fe}_3\text{O}_4@\text{TiO}_2\text{-Ni}^{2+}$, $\text{NiFe}_2\text{O}_4@\text{TiO}_2$ and $\text{NiFe}_2\text{O}_4@\text{TiO}_2\text{-Ni}^{2+}$ by vapor thermal method.....	68
Figure 3.20: Photo-current response of the $\text{NiFe}_2\text{O}_4@\text{TiO}_2$ and $\text{NiFe}_2\text{O}_4@\text{TiO}_2\text{-Ni}^{2+}$ by non-thermal method.....	69
Figure 3.21: Mott-Schottky plot of the TiO_2	70
Figure 3.22: Mott-Schottky plot of the $\text{Fe}_3\text{O}_4@\text{TiO}_2$ and $\text{Fe}_3\text{O}_4@\text{TiO}_2\text{-Ni}^{2+}$ in the dark condition.....	71
Figure 3. 23: Mott Schottky plot of the NiFe_2O_4	71
Figure 3.24: The optimization of the photocatalyst amount under simulated light irradiation ..	72
Figure 3.25: Calibration Curve	73
Figure 3.26: Absorbance spectra of the methylene blue solution photo-decolorization process over time in the existence of $\text{NiFe}_2\text{O}_4@\text{TiO}_2$ photocatalyst and degradation efficiency vs. time	74
Figure 3.27: Degradation efficiency of the photocatalysts $\text{Fe}_3\text{O}_4@\text{TiO}_2$, $\text{Fe}_3\text{O}_4@\text{TiO}_2\text{-Ni}^{2+}$, $\text{NiFe}_2\text{O}_4@\text{TiO}_2$, $\text{NiFe}_2\text{O}_4@\text{TiO}_2\text{-Ni}^{2+}$ under the simulated visible light irradiation	74
Figure3.28: The Results of the Recycling Studies for the $\text{NiFe}_2\text{O}_4@\text{TiO}_2\text{-Ni}^{2+}$ photocatalyst synthesized by vapor thermal method.....	75
Figure3.29: Degradation efficiency of the $\text{Fe}_3\text{O}_4@\text{TiO}_2$, $\text{Fe}_3\text{O}_4@\text{TiO}_2\text{-Ni}^{2+}$, $\text{NiFe}_2\text{O}_4@\text{TiO}_2$, $\text{NiFe}_2\text{O}_4@\text{TiO}_2\text{-Ni}^{2+}$ samples prepared by non-thermal method under the simulated light irradiation	76

LIST OF TABLES

Table2.1: The classification of the photocatalysts according to the characterization method applied in this work.....	51
Table 3.1: Measured Crystallite sizes of the Prepared Photo-catalyst.....	54
Table 3.2: Obtained Band Gap Values of the prepared photocatalyst.....	58
Table 3.3: Photo-current response results of the synthesized photo-catalysts.....	69
Table 3.4: Mott-Schottky Analysis Results of the samples.....	72
Table 3.5: Degradation Efficiency of the Prepared Photocatalysts by Vapor Thermal Method	75
Table3.6: Degradation Efficiencies of the Prepared Photocatalysts by Non-Thermal Method..	77

Şekil tablosu ögesi bulunamadı.

ABSTRACT

SYNTHESIS AND CHARACTERIZATION OF MAGNETIC PHOTOCATALYSTS FOR HYDROGEN GENERATION

In today's world, the energy and environment are more related to each other. After the industrial revolution and the depletion of the energy sources the environment pollution has increased rapidly. With the investigation for the new alternative methods which have positive effect to the environment, the degradation of the organic pollutants with photocatalytic processes and the photoelectrochemical hydrogen production methods using the renewable source solar light have gained significant attention. All of this study depends on the heterogeneous photocatalysis process which uses the semiconductor photocatalysts.

In this work, the easily separable from the reaction medium and photocatalytic and photoelectrocatalytic active photocatalyst material synthesis were performed to improve the efficiency in visible light spectrum using the TiO₂ semiconductor which has wide band gap energy (active in UV region). Synthesized photocatalysts were designed as a core shell structure to boost the electron hole charge and suppress the recombination reaction.

Firstly, the planned materials were produced by a vapor thermal technique. The materials were characterized by XRD, UV-DRS and Raman spectroscopy. In the further step same structure magnetic core-shell photocatalyst were arranged via non-thermal method. Magnetic core and TiO₂ were synthesized separately and had been come together with ultrasonication. Moreover, for two synthesis method Ni²⁺ loading had been conducted to examine the effect of the photo-(electro)-catalytic activity. Fe₃O₄/NiFe₂O₄@TiO₂ samples were tested under the synthesis technique with methylene blue degradation analysis to search how photocatalytically efficient under the visible light. After the comparison for the photocatalytic activities, the photo-current responses important determinant for the photoelectrochemical hydrogen production capacity was measured. According to the obtained results, vapor thermal method prepared the NiFe₂O₄@TiO₂-Ni²⁺ had given the optimal photocatalytic activity and 87.7% degradation efficiency was provided under the visible light irradiation. Moreover, the maximum photo-current density was obtained for NiFe₂O₄@TiO₂-Ni²⁺ which is 37 μA/cm². However, the non-

thermal method samples showed pure photocatalytic activity and only 59.83% degradation efficiency was obtained for the $\text{Fe}_3\text{O}_4@\text{TiO}_2\text{-Ni}^{2+}$ photocatalyst. Besides, the photo-current response obtained for $\text{NiFe}_2\text{O}_4@\text{TiO}_2$ photocatalyst was $132 \mu\text{A}/\text{cm}^2$ under visible light illumination.



ÖZET

MANYETİK FOTOKATALİZÖRLERİN HİDROJEN ÜRETİMİ İÇİN SENTEZİ VE KARAKTERİZASYONU

Günümüzde, enerji ve çevre birbiriyle ilişki olan iki önemli alandır. Sanayi devrimi ve enerji kaynaklarının tükenmesiyle birlikte çevre kirliliğinde de büyük bir artış yaşanmaktadır. Çevreye olumlu etkileri olan alternatif enerji kaynaklarının aranmaya başlanmasıyla, organik kirleticilerin fotokatalitik proses ile bozunması ve yenilenebilir kaynak güneş ışığı kullanılarak fotoelektrokimyasal hidrojen üretim yöntemleri oldukça önem kazanmaya başlamıştır. Bu çalışmada yarı iletken fotokatalizörün kullanıldığı heterojen fotokataliz reaksiyonlarına dayanmaktadır.

Yaptığımız bu çalışmada, reaksiyon ortamından kolayca ayrılabilen, fotokatalitik ve fotoelektrokatalitik olarak etkin fotokatalizörler malzemelerinin sentezi geniş bant aralığına sahip ve UV bölgede etkin TiO_2 karakterize edilerek gerçekleştirildi. Sentezlenen fotokatalizörler reaksiyon sırasında oluşan elektron-boşluk çiftlerini arttırmak ve bu oluşan elektron-boşluk çiftlerinin yeniden birleşmesini baskılamak amacıyla çekirdek-kabuk yapısı şeklinde tasarlandı.

İlk olarak, planlanan fotokatalizörler buhar-termal yöntemi ile sentezlendi. Dizayn edilen malzemeler XRD, UV-DRS, SEM ve Raman spektroskopisi analizleri ile karakterize edildi. Bir diğer aşamada, manyetik çekirdek kabuk yapısında planlanan aynı fotokatalizörler non-termal yöntemi ile sentezlendi. Non-termal yöntemde buhar-termal yönteminden farklı olarak manyetik çekirdek ve TiO_2 yapısı ayrı bir şekilde sentezlendi ve ultrasonikasyon su banyosu ile birleştirildi. Ayrıca, her iki yöntemde fotokatalizörlere foto(elektrik)katalitik etkisini arttırmak amacıyla Ni^{2+} yüklemesi yapıldı. $\text{Fe}_3\text{O}_4/\text{NiFe}_2\text{O}_4@/\text{TiO}_2$ örnekleri her iki yöntemle sentezlenmiş aynı tür katalizörlerin fotokatalitik aktivitesini incelemek amacıyla metilen mavisi bozunması görünür ışık altında test edildi. Fotokatalitik aktivitelerin test edilmesinden sonra hidrojen üretim kapasitesinin ölçülmesinde önemli bir belirleyici olan foto-akım ölçümleri yapıldı.

Elde edilen sonuçlara göre buhar termal yöntemi ile hazırlanan fotokatalizörlerden $\text{NiFe}_2\text{O}_4@/\text{TiO}_2\text{-Ni}^{2+}$ fotokatalizörü diğer fotokatalizörlerin yanında en fazla fotokatalitik aktivite göstermiş ve metilen mavisi 87,7% oranında bozunmaya uğramıştır. Ayrıca, aynı

şekilde $\text{NiFe}_2\text{O}_4@\text{TiO}_2\text{-Ni}^{2+}$ fotoelektrokimyasal ölçümlerde en yüksek foto-akım değeri $37\mu\text{A}/\text{cm}^2$. Bununla birlikte, non-termal yöntemi ile hazırlanan fotokatalizörler düşük fotokatalitik aktivite göstermiştir. Bu yöntem ile sentezlenen fotokatalizörler $\text{Fe}_3\text{O}_4@\text{TiO}_2\text{-Ni}^{2+}$ ile en yüksek bozunma oranı 59% elde edilmiştir. Ayrıca, non-termal yöntemde $\text{NiFe}_2\text{O}_4@\text{TiO}_2$ en yüksek fotoelektrokatalitik aktivite göstermiş ve görünür ışık altında en yüksek foto-akım değeri $132\mu\text{A}/\text{cm}^2$ elde edilmiştir.



1 INTRODUCTION

Today, resources are used to meet the energy needs of the worlds (coal and oil derivatives) has been exhausted. An increasing necessity for a clean environment has increased the awareness in alternative and renewable energy sources.

Solar energy is a renewable energy source which uses most of photocatalytic applications which can become a possible solution for the world energy demands[1]. Solar energy should be transformed and kept an energy form to meet the energy demand. Hydrogen is an alternative source to use the solar energy effectively[2].Hydrogen is an important energy vector that is a promising candidate for the following reasons: (1) it can be obtained from the sustainable resources such as water, biomass, fossil fuels etc. which is a sufficiently chemical in the earth; (2) the achievable energy efficiency is higher than the other fuels when compared; (3) if it is brought into existence from the renewable sources, it will not spread to the environment greenhouse gas, pollutants etc. If we consider these reasons hydrogen is the most clean source to meet the world energy demands[1].

Currently, hydrogen production is supplied from renewable energy merely5% and it mainly obtained via water electrolysis 95% hydrogen from fossil fuels. Hydrogen production from renewable sources is not widespread since the price is still extreme. Photoelectrochemical reaction systems have gained great interest using solar energy for hydrogen production since the properties are of environmentally friendly, low cost and a clean way. The initial work of Fujishima and Honda which was reported about the photoelectrochemical hydrogen generation using the TiO₂ electrode gives rise to the semiconductor photocatalysis[3].

Innovative investigations have been published in several journals and many review papers on the semiconductor photocatalysis reactions can be found in the literature which highlight the photocatalytic water purification and some of researches are connected to the photoelectrocatalytic hydrogen production[1, 4-6]. Photocatalytic water purification and photoelectrocatalytic hydrogen production need photo generated e^-/h^+ charges. Yet, the utilization of the electron-hole pairs and the processing system are diverse. In photocatalytic purification of water, the valence band holes are the vital factor that manages to the decomposition of organic contaminants whereas in the water splitting

process for hydrogen production the conduction band electrons are the key elements for reducing the protons to the H₂.

Regarding these factors, we aimed to combine the photocatalytic water purification and hydrogen production via photoelectrochemical cell reactions and investigate the photocatalytic and photoelectrocatalytic activity of the prepared photocatalysts[3].

1.1 HETEROGENEOUS PHOTOCATALYSIS FOR ENERGY AND ENVIRONMENT PROBLEMS

The field of heterogeneous photocatalysis has gained significant attention mainly in energy and environment. Heterogeneous photocatalysis is described as the chemical transformation which occurs in photocatalyst medium. Heterogeneous photocatalysis has different applications as depicted in Figure 1.1. The most common application of heterogeneous photocatalysis is the solar water splitting and purification of water or air which contain organic contaminants[7].

Recently, heterogeneous semiconductor photocatalysis has gained important attention especially to degrade the organic contaminants. Heterogeneous photocatalysis is performed in several media: gas and pure organic liquid phase or aqueous solution. The overall reaction mechanism contains five independent steps as described below:

- 1- Reactant transformation to the surface
- 2- Absorption at least one reactant
- 3- Adsorbed phase reaction
- 4- Desorption of the products
- 5- Separation of the final products [1]

Photocatalysis is generally founded on the illumination of a semiconductor with light effect. By effect of the photons which come from the light source, the semiconductor yields extremely free radicals which oxidize the adsorbed reactants on semiconductor surface area[8]



Figure 1.1: Scope of Heterogeneous Photocatalysis Applications

Heterogeneous photocatalysis has been widely used several applications as depicted in Figure 1.1. Water treatment and water splitting is two effective fields which are both strongly connected with the searching in photoelectrochemistry using semiconductor since the 1960s. Intensive studies started after the invention of the n-type TiO_2 photoelectrode in a photoelectrochemical cell using water. After this, numerous investigations have gained attention on the application of solar light for the generation of hydrogen as a sustainable fuel from water. Moreover, various researchers have discovered that semiconductor materials could degrade the organic and inorganic samples with redox reactions. Particularly, this organic and inorganic particles are generally known as environment pollutants[9].

Photoelectrochemical water splitting can be used to lead the planning of the splitting of water molecule using semiconductor particles in photocatalytic systems. Such particulate systems gain advantages of simple and cheaper to establish a system which is beneficial for supplying generation of hydrogen. It is clear that growing concerns about the environmental cleaning have also aroused the attention for heterogeneous photocatalysis especially water treatment. In our experiments we investigated these two important field of heterogeneous photocatalysis energy and environment using semiconductor materials which mimic the photosynthesis process.

1.2 ALTERNATIVE ENERGIES AND HYDROGEN

Generally, fossil fuels are an important source of energy. Sustainable energy needs have been increasing in today's world due to the depletion of fossil fuel source. Moreover, because of the negative effect to the environment of the fossil fuel source, several attempts have been made to find a sustainable energy. This growing request for the energy and defending the environment have initiated searching alternative sources for the energy production. The renewable energy is the finest possible way to exchange the fossil fuel. Sun is an endless energy supply. The energy obtained from the sun not only meet our energy needs but also protects the environment. Photosynthesis is an example of the fabrication as well as helps to store solar energy. In the light of this information, artificial photosynthesis system have been designed by researchers using the photosynthesis mechanism. Thus, splitting of water molecule by photocatalytic process with the utilization of photocatalyst is a practical and environmental friendly solution for solar energy storage and use. The breaking of water molecule into its basic components hydrogen and oxygen using solar energy is an effective property of the water splitting processes. In water splitting process, solar energy can be stored in the form of hydrogen gas. Recently, the hydrogen based applications have gained considerable attention[10].

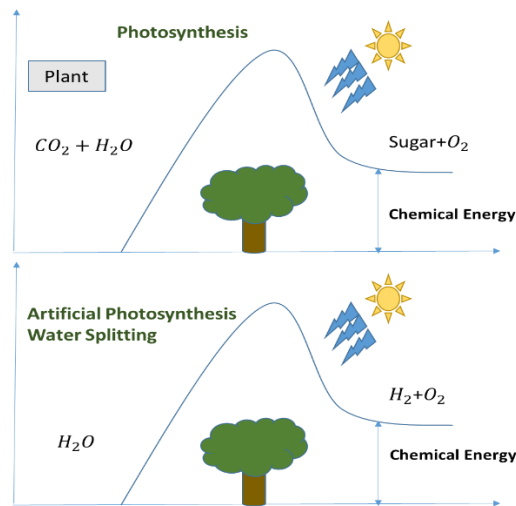


Figure1.2:Illustration of basic scheme of photosynthesis and photocatalytic water splitting as artificial photosynthesis[11].

Conventionally, fossil fuels is the main source to produce hydrogen for instance natural gas by steam reforming processes. Hydrogen generation from other fossil sources is

obtained from partial oxidation process, auto-thermal reforming, water electrolysis, biomass, thermochemical process, photobiological process. Close to 50% is obtained from natural gas steam reforming process, 30% is from oil/naphtha reforming processes, water electrolysis provides 3.9% and coal gasification is of 18% and 0.1% from other sources[12].

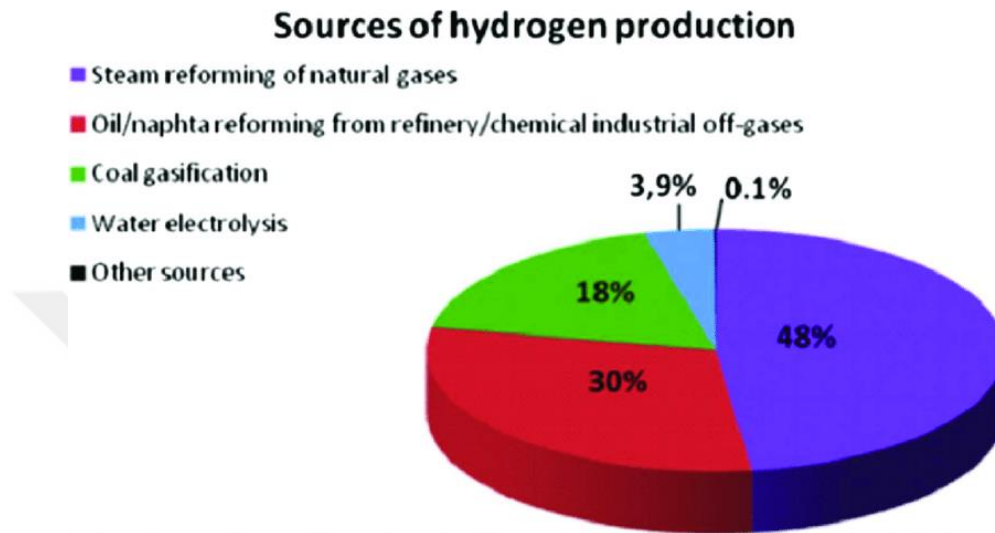


Figure1.3: Distribution of the Hydrogen Production Resources for Conventional Production Method[13]

Renewable energy supplying method has lower carbon emissions when a comparison is with conventional energy production method. This energy production routes generally consist of wind, hydropower, geothermal, solar etc.

Wind energy is used the mechanical power to generate electrical energy. Nonetheless, being a renewable source of energy it is free and abundant but main disadvantage is not being storable. Moreover, hydropower can be produced from water and the produced energy can be converted to electricity. Hydroelectric dam is the most common method to obtain the electricity from the hydropower source by using water. Basically, hydropower dam is transferred the water through turbines which causing them the rotary motion and the energy which is generated by water movement is captured. Geothermal energy is generated by heat treatment to the water or rocks deep underground. Different from the other alternative energy sources, geothermal energy can be obtained after many years. Solar energy is an infinite source which can be obtained from the sun and can be transformed to the electricity. However, the most important criteria to use the solar energy

is the geographical place, season and time of day etc. To summarize, the renewable energy sources is dependent to the location and time. Hence, it is required to recognize the medium to store the energy [14].

1.2.1 Hydrogen Production Methods

- **Hydrogen Production from Fossil Fuels**

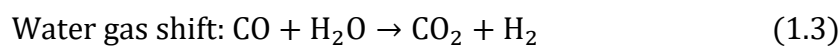
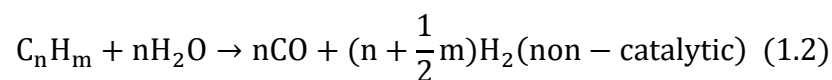
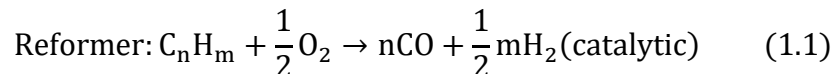
Production of by utilizing the fossil fuels is a conventional method. There are several ways from to make use of fossil fuels for hydrogen generation, the main of which is the hydrocarbon reforming and hydrocarbon pyrolysis. These techniques provide almost entire hydrogen need. Presently, still fossil fuels keep its dominant role in hydrogen production sources.

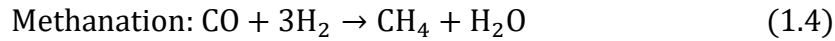
Steam Reforming Method

Basically, steam reforming comprises catalytic transformation of hydrocarbon to the hydrogen and carbon oxide products which contains several production steps reforming, synthesis gas generation, water-gas shift and gas purification. For cutting down the H₂ need and inhibit the formation of coking on the catalyst surface, the parameters of operation are designated at high temperatures and pressures 3.5 MPa[15].

Partial Oxidation Method

Partial oxidation generally starts with the alteration of steam into oxygen and hydrocarbons which then processed and turn to carbon oxides as byproducts and hydrogen as main product. The temperature requirement for the catalytic process to occur might require about 950°C whereas the non-catalytic process at 1150-1315 °C can drive with hydrocarbons consisting methane, coal, heavy oil etc. The catalytic and non-catalytic processes can be denoted in the following equations





Autothermal Reforming Method

Autothermal reforming technique is a partial oxidation process which is exothermic in nature, generates the heat whereas the endothermic steam reforming uses this energy to generate hydrogen. Fundamentally, steam and oxygen gas comes in contact in the reformer, initiating the reforming and oxidation reactions[15]

- **Hydrogen Production from Renewable Sources**

Electrolysis

Carbon-free and sulfur-free hydrogen is the most significant benefit of this method. The only drawbacks of this method is to have higher cost and energy needs than the fossil fuel. Using the wind to generate pollution free hydrogen shows the highest potential among renewable sources.

Biomass Gasification

Biomass is a renewable source derived from agricultural residues, forestry, wood processing, animal wastes, crops etc. which used as a hydrogen production source[15]. At present, the biomass gasification is not able to provide hydrogen energy. But, using this technique a clean hydrogen production can be recovered. As CO₂ released after the biomass oxidation which can be adsorbed from the atmosphere which fixed by photosynthesis. The option to reduce the CO₂ emission, biomass gasification has a potential over fossil fuel [16].

Solar Hydrogen Production

Hydrogen is renewable resource when generated from solar light or via electricity from a renewable source for example wind energy, hydropower etc. Many materials contain hydrogen. Besides, water is the most abundant as can be naturally found (river, rain etc.). Moreover, hydrogen can be obtained by the means of fossil fuels, biomass, ammonia etc. If hydrogen is extracted from fossil fuels, carbon dioxide also separated which causes the rising the greenhouse gas effect and many pollutants to the stratosphere [12].

The abundant amount of water and sun is an alternative and promising way to produce hydrogen. Hydrogen evolution reactions can be generally classified into three: (1) thermo-chemical water splitting, (2) photo-biological water splitting, (3) photo-catalytic and photoelectrocatalytic water splitting.

Thermochemical water splitting can be considered the simple way to generate hydrogen. In this method heat adjustment and management is not an easy process and also not sustainable in the long term. Photo-biological water splitting is another method to get hydrogen and classified into two classes. During the light illumination, high ratio hydrogen obtained under anaerobic condition which is related to water bio-photolysis and the other is referred as organic bio-photolysis. Organic bio-photolysis uses the organic wastes to generate high yield hydrogen. Nevertheless this method releases CO₂ to the environment which is not convenient for the future perspective because of the greenhouse effect. Photo-catalytic water splitting using solar light method has a huge potential for the hydrogen generation. If we compare this technique with the thermochemical and photo-biological water splitting is of some benefits: (1) efficient hydrogen generation from solar light, (2) choosing optimal photo-catalyst for low cost, (3) convenient and cheap reactor design providing wide application[14, 17].

1.3 PHOTOCATALYTIC WATER SPLITTING

Solar and water are the renewable and the most promising energy sources on the universe. The conversion to the hydrogen while utilizing the solar light has gained much attention after the Fujishima and Honda's photo-electrochemical cell using the TiO₂ semiconductor material. In recent years, splitting of water molecule by photocatalytic process by utilizing the semiconductor materials in order to generate of clean fuel hydrogen demonstrated high potential to meet the world's energy demand. Crystallinity and particle size of the semiconductor material has a huge effect on the photocatalytic activity of a metal-oxide photo-catalysts which generally depends on the synthesise method[18]. Several researchers had searched the water splitting using different type semiconductor materials in the experiments as a photo-electrodes or photo-catalysts since the invention. Nevertheless, an efficient photocatalytic material which is active under the visible light illumination still had not been found. Besides, the new photocatalyst materials have been examined for an effective photocatalytic and photoelectrocatalytic water splitting

reactions[11]. Basic photocatalytic water splitting contains the reduction and oxidation reactions. The first step starts with the absorption of the photon energy by the semiconductor and generates the electron-hole pairs. The structure of a semiconductor is the most important criteria for an effective reaction. Most of the heterogeneous photocatalysts keep the semiconductor properties. Valence band and conduction band are the basic characteristic bands of a semiconductor and the difference between them is referred to as band gap value. Under dark conditions, both charge carriers, i.e. electrons and holes, are in the valence band. When a photon of light having energy greater than that of the band gap, an electron gets excited with this energy and moves to the conduction band as a majority charge carrier, while holes as minority charge carriers remain in the valence band. Excited e^- and h^+ pairs create the redox reaction which is similar to photoelectrolysis. Water molecule reduction happens with the e^- which arises from the valence band to produce H_2 and the h^+ oxidizes to form O_2 molecules. For hydrogen generation, the conduction band position potential must be further negative than the redox potential of the hydrogen generation (H^+/H_2 ; 0V vs. NHE) and the valence band position must be more positive than the potential of the oxygen generation (O_2/H_2O ; 1.23V).

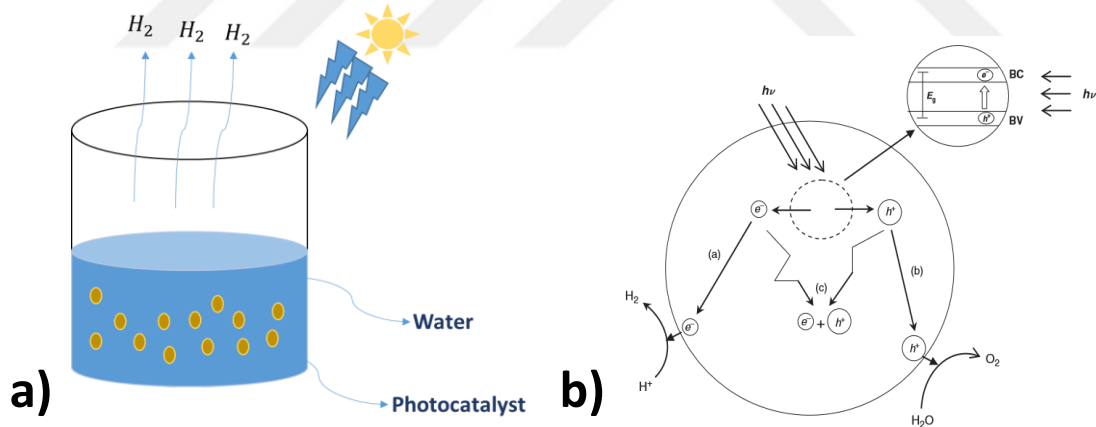


Figure 1.4: a) Schematic illustration of water splitting process to generate hydrogen under solar energy[11]; b) The basic principle of photocatalytic water splitting on photocatalyst surface[19]

Moreover, generated e^- and h^+ pairs are divided and transfer without recombination. The crystallinity is the most important feature to boost the charge separation and increase the photocatalytic efficiency. If the semiconductor has defects, the photocatalytic efficiency decreases which can be obtained from the mechanism. The defects may result in the recombination

of the photo-generated charges. However, the crystal size is smaller, the time interval becomes smaller for transportation on the semiconductor surface and materialize the reaction.

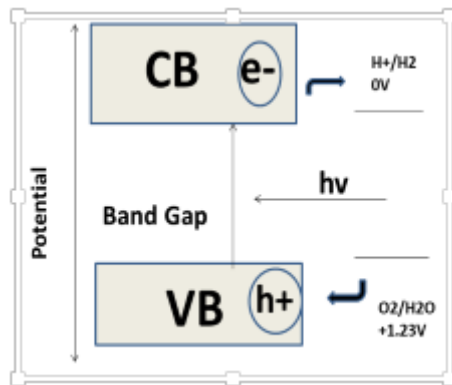


Figure 1.5: Photocatalytic water splitting principle on top of the semiconductor surface

The last part contains the chemical reaction which happening on the surface of the semiconductor. The surface characteristic is the basic factor for realization of the reaction. If the active sites on the semiconductor surface bigger than the generated electron and hole with the effect of light can exceed the potential of water splitting since the charges can perform the reduction and oxidation reactions without recombination.

A high crystallinity is mostly required for the photocatalytic water splitting applications since up and hill reactions among the electrons and holes. In opposite, big surface area is a necessity for the decomposition of the organic pollutants due to the adsorption of the compounds are much more important to degrade the hydroxyl group in the reaction[3, 11].

1.4 PHOTELECTROCHEMICAL WATER SPLITTING

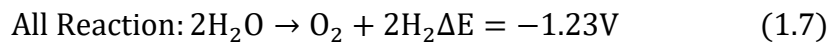
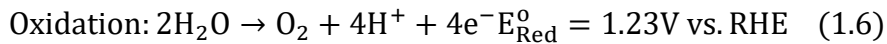
Fujishima and Honda promoted the photo-electrochemical splitting of water molecule using a semiconductor material with advanced efficiency and low cost for the first time. This invention has gained much more attention for using of solar energy to fabricate a renewable, long-term and dirt free energy economy. Basically, splitting of water photoelectrochemically depends on the solar energy alteration to hydrogen by performing a light illumination on a semiconductor material in a suitable electrolyte medium which is enable to absorb light efficiently. As splitting of water photocatalytically,

semiconductor material is the vital factor in PEC applications. Semiconductors activate the reduction and oxidation reactions under the light illumination. These materials are able to keep the light which start the redox reaction to produce the hydrogen with an additional voltage to carry out the chemical reaction efficiently. This additional voltage required to carry out the chemical reactions in the medium and provides an externally applied chemical bias. This applied additional voltage assists to drive the reaction at a desired current density. A semiconductor material is prepared by a convenient technique as a photo-electrode. The photo-electrode is illuminated with a light source and excited e^- are transferred to the semiconductor CB under the illumination from VB. Generated charges are divided to form the hydrogen at the CB (n type semiconductor), and at VB to form oxygen molecules[20, 21].

1.4.1 Basic Working Principle of Photoelectrochemical Cell Mechanism

Hydrogen and oxygen formation via splitting of water photoelectrochemically basically depends on the chemical reactions which occur on the photoelectrochemical cell. The photoelectrolysis can be categorized into five main step which are (1) photon absorption with bigger energy than the semiconductor energy level between the CB and VB, (2) generation of the photoexcited charges, (3) division of charge carriers at semiconductor-electrolyte boundary (4) charge carriers diffusion semiconductor-electrolyte boundary and (5) redox reactions occurring at the electrodes (reducing H^+ ion to H_2 and oxidizing water to form O_2).

The general solar splitting mechanism of water consists of two half reactions take position at the photoelectrochemical cell on photoelectrode surface.



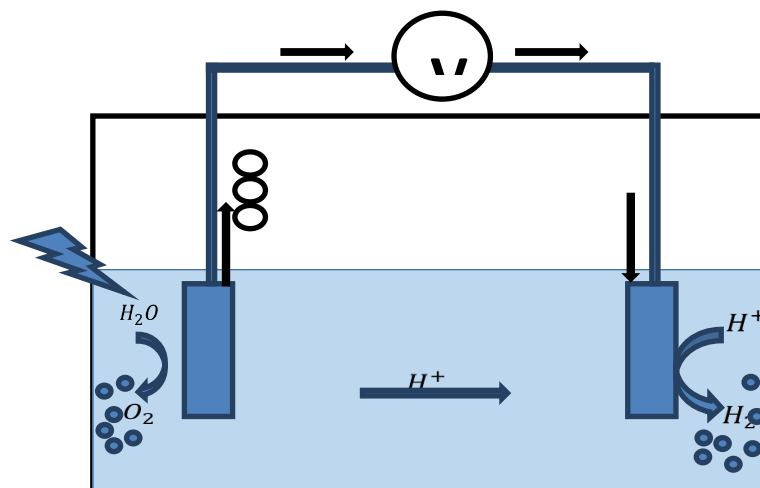


Figure1.6: Schematic diagram of the photoelectrochemical cell reactions

1.4.2 Basic Factor That Affecting the Photo-electrochemical Water Splitting

- **Crystallinity**

Crystallographic properties affect the activity of a semiconductor material in photo-electrochemical reaction. The degree of the crystalline shows much more efficient performance if we compare the amorphous materials. The more the orderliness of a crystalline material increases, the higher the photo-electro-catalytic performance obtains. As can be considered the high crystallinity increases the defect density and electron-hole transferring, this diminishes the back combination of the charges in the electrolyte.

- **Temperature**

The temperature is a vital factor especially for the efficiency of a photo-electrochemical cell. Researchers showed that the temperature affect the semiconductor CB and VB energy difference. Besides, a significant part is the annealing temperature to determine the optimal conditions for a photo-electrochemical cell experiments.

- **Size**

The particle size affects the photoelectrochemical activity of the material. Also the structure of a photocatalyst can improve the charge separation. Larger particles can lead the electrons and holes transportation effectively which decreases the recombination at the electrolyte and electrode interface.

- **Band Gap**

The band gap range is mostly control the PEC efficiency. In general, the appropriate band gap range ought to be between 1.6 eV -2.2 eV to obtain an efficient PEC activity. The narrow band gap helps the light absorption in the visible light spectrum. Conversely, wide band gap fails to absorb the light and convert the photon energy to split the water.

- **pH Dependency**

pH value plays a vital role . The Ph value generally depends on the electrolyte solution pH value. The selection of the optimal medium can be achieve the choosing the most suitable electrolyte solution which usually depends on the basic semiconductor characteristics and also deposition techniques of the electrode. For example TiO₂ is a n-type semiconductor material and any electrolyte medium can be used for e PEC cell[22].

- **Light**

The light source should be modified and chosen to obtain the high photo-response in a PEC cell. The type of the light source should be specified by taking care of the absorption capacity in the wavelength spectrum.

1.4.3 Activity Calculations

In photoelectrochemical measurements, activity calculations are complex. Measuring the photoelectrochemical performance, the most important point is the photon energy transformation to the chemical energy. A recent study examined the different efficiency calculation methods. It was reported that two general efficiency calculations used to investigate the PEC and solar cells efficiencies. It was shown as external quantum efficiency and internal quantum efficiency.

External quantum efficiency is measured from the ratio of the number of charge carriers produced by the cell over the number of photons applied on the cell . IPCE (incident photon to current conversion efficiency) is a form of the efficiency of the external quantum efficiency[23].

$$IPCE = \frac{1240 \times I_{PH}}{P \times \lambda} \quad (1.8)$$

I_{PH} = produced photo-current intensity ($\mu\text{A}/\text{cm}^2$)

λ = wavelength of the incident photon (nm)

P= power of the light($\mu\text{W}/\text{cm}^2$)

The semiconductor materials with a proper band gap value are required to the realization of the spontaneous water splitting reaction. Generally, PEC experiments were conducted by applying an external bias to conduct the division of water. In conclusion, the pec efficiency can be computed from the next equation especially to examine the H₂ production activity[24].

$$\eta\% = \frac{(1.23 - V_{bias}) \times I_p}{P} \times 100 \quad (1.9)$$

1.5 PHOTOCATALYSTS FOR WATER SPLITTING

Lots of semiconductor based photocatalyst materials have demonstrated high activity under the UV or visible light illumination. The photocatalysts can be classified into two basic groups: first, the metal oxides which has d⁰ configuration metal oxide semiconductors (Ti⁴⁺, Zr⁴⁺, Nb⁵⁺, Ta⁵⁺, W⁶⁺, Mo⁶⁺ etc.) and the second group is the electronic structure in d¹⁰ arrangement metal oxides (Sn⁴⁺, Ge⁴⁺, In³⁺, Ga³⁺, Sb⁵⁺, etc.).

1.5.1 UV Light Active Photocatalysts

Many UV light active photocatalysts which enable the water splitting reactions are metal oxides having the d⁰ and d¹⁰ configuration. In this category, Titanium based semiconductor photocatalysts are generally used in water splitting reactions[25].

Firstly, TiO₂ was used as a photo-anod after the invention of Fujishima and Honda. In their work, TiO₂ (Rutile) anode and Pt cathode was used in an electrochemical cell under the UV light illumination (<415 nm) via a 500 W Xe lamp. It was observed that O₂ evolution on the anode electrode. Obtained photoelectrochemical efficiency of this study was 10%. [18]. Since this pioneering work of Fujishima and Honda, many photocatalysts have been built up and H₂ production with photocatalytic and photoelectrochemical analysis has been investigated. TiO₂-based photocatalysts via loading with C or N, and S have been investigated by other researchers to boost the activity of the [18, 26-29].

Furthermore, it was reported that Au and Pt-loaded TiO₂ photocatalysts had been produced with precipitation, photodeposition, impregnation and colloidal mixing method to investigate the H₂ evolution and with this study it was realized that the synthesis method can affect the hydrogen production prominently [14, 30]. ZrS in SO₃²⁻ solution were studied to examine the H₂ generation and it was found that 90% quantum yield was obtained.

Besides, various metal oxide photocatalysts have been mostly studied in photocatalytic experiments. Ni loaded Ga₂O₃ showed effective photocatalytic activity by adding the Cr, Ca, Zn, Sr, Ta and Ba ions [31].

1.5.2 Visible Light Active Photocatalysts

From now on, reported photocatalytic systems for water splitting by using semiconductor desire ultraviolet light (UV) owing to the wider band range than other materials. However, UV light can convert the solar energy only 4%, while visible light accounts for 50%. It is vital to use the visible region to generate H₂ efficiently by photocatalytic systems. The modification of photocatalysts is mostly compelling for the efficient use of solar energy. It is claimed that the photocatalytic systems thematerial should have vital properties which is stability and resistancy in aqueous media, convenient crystallinity and low cost [32].

The condition of photoexcited charge separation is an important issue that mostly influences the photocatalytic systems. It is required that efficient photocatalysts in visible region having a convenient band gap. In recent studies various methods are being developed such as metal-metal alloys, metal-nonmetal nanocomposites (metal oxides, sulphides, nitrides etc.) to enhance the light absorption, charge transfer kinetics, structural properties and lowering the band gap range.

Fe₂O₃, is a semiconductor material which is of n-type characteristic, a narrow band gap range and active in visible region photocatalyst. It is also sensitive of TiO₂ due to the characteristic of non-toxicity and chemical stability. However, it has low charge carrier density and slow oxygen evolution reaction owing to the high surface area [33, 34].

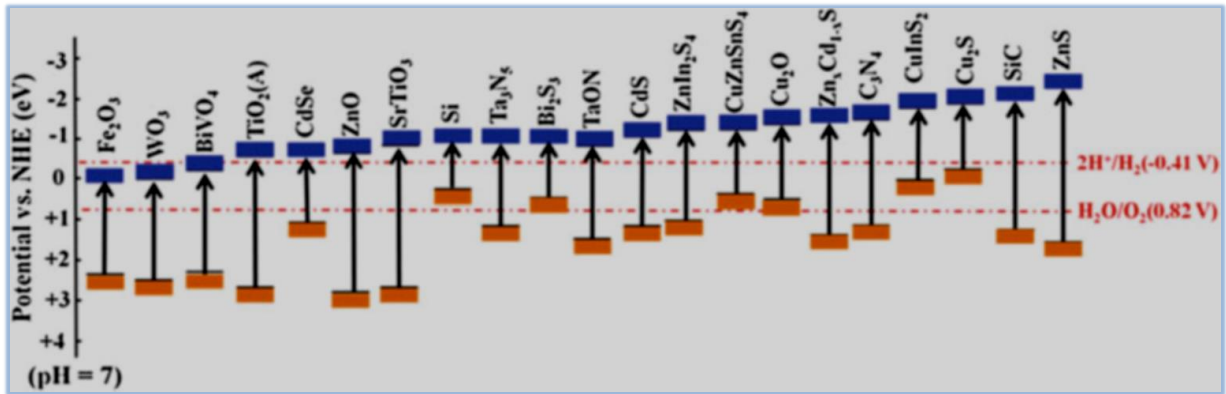


Figure 1.7: Band edge positions some of semiconductor materials[10]

Magnetic Materials

Magnetism is a physical event which mostly affect the ferromagnetic materials. The magnetism can be identified by magnetic field. With the action of an electric current or magnetic dipoles, the magnetic force is created. The response of a material as a magnetic field is enforced that shows characteristic features of the material. The spinning electrons in a material acts like a small magnet. These small magnets are arranged in the direction of magnetic material and then the material is magnetized. Magnetism is occurred when charged particles with the effect of electric are in motion. Magnetism can be observed almost all materials. However, sometimes it is evident or sometimes not obvious. Sources of magnetism can be based on two sources:

- Electric current
- Magnetic moments of electron in spin

The motion of electron in orbital and spin , also the interaction between these electrons create the magnetism. Different type of magnetic behaviours occur due to the different response of the materials to the external magnetic effects. Some of the materials are much more magnetic than others. This is the reason is that between some materials there is more interaction and the between the others there is no interaction between the atoms. The magnetic behaviours can be categorized into five class:

1-Diamagnetism

2-Paaramagnetism

3-Ferromagnetism

4-Ferrimagnetism

5-Antiferromagnetism

In the following, the basic properties of these different magnetic behaviours will be described.

Magnetic Behaviors of The Materials

Diamagnetism

Diamagnetism can be observed in all materials and this arises from the tendency of the materials to the applied magnetic field. In a diamagnetic material, whole electrons are paired, so that the intrinsic electrons cannot generate any bulk effect. Therefore, the magnetic effect depends on the electrons' orbital motion. That is the reason, in an applied magnetic field, diamagnetic materials are weakly magnetized with the opposite direction of the applied magnetism. Water, gold, copper, air are the examples of the diamagnetic materials.

Paramagnetism

In a paramagnetic material, there are uncoupled electrons. As the coupled electrons are of opposite directions which cancel out the magnetic field, the uncoupled electron is independent to arrange its magnetic field. Since the external magnetic field is performed, the magnetic field will arrange in the control of applied field

Ferromagnetism

Ferromagnetic materials can be defined as a permanent magnet. A ferromagnetic material has also unpaired electrons the same as paramagnetic material and also the magnetic moments of the electrons can arrange even if the magnetism is moved away. Basically, the iron, nickel, cobalt, and alloys of these metals are ferromagnetic materials.

Antiferromagnetism

Different from a ferromagnetic material, an antiferromagnetic material valence electrons are tend to point opposite direction. When the atoms are aligned to the opposite direction, the net magnetic field will be zero which means there is no magnetism. Antiferromagnetic behaviour can be observed mostly transition metals, hematite, nickel oxide etc.[35, 36].

Ferrimagnetism

Same as ferromagnet, ferrimagnetic materials keep magnetization when removed from a magnetic field, however the adjacent electron pairs are arranged in opposite direction. Commonly, ferrimagnetism appears magnetite and other ferrites.

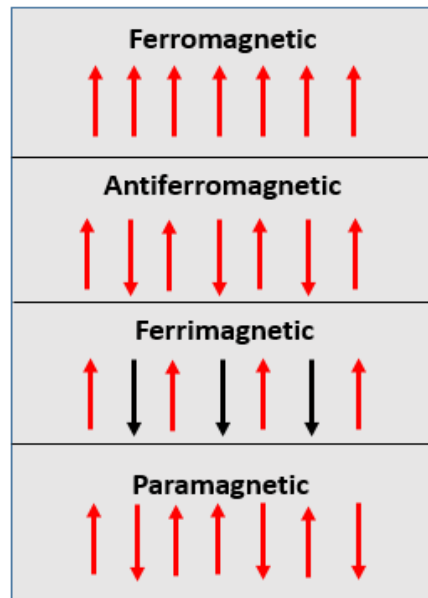


Figure 1.8: Ordering of the materials according to the magnetic behaviors

1.5.3 Magnetic Photocatalysts

Ferrites are well known magnetic materials which used several field because of their suitable physical and chemical properties, but different from the other semiconductor materials they have desirable optical absorption characteristic in the visible light spectrum and appropriate electronic structure used for the photocatalytic applications. Additionally, spinel ferrites connected photocatalysts showed higher effectiveness owing to the available catalytic sites[37]. Spinel ferrites are identified with a general

formula $M_xFe_{3-x}O_4$ which M defines the metal ions (M=Ni, Co, Zn, Mg etc.) is triple transition metal oxides. Generally used photocatalytic application of the ferrites are decomposition of the organic pollutants. Guo etc. al prepared the $MnFe_2O_4$ via a solvothermal technique and investigated the photocatalytic activity in visible light spectrum by degrading the methylene solution [38].

Core-shell multi component nanocomposites have gained significant attention due to the function of magnetism, biomedicine, catalysis, electronics etc. Core-shell multi component materials can be adapted into one system with many usefull function. Moreover, a nanocomponent with a magnetic core can be easily seperated and collected from the reaction medium. In recent reports claimed that transition metal ferrites had been used as a core and coated with a suitable semiconductor, especially in photocatalytic degradation applications [34, 39-41]. Wei etc. al studied the photocatalytic activity of the magnetic $g-C_3N_4/Fe_3O_4/TiO_2$ composite by degrading both dinitro butyl phenol and methylene blue solutions under visible light. The magnetic composite were isolated from the reaction medium and the recycling properties were tested several times[42]. Kim etc. al. designed a magnetic core-shell nanocomposite $NiFe_2O_4@TiO_2$ semiconductor material and the photocatalytic efficiency had been investigated in a methanol/water solution. It is reported that the enhancement in photoactivity and H_2 production was obtained. This result was related that the connection between the $NiFe_2O_4$ and TiO_2 was suppressed the recombination the electron/hole pairs[40]. Recent efforts have been performed to propose and construct ternary nanocomposites which are of adjustable physical and chemical properties to enhance the catalytic efficiency. It was studied that a $Fe_3O_4@SiO_2@TiO_2-Ag$ nanomaterials was tested by degrading the RhB solution to analyze the photocatalytic activity and it had showed high performance to decrease the recombination rate by Ag particles which deposited on the ternary nanocomposite, and could be easily separated due to the Fe_3O_4 , SiO_2 layer protected this magnetic core chemical and photo-dissolution and TiO_2 shell made the ternary nanocomposite high stabile through the reaction medium[43]. In another study, Yusoff etc. al. synthesized Fe_3O_4-ZnO particles as a core-shell decorated on reduced graphene oxide sheets. The prepared material activity had been investigated by photoelectrochemical experiments. According to the reported photoelectrochemical results the photocurrent density

increased effectively with increasing amount of the Zn(OH)_2 precursor and also adding of graphene sheets, the photoelectrochemical efficiency increased significantly[44].

Ferrites are chemically and thermally stable in aqueous media. In the existence of the different metal cations (MgFe_2O_4 , NiFe_2O_4 , ZnFe_2O_4 etc.) checked against to the single component metal oxide (iron oxide) the electron/hole transfer can be facilitated and this can improve the photoactivity. Chang etc. al. has studied the effects of the morphology, crystalline property, magnetic property, surface area and photocatalytic activity for the H_2 generation of the $\text{CoFe}_2\text{O}_4@ZnS$ core@shell photocatalyst. It was reported that the calcination assists the improvement of the photocatalytic activity[45].

In literature graphene supported photocatalyst have been investigated on magnetic core-shell materials. Ma etc. al studied that $\text{Fe}_3\text{O}_4@TiO_2$ magnetic core@shell nanoparticle synthesis and photocatalytic activities. Magnetic core@shell was prepared via a hydrothermal method and then with a second hydrothermal method graphene oxide was reduced on the magnetic photocatalyst. It was notified that the decolorization of methyl orange dye was performed to examine the photocatalytic action of the semiconductor under the illumination of solar light. In Figure 1.3 the illustration of the degradation mechanism on the reduced graphene oxide supported $\text{Fe}_3\text{O}_4@TiO_2$ photocatalyst.

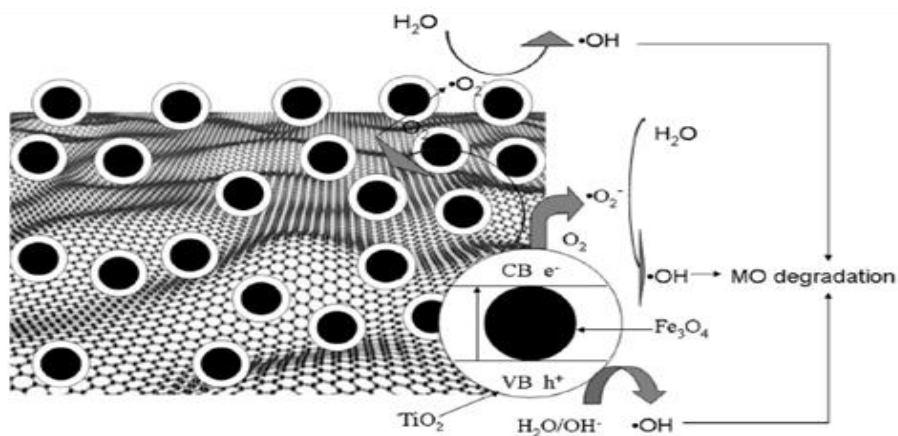


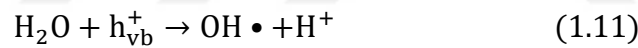
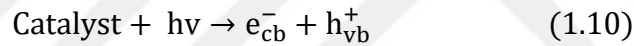
Figure 1.9: Degradation mechanism of the magnetic core@shell photocatalyst $\text{Fe}_3\text{O}_4@TiO_2$ with graphene oxide modification[41]

1.6 PHOTOCATALYTIC DYE DEGRADATION

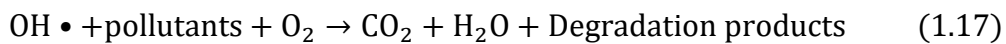
The basic theory of the photocatalysis is withstand the semiconductor illumination by a light (UV or visible). In degradation process, when the photons affect the semiconductor

the highly oxidizing radicals which degrading the organic pollutants on the material surface. The photon energy is transformed into chemical energy with the effect of redox reactions on semiconductor. This creates the activation sites of the semiconductor to decompose the molecular pollutants which being in the medium. The degradation process initiates with the radical oxidation process by strong oxidants such as OH•[8].

The photocatalytic dye degradation process is regarded to take place the following reaction steps. Firstly, with the light illumination, e^-/h^+ pairs are generated at CB and VB of the illuminated semiconductor surface, respectively. Both these charges can transfer to the semiconductor surface to realize the chemical reactions where the other species present in the medium such as organic pollutants. In generally, the hole generated at the valence band can react with H_2O and form OH• and electrons counter with the O_2 to form anion of oxygen $O_2^-•$. This intermediate reaction prohibit the back reaction of the e^-/h^+ pairs. Higher oxidation and reduction potentials of OH• and $O_2^-•$. can manage to figure other species which is in charge for the discolorization process of the model molecule[46, 47].



Generated radicals which in the photocatalytic process can degrade the organic pollutants, dyes, pesticides, intractable contaminants adsorbed on the semiconductor surface. In the last part of the reaction mechanism as shown in Figure 1.10 we can write down the final products as;



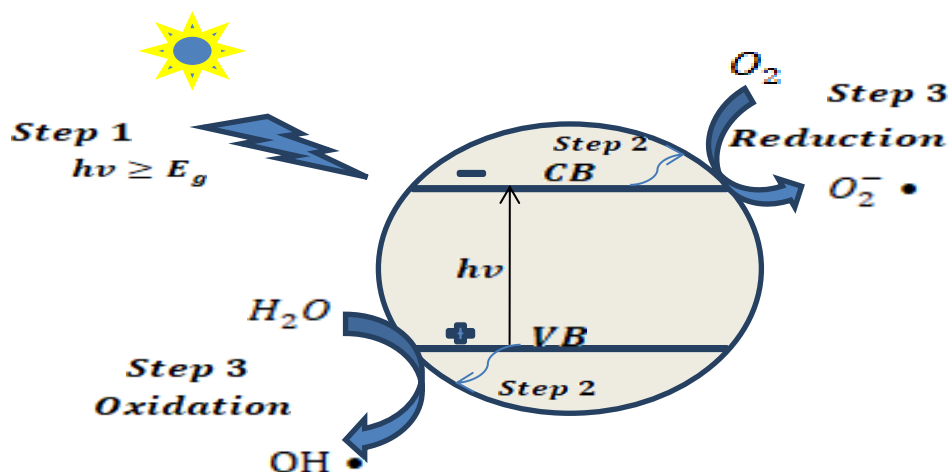


Figure1.10: Illustration of the photocatalytic dye degradation on the photocatalyst surface

1.6.1 Effect of the Working Parameters

- **Effect of pH**

The pH has an important factor on the degradation process effectiveness. Depends on the semiconductor type it can affect of the decolorization rate of the process and dye absorption on the semiconductor surface. Ajmal etc. al claimed that holes produced at lesser pH level act as main oxidizing species at higher pH level hydroxial radicals are responsible for the oxidation of the pollutants[48]. Bizani claimed that the effect of the pH can be explained by the electrical double layer of the solid- liquid boundary which influence the absorption- desorption mechanism of the degradation process and division of the e^-/h^+ pairs from the semiconductor surface[49].

- **Effect of the photocatalyst amount**

It is a vital point to use an optimal amount of photocatalyst to obtain an efficient degradation rate of dye. The amount of the photocatalyst depends also the light intensity, reactor design, targeted dye as well as the photocatalyst morphology. Considering this factors, many researchers used different amount of photocatalyst in their systems. It was notified that the adsorbed dye quantity on the photocatalyst surface usually rises by growing the TiO_2 amount particularly up to 1000 mg/L[50]. Caliman etc. al studied that the optimal photocatalyst amount of TiO_2 was performed 0.5 g/L [51]. In another study,

increasing the photocatalyst amount from 1 g/l to 4 g/l the dye decolorization had been enhanced significantly from 69.27% to 97.29% [52].

- **Effect of initial concentration**

The initial concentration is an important factor which should be taken into account due to the effect on the reaction kinetic. It is claimed that as the increasing the initial concentration of the dye with a fixed amount of photocatalyst, the degradation rate reduces [53]. While the dye initial concentration enhances, the more organic substances are adsorbed on the surface catalyst, as a result the photons which will reach to the semiconductor are inhibited. This will diminishes the degradation rate due to lessen the radicals had been produced in the reaction [46].

- **Effect of temperature**

Temperature has an effect on photocatalytic degradation process. It was investigated from many researchers on the photocatalytic activity. It was reported that the an increase in temperature, it rises the recombination reaction between electron and hole, this results the decreasing in photocatalytic activity [46].

1.7 LITERATURE REVIEW

Introduction

Recently, semiconductor photocatalysts have aroused considerable interest to degrade the hazardous pollutants. TiO_2 , is an essential semiconductor material which used in photocatalytic uses due to the long term chemical permanency against photo corrosive, environmentally friendly and low cost [41]. Yet, TiO_2 has some difficulties which is to reuse in the reaction medium, rapid electron-hole back reaction and wide band gap [54]. It is required to improve a novel way to reuse the photocatalytic applications. Magnetic separation is a suitable way for moving away and reusing the magnetic particles via an external magnetic field. The incorporation of magnetic particles with TiO_2 semiconductor material can prevent the recovery problem of the photocatalyst from the medium. However, magnetic particles are not stable and much more sensitive compared with titanium. In this work, we used a magnetic core to increase the separation properties

of the photocatalyst and coated with TiO₂ shell to overcome the disadvantages of the magnetic core [39].

In this work, magnetic core@ shell structure photocatalyst samples were prepared using two different synthesis methods which are vapor thermal and non-thermal. The magnetic cores were obtained using ferrite materials which are Fe₃O₄ and NiFe₂O₄ using the co-precipitation method and coating process were performed using vapor thermal and non-thermal methods. The synthesized nanomaterials were characterized by XRD, SEM, UV-DRS and Raman analysis to verify the morphological and structural characteristic of the samples. The obtained characterization results showed that the formation of the Fe₃O₄/NiFe₂O₄@TiO₂ photocatalyst by means of the average particle size is in superior harmony with the reported experimental end result according to the literature. SEM analysis was performed to examine morphological structure of the vapor thermal method samples. The band gap range of the photocatalyst was identified via UV-DRS analysis for both vapor thermal and non-thermal methods samples. Raman analysis is an analysis technique which was accomplished to examine the vibrational features of the materials further the influence of the Ni²⁺ loading to the photocatalyst.

Characterization and Modification of Fe₃O₄/NiFe₂O₄@TiO₂ Photocatalysts

At first, the Fe₃O₄@TiO₂ and NiFe₂O₄@TiO₂ photocatalysts were modified with Ni²⁺ loading. Loading process was conducted for two synthesis method vapor thermal and non-thermal method samples. The samples were characterized using XRD analysis. The XRD pattern proved that the magnetic cores (Fe₃O₄-NiFe₂O₄) could be coated with TiO₂ shell successfully. There is no impurity peaks observed which proved there was no any different phase formation. SEM analysis results showed that the photocatalysts are of spherical shape. Raman analysis results are in fine harmony with the TiO₂ phase Raman shift. Moreover, the Ni²⁺ changed the peak positions through the left. The results indicated different characteristic for the photocatalytic and photoelectrocatalytic activities. Prepared samples were investigated separately to determine the activities in the visible region wavelength. MB is a special dye which selected in place of a model molecule for observing the organic pollutants refusal from the reaction medium. The methylene blue degradation experiments were performed to elaborate the photocatalytic activity whereas the photoelectrochemical experiments were analyzed to observe the H₂ production

efficiency under visible light. PEC analysis were made using an electrode cell system contains reference, working and counter electrode. 0.1M Na₂S was used as electrolyte. The common point of the obtained results indicate that Ni²⁺ loading enhanced both photocatalytic and photoelectrocatalytic activity.

Table 1.1 shows similar study results found in the literature using the same materials to compare our results for the photoelectrochemical splitting of water molecule reactions for hydrogen generation. Moreover, Table 1.2 shows the similar dye degradation experiments results comparing with the literature works which used the same photocatalyst materials



2 MATERIALS AND METHOD

2.1 MATERIALS

2.1.1 Materials for Preparation of Photocatalysts

The materials were used for the synthesis of the magnetic cores Fe_3O_4 and NiFe_2O_4 were given.

Chemical materials which was used in the experiments are $\text{Fe}(\text{NO}_3)_3 \cdot 9\text{H}_2\text{O}$, $\text{Fe}(\text{SO}_4) \cdot 7\text{H}_2\text{O}$, PEG 20000, $\text{Ni}(\text{SO}_4) \cdot 7\text{H}_2\text{O}$, Tri ethanol amine (TEA), Titanium iso propoxide (TISOP), 25% NH_3 , propanol, ethanol. These chemicals have been purchased from Aldrich and used without any further purification.

2.1.2 Materials for Methylene Blue Degradation

Methylene Blue Degradation was materialized in a 250 ml round bottom shape two necked quartz reactor balloon. Ultrasonic water bath and a magnetic stirrer were used to get a homogeneous distribution. 300W OSRAM lamp was used as a light source. Materials which were used for the photocatalytic methylene blue degradation experiments were given.

The materials for Methylene Blue Degradation Analysis:

*Methylene Blue Solution

*Distilled Water

*Photocatalyst to be analyzed

2.1.3 Materials for Photoelectrochemical Measurements

Photoelectrochemical measurements were performed using a three electrode cell linked to an electrochemical system (Gamry potentiostat). The Ag/AgCl electrode and platinum wire were worked as a reference and counter electrodes separately. Using a spin coating technique, working electrode was formed onto ITO glass and was illuminated with a light source Asahi Solar Simulator HAL-320 Compact Xenon Light Source with 1 sun

(100mWcm⁻²) intensity. The system potential measured against to Ag/AgCl electrode was transformed to the RHE potential using the following equation (2.1):

$$E_{(RHE)} = E_{Ag/AgCl} + 0.059 * pH + E_{Ag/AgCl}^0 \quad (2.1)$$

In this equation $E_{Ag/AgCl}^0$ is 0.1967 V and Ph value equal to 13.

*ITO glass

*Ag/AgCl as a reference electrode

*Pt wire as a counter electrode

*Prepared photocatalyst

*Ethanol

*Ultrasonic Water Bath

*Spin Coater

*Gamry potentiostat

* Asahi Solar Simulator HAL-320 Compact Xenon Light Source

2.2 METHOD

2.2.1 The Fabrication of Core Composites

In a typical synthesis process, Fe (NO₃)₃.9H₂O (0.2 M Fe³⁺cations) and Fe(SO₄).7H₂O (0.1 M Fe²⁺cations) was dissolved in 400 ml distilled water with the aid of magnetic stirrer. Then, 8 g PEG 20000 was joined to the above solution. After stirring, 8 M NH₄OH solution was added till the pH value of the solution is equal to 11. After reaching the desired value, the solution kept under the ultrasonication for 30 min. Finally, the black precipitates was got with a magnet, cleaned with pure water several times and dried at 70 °C, 6 h. The same procedure was applied for the preparation of the NiFe₂O₄ magnetic core. Fe (NO₃)₃.9H₂O (Fe³⁺ cations) and Ni(NO₃)₂.6H₂O(Ni²⁺ cations) salts were used

2.2.2 The Fabrication of Fe₃O₄@TiO₂ Composites

- **The Fabrication of Fe₃O₄@TiO₂ Composites by Vapor Thermal Method**

The Fe₃O₄@TiO₂ composites were prepared by a simple vapor thermal method. As prepared Fe₃O₄ samples were dispersed in ml propanol solution with the help of ultrasonication for 10 min. After that .0.5 ml NH₃ solution was added and kept under ultrasonication for 30 min (Solution A). A mixture of 5 ml propanol and TEA (Triethanoleamine) was prepared under magnetic stirring; TISOP (Titanium isopropoxide) was added slowly to this mixture (the molar ratio of Ti: TEA = 1:2) (Solution B). Solution B was dropped slowly to the first solution and again kept ultrasonic water bath for 30 min. Prepared mixture (Solution AB) was taken to stainless steel autoclave and retained at 160°C for 24 h. The vessel that contains the Solution AB was placed in a water bath in the stainless steel autoclave to perform the vapor-thermal method. Finally, the autoclave was frozen to the room temperature, filtered, cleaned with propanol and dried at 100°C. Finally, the dried particle calcined at 450 °C for 1 h. For the preparation of the Fe₃O₄@TiO₂-Ni²⁺ photocatalyst, as prepared Solution B in the fabrication process of Fe₃O₄@TiO₂ photocatalyst, determined amount of Ni²⁺ salt (Ni²⁺:Ti⁴⁺=0.1:100) was added inside Solution B.

- **The Fabrication of TiO₂ Samples by Non-Thermal Method**

The TiO₂ nanoparticles were prepared via the sol-gel method. TISOP was used the vapor thermal method. The TISOP solution was dissolved in 20 ml ethanol and stirred for 30 min. A mixture composed of 4.2 ml acetic acid and 5 ml ethanol was stirred 1 hour and then added inside the TISOP and ethanol solution. Obtained precursor was dried at 100 °C for 3 h. Obtained powder was calcined at 450 °C for 1 h.

- **The Fabrication of Fe₃O₄@TiO₂ Composites by Non-Thermal Method**

The fabricated Fe₃O₄ magnetic cores were dissolved in 100 ml pure water for 30 min. After the dispersion of the Fe₃O₄, pure TiO₂ was added to this solution at a certain amount. This solution was kept under the ultrasonication approximately 1 h. At the end of the

loading of the TiO₂ on Fe₃O₄, the precipitates were collected by means of a magnet washed with ethanol several times. The brown color particles were dried at 110°C. Same procedure was carried out for the Fe₃O₄@TiO₂. To synthesize the Fe₃O₄@TiO₂-Ni²⁺, determined amount of the Ni²⁺ salt (Ni²⁺:Ti⁴⁺=0.1:100) was added inside the TISOP and ethanol solution at the synthesis stage of the TiO₂

2.2.3 The Fabrication of NiFe₂O₄@TiO₂ Composites

- **The Fabrication of NiFe₂O₄@TiO₂ Composites by Vapor Thermal Method**

The NiFe₂O₄@TiO₂ composites were prepared by a simple vapor thermal method. As prepared NiFe₂O₄ samples were dispersed in 6.2 ml propanol solution with the help of ultrasonication for 10 min. After that .0.5 ml NH₃ solution was added and kept under ultrasonication for 30 min (Solution A). A mixture of 5 ml propanol and TEA (Triethanoleamine) was prepared under magnetic stirring; TISOP (Titanium iso propoxide) was added slowly to this mixture (the molar ratio of Ti: TEA = 1:2) (Solution B). Solution B was dropped slowly to the first solution and again kept ultrasonic water bath for 30 min. Prepared mixture (Solution AB) was taken to stainless steel autoclave and kept at 160°C for 24 h. The vessel that contains the Solution AB was placed in a water bath in the stainless steel autoclave to perform the vapor-thermal method. Finally, the autoclave was frozen to the room temperature, filtered, cleaned with propanol and dried at 100°C. The dried particle calcined at 450 °C for 1 h. For the synthesis of the NiFe₂O₄@TiO₂-Ni²⁺ photocatalyst, as prepared Solution B in the fabrication process of NiFe₂O₄@TiO₂ photocatalyst, determined amount of Ni²⁺ salt (Ni²⁺:Ti⁴⁺=0.1:100) was added inside Solution B.

- **The Fabrication of NiFe₂O₄@TiO₂ Composites by Non-Thermal Method**

The fabricated NiFe₂O₄ magnetic cores were dissolved in 100 ml pure water for 30 min. After the dispersion of the NiFe₂O₄, pure TiO₂ was added to this solution at a certain amount. This solution was kept under the ultrasonication approximately 1 h. At the end of the loading of the TiO₂ on NiFe₂O₄, the precipitates were collected by a magnet cleaned with ethanol numerous times. The brown color particles were dried at 110°C. Same procedure was applied for the NiFe₂O₄@TiO₂-Ni²⁺. To synthesize the NiFe₂O₄@TiO₂-

Ni²⁺, determined amount of the Ni²⁺ salt (Ni²⁺:Ti⁴⁺=0.1:100) was added inside the TISOP and ethanol solution at the synthesis stage of the TiO₂

2.2.4 X-Ray-Diffraction Analysis

X-Ray analysis is an important instrument to find the crystal structure of an unknown material and identify the crystal orientation or grain for solid materials. The diffraction pattern obtained from an unknown material is compared with the pre-determined pattern diagram systematically which is to understand the relevance of the intended material.

XRD measurements were recorded on Bruker D2 PHASER over the range between $20 < \theta < 70$ with under $Cu/K\alpha$ radiation to determine the crystal size, material phase and impurity of the materials. To calculate the crystal size of the prepared samples we applied Debby-Scherrer equation (2.2)

$$D = \frac{K\lambda}{\beta \cos \theta} \quad (2.2)$$

In which D represents the mean particle size, K is a crystal constant which is equal to 0.9, λ identifies the X-ray radiation wavelength, β is the full width at half maximum (FWHM; calculated from origin program) in radians, θ is the Braggs angle.

2.2.5 UV-Visible Diffuse Reflectance Spectroscopy (UV-DRS) Analysis

UV- DRS analysis is used to measure the ability to absorb light of a photocatalyst sample. The optical observable fact known as diffuse reflectance is generally used from UV-visible to IR regions. Each molecule absorbs light by wavelength difference according to its own physical character.

UV-visible diffuse reflectance spectroscopy was performed with PG device T92+ spectrophotometer. Pure barium sulfate was chosen as a reference material. The measurements was recorded between range of 230 and 900 nm. With this analysis, both reflectance and the band gap value of the photocatalyst can be measured. The band gap of the photocatalyst is considered by Kubelka-Munk expression (2.3) [55].

$$(h\nu\alpha)^{1/n} = A(h\nu - E_g) \quad (2.3)$$

In this equation E_g is the band gap energy (eV), h is Planck constant ($4.135 \times 10^{-15} \text{ eV.s}$), ν is the frequency, A is the proportionality constant; α is the optical absorption coefficient and n is a factor that depends on the kind of optical transition induced by photon absorption (1/2 and 2 for direct and indirect transitions, respectively). By applying $n=2$, the direct band gap energy was estimated. $(h\nu f(R))^2 - h\nu$ graphs was drawn and the slope of the linear area gave the band gap energy[56].



Figure2.1: UV-Visible Diffuse Reflectance Spectroscopy Instrument

2.2.6 Scanning Electron Microscopy Analysis (SEM)

SEM analysis is a method that obtains information about the size and morphology of the analyzed material. The analysis is performed by displaying the structure of the materials in high resolution. In this way, the morphological structure and size of the material can be informed by SEM analysis.

Accelerated electrons in SEM carry a significant amount of kinetic energy and this is spread out a range of signals created by electron and sample interaction. These signals produce SEM images.

In our work, as prepared four samples was analyzed by SEM to examine the shape and size of the materials even nanorod or nanosphere etc.

2.2.7 Energy Dispersive X-Ray Spectroscopy (EDS) Analysis

Energy Dispersive X-Ray spectroscopy is a standard methodical technique which is performed to determine the sample elemental compositions in a minor quantity. In a properly armed SEM, the atoms on the sample surface are excited and the X-Ray

wavelengths are emitted due to the characteristic atomic structure of the elements. These X-Rays can be observed from an energy dispersive detector. Suitable elements which are of valid amounts can be detected and yielded considering the compositions of the atoms. It is defined as EDS and is beneficial for the composition analysis[57].

2.2.8 Raman Spectroscopy Analysis

The energy of a molecule be parts of partially transitional energy, partially rotational, vibrational and electronic energy according to the characteristic properties. In Raman, the sample is exposed by strong laser in the UV-visible region and the light which is scattered is generally detected in the direction perpendicular to the beam. The light which is sent to the sample is of two type: Rayleigh scattering which is powerful and Raman scattering which is too weak as shown in Figure 2.2 [58]

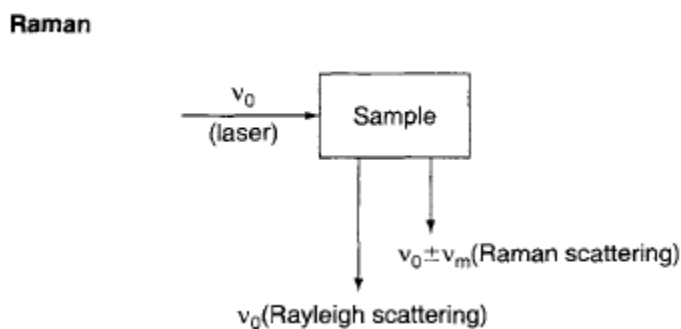


Figure2.2: Raman Scattering Mechanism[58]

Raman analysis is a vibrational spectroscopic methods used to supply on molecular vibration and material structure. This method uses a light comes from a laser to illuminate the sample and produces infinitesimal amount of spotted Raman light which is converted a Raman spectrum via a camera. The pattern of the Raman spectrum offers to identify substances and investigate the crystallinity, orientation, tracking changes of the sample. A Raman spectrum is represented as an intensity–wavelength shift [59].

In this work, we investigated the structural properties of the prepared samples with Raman analysis. A Raman spectrum was performed with STEX 100 Raman spectroscopy instrument.

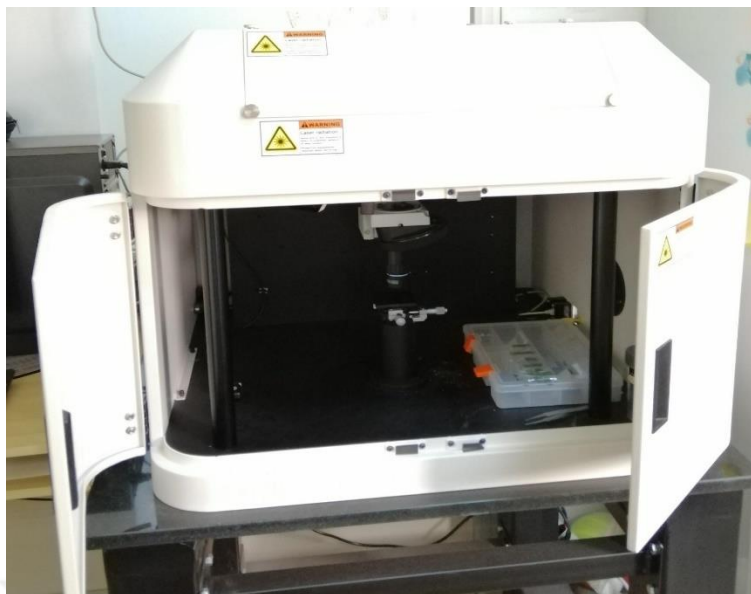


Figure2.3: Raman Spectroscopy Instrument

2.2.9 Photoelectrochemical Activity Measurements

The photoelectrochemical measurements was performed via a three electrode cell linked to an electrochemical system which is also illuminated a visible light source set light intensity equal to $100\text{mW}/\text{cm}^2$ (1 sun).The Pt wire and Ag/AgCl electrodes used as a counter electrode and reference electrode, respectively. The working electrode was covered on an ITO glass using spin coating method and $0.1\text{M Na}_2\text{S}$ was used as an electrolyte.

2.2.9.1 Linear Sweep Voltammetry

Voltammetry is basically a method that the potential of the working electrode is controlled and increased over time linearly and the current is measured according the applied potential which is written as a function of applied potential. Linear sweep voltammetry analysis was carried out so as to the photo-response of the prepared photoanode check between 0.5V and 1.4 V (vs. RHE).

2.2.9.2 Chronoamperometry

Chronoamperometry is an electrochemical technique in which the potential of the working electrode is analyzed and the resultant current is measured as a function of time

and interpreted current vs. time. In our work, chronoamperometry measurements were performed by 100mW/cm² (1 sun) light intensity and at 0 V applied potential.

2.2.9.3 Mott-Schottky Analysis

Mott-Schottky analysis is basically based on the measurement of the capacitance value of the photoanode comparing by varying potential of the working electrode. As a result of the Mott-Schottky analysis the 1/C²-V graph is obtained[60]. According to this graph, the flat band potential E_{fb} and the charge carrier density can be determined by the Mott-Schottky equation (2.4).

$$\frac{1}{C^2} = \frac{2}{\varepsilon_0 \varepsilon_r e N_{Dopant} A_s^2} \left(E_{app} - E_{fb} - \frac{KT}{e} \right) \quad (2.4)$$

According to this relation; C stands for the capacitance, e is the charge of an electron (1.602 × 10⁻¹⁹ coulomb), ε₀ is the permittivity in vacuum, A represents the surface area, ε_r is the relative permittivity of the semiconductor, N_{Dopant} is the donor density or free carrier density, K is the boltzman constant, T represents the temperature, E_{app} represents the applied potential [61]. In Mott Schottky graph, the slope of the linear area gives the N_{Dopant} value which is the value of the x-axis.

Besides this, from the Mott-Schottky graph space charge layer thickness W, can be considered by using the following equation (2.5)

$$W = \left(\frac{2\varepsilon_0 \varepsilon (E_{app} - E_{fb})}{e N_{Dopant}} \right)^{1/2} \quad (2.5)$$

Mott-Schottky analysis was performed in dark conditions at 1000 Hz frequency and 10 mV AC voltages.

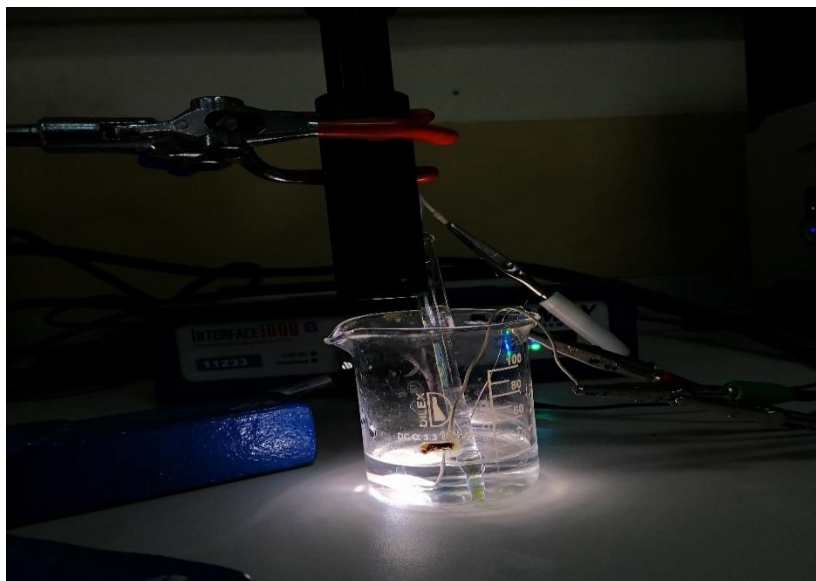


Figure 2.4: Three electrode photoelectrochemical cell reaction system under the visible light ($\lambda > 400$ nm)

2.2.10 Photocatalytic Methylene Blue Degradation Analysis

Photocatalytic efficiencies of the samples were performed by the decolorization of methylene blue dye under visible light. MB dye was selected as the model molecule for photocatalytic degradation because of it is widely used and was illuminated with 300 W OSRAM Xenon lamp. The time evolution of the MB absorbance peak at $\lambda \approx 664$ nm is used to calculate the kinetic parameter. The reactor balloon was placed in a home-made reactor box. In our experiments, 0.5 g of samples was measured and balanced in 100 ml methylene blue solution (10 ppm). The solution of MB was continuously stirred in the dark condition about 45 min to get absorption-desorption equilibrium among the MB, photocatalyst and water. The prepared mixture was illuminated approximately 3 h. A certain mixed solution was extracted and filtered to set apart the photocatalyst and the clean mixture was taken to detect the absorbance value by using UV-vis spectrophotometer. The sample was taken for 15 min. during the first 1.5 h. then samples were taken every 30 min. and the absorbance was measured with UV-vis spectroscopy instrument. Calibration curve was generated to find the concentration according to obtained absorbance values at 664 nm wavelength.

Methylene blue degradation rate was calculated with following equation (2.6)[59].

$$\% \text{ Degradation efficiency} = \frac{C_0 - C_t}{C_0} \times 100 \quad (2.6)$$

C_0 =Methylene blue concentration at initial time,

C_t =Methylene blue concentration at time t,

Langmuir–Hinshelwood rate expression is an expression which is used to characterize the kinetic behavior of the photocatalyst can be comply well with the connection between the first decolorization rate and the concentration of the methylene blue dye designed for heterogeneous photocatalytic processes occurring at the solid–liquid boundary[24, 56].

Langmuir-Hinshelwood kinetic model was given the following equation (2.7)

$$r = \frac{dC_{MB}}{dt} = \frac{k \times K \times C_{MB}}{1 + K \times C_{MB}} \quad (2.7)$$

r=initial disappearance rate of the dye;

C_{MB} = equilibrium dye concentration

t=time of the reaction;

K = the equilibrium constant for the adsorption of the organic dye onto catalyst;

k = reaction rate constant.

When the dye concentration is exceptionally small, $K \times C_{MB}$ is very small check against to 1, the term $K \times C_{MB}$ can be unimportant. The equation then was integrated with respect to t, so it was obtained pseudo first order kinetic model as seen in equation 2.8. The term $k \times K$ was used as k_{app} in the converted equation (2.8).

$$-\ln \frac{C_{MBt}}{C_{MB0}} = k_{app} \times t \quad (2.8)$$



Figure2.5: Photocatalytic Methylene Blue Degradation Reaction System

Table 2.1 was designed to classify the characterization techniques used to characterize the vapor thermal and non-thermal method. It is showed that the performed characterization and activity measurements which was applied during the studies. In this work, materials with the same characteristic and physical properties were produced using two different methods (which are vapor thermal and non-thermal method) and compared the photocatalytic and photoelectrocatalytic activities, the optical properties by UV-DRS analysis and vibrational and characteristic properties by Raman analysis. XRD and SEM analysis were only performed for the materials which produced by vapor thermal method.

Table 2.1: The classification of the photocatalysts according to the characterization method applied in this work

Synthesized Photocatalysts	VAPOR THERMAL METHOD							NON-THERMAL METHOD					
	XRD	SEM	UV-DRS	Raman	PEC	MB	EDS	XRD	SEM	UV-DRS	Raman	PEC	MB
$\text{Fe}_3\text{O}_4@\text{TiO}_2$	X	X	X	X	X	X				X	X	X	X
$\text{Fe}_3\text{O}_4@\text{TiO}_2\text{-Ni}^{2+}$			X	X	X	X	X			X	X	X	X
$\text{NiFe}_2\text{O}_4@\text{TiO}_2$	X	X	X	X	X	X				X	X	X	X
$\text{NiFe}_2\text{O}_4@\text{TiO}_2\text{-Ni}^{2+}$			X	X	X	X				X	X	X	X

3 RESULTS AND DISCUSSION

3.1 X-Ray Diffraction (XRD) Analysis Results

The prepared photocatalysts were investigated with X-Ray Diffraction analysis to identify the phase structure and crystal size of materials.

XRD pattern of the Fe_3O_4 showed a series characteristic peaks located between the $20 < 2\theta < 70$ which is fitted well the Fe_3O_4 samples (JCPDS card No.19-0629). The observed diffraction peaks of the prepared Fe_3O_4 samples showed cubic phase and no contamination peaks are observed which point out that prepared Fe_3O_4 samples is clean (Figure 3.1).

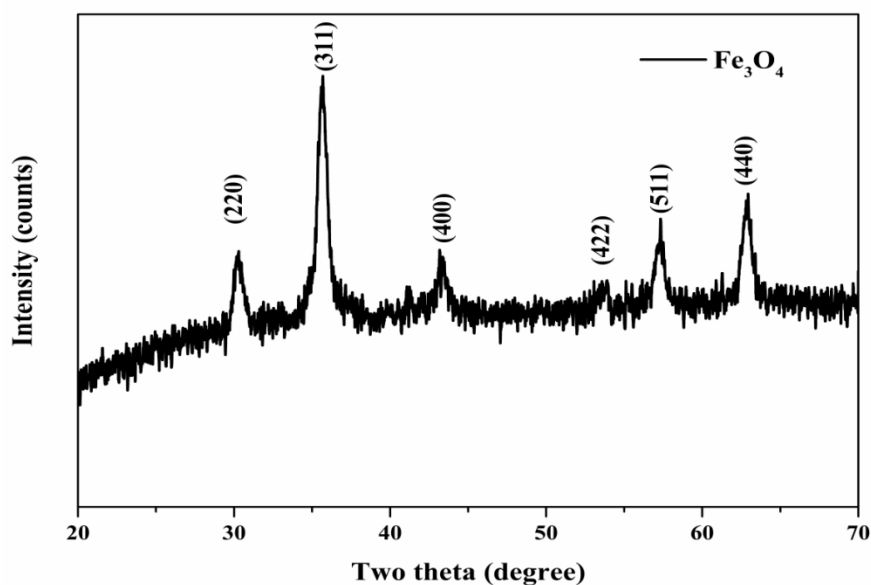


Figure 3.1: XRD pattern of the Fe₃O₄ photo-catalyst

The diffraction peaks at 2θ values of 30.24° , 35.75° , 43.36° , 53.66° , 62.90° which can be attributed respectively to the (220), (311), (400), (422), (511), (440) diffraction planes of the cubic phase Fe₃O₄ (JCPDS card No. 19-0629)[62]. The crystallite size of the Fe₃O₄ photo-catalyst was given Table 3.1.

XRD pattern of the TiO₂ showed a series characteristic peaks located between the $20 < 2\theta < 70$ which is fitted well the TiO₂ samples. The observed peaks of the prepared TiO₂ samples showed single phase tetragonal structure and no pollution peaks are observed which indicate that prepared TiO₂ samples is pure .

The diffraction peaks at 2θ values of 25.71° , 38.47° , 48.33° , 55.18° , 63.09° which can be recognized respectively to the (101), (103), (200), (211) and (213) diffraction planes of the tetragonal phase TiO₂ (JCPDS card No.00-021-1272).The diffraction peak of the TiO₂ pattern showed the characteristic anatase and rutile phase characteristic peaks. According to XRD pattern (211) and (002) planes are of rutile phase characteristic peaks whereas (101), (103) and (200) planes are of anatase phase characteristic peaks as shown in Figure 3.2. The crystallite size of the TiO₂ was given in Table 3.1.

XRD pattern of the Fe₃O₄@TiO₂ samples showed both Fe₃O₄ (magnetite) and TiO₂ characteristic peak as shown in Figure 3.2. By comparing the peaks of the TiO₂ and Fe₃O₄@TiO₂ sample it is found that Fe₃O₄ (magnetite) could be coated well with TiO₂ shell properly. And it is clear that XRD diffraction peak intensities of Fe₃O₄ have been

decreased with coating of TiO₂. There were any additional peaks showed indicates that there was no new phase creation between Fe₃O₄ and TiO₂

XRD pattern of the NiFe₂O₄@TiO₂ samples was depicted in Figure 3.2. NiFe₂O₄ contains several characteristic peaks at 2θ values of 18.39°, 30.29°, 35.70°, 37.31°, 43.36°, 53.80°, 57.36°, 62.92° which were assigned to the (111), (220), (311), (222), (400), (422), (511) and (440) (JCPDS No. 54-0964) which indicates the crystal system of the spinel NiFe₂O₄, respectively [63, 64]. In XRD pattern, the peaks of NiFe₂O₄@TiO₂ sample showed mostly TiO₂ characteristic peaks and some of the NiFe₂O₄ characteristic peaks couldn't be seen. It can be related that TiO₂ is successfully coated on the surfaces of the NiFe₂O₄. Besides, no impurity peaks proved that there was not another formation between NiFe₂O₄ and TiO₂.

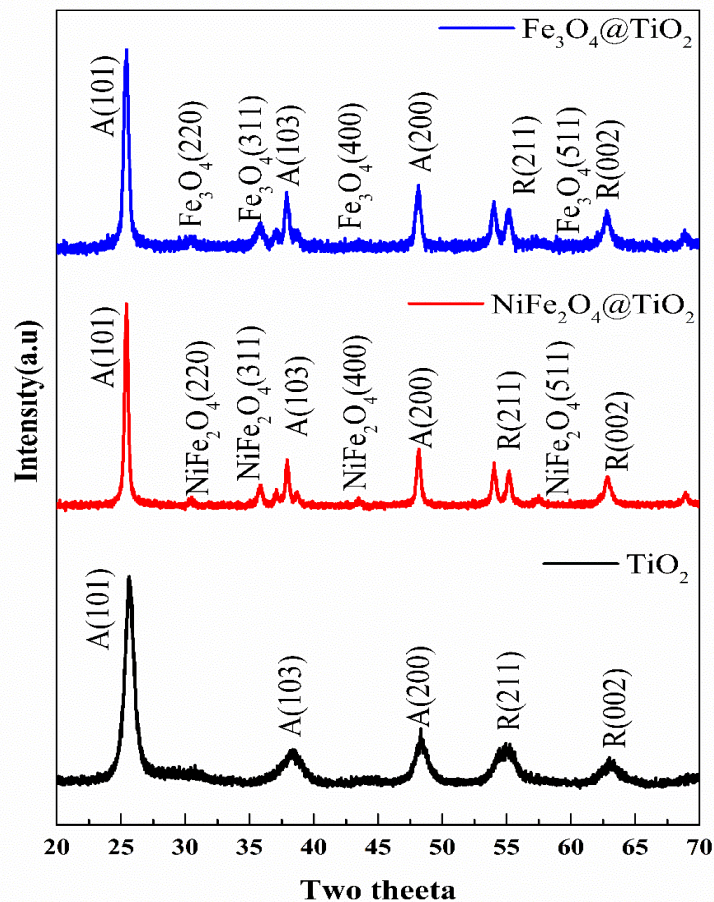


Figure 3.2: XRD pattern of the TiO₂, NiFe₂O₄@TiO₂ and Fe₃O₄@TiO₂ photo-catalyst (A: Anatase phase; R: Rutile phase)

Table 3.1: Measured Crystallite sizes of the Prepared Photo-catalyst

Synthesized Photocatalyst	2 θ (Angle)	FWHM(Calculated from Origin)	Crystallite Size(nm)
TiO ₂	25.67	0.94084	8.663865
Fe ₃ O ₄	35.77	22.18933	0.376361
Fe ₃ O ₄ @TiO ₂	25.41	0.48815	16.97314
NiFe ₂ O ₄ @TiO ₂	25.43	0.36203	22.50484

3.2 UV-Visible Diffuse reflectance Analysis Results

In diffuse reflectance spectroscopy the instrument procedures the diffusely reflected light. The Tauc- plots (plot of $h\nu f(R)$ vs. photon energy ($h\nu$)) which were used to calculate the direct band gap values were drawn from the reflectance measurements using the conversion of Kubelka–Munk function (equation 3.1).

$$f(R) = \frac{(1-R)^2}{2R} \quad (3.1)$$

In the case of diffuse reflectance measurements Kubelka–Munk function of the reflectance ($f(R)$) which is comparative to the absorption coefficient, α which was used to calculate the direct band values from Tauc-plots [65]. The band gap is an important criteria for effective photo-catalytic and photo-electro-catalytic applications which should be between the range $1.23 < E_g < 3.0$ eV [34]. Our main objective is to synthesize our photo-catalyst in the appropriate band gap range. Thus, we optimized the molar ratio among the magnetic core and TiO₂ shell.

UV-Visible DRS spectra results of bare TiO₂, Fe₃O₄@TiO₂ and Fe₃O₄@TiO₂-Ni²⁺ were obtained between 300 and 800 nm. Reflectance measurements were made with UV-DRS instrument. As depicted in Figure 3.3, the reflectance spectra of the Fe₃O₄@TiO₂ sample lower than the pure TiO₂.

It was seen that the effectiveness of the Fe₃O₄ was increased with the TiO₂ coating especially between 600-800 nm wavelengths. Coating Fe₃O₄ with the TiO₂ decreased the

band gap value of the TiO_2 whereas the absorption in visible light spectrum had increased. Moreover, Ni^{2+} loading had decreased the band gap value of the $\text{Fe}_3\text{O}_4@\text{TiO}_2$ significantly. The band values were shown in Table 3.2.

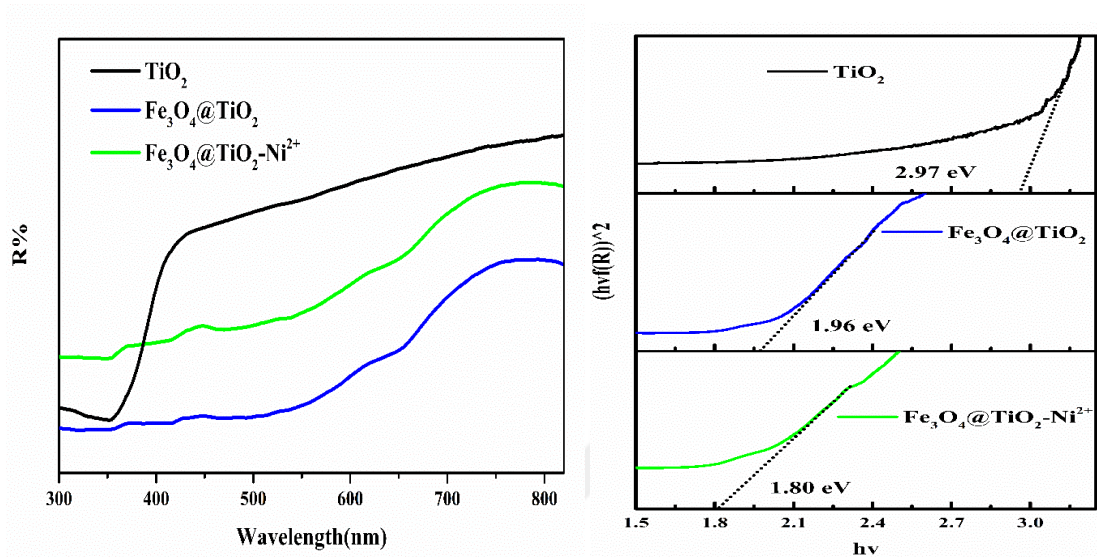


Figure 3.3: UV-DRS spectra and Tauc plots of the photocatalyst TiO_2 , $\text{Fe}_3\text{O}_4@\text{TiO}_2$, $\text{Fe}_3\text{O}_4@\text{TiO}_2-\text{Ni}^{2+}$ synthesized by vapor thermal method

UV-DRS analysis result of the non-thermal method $\text{Fe}_3\text{O}_4@\text{TiO}_2$ was depicted in figure 3.4. The sample was prepared by the non-thermal method. The reflectance spectra of the sample showed mostly the same characteristic pattern when compared the vapor thermal method. However, as it can be seen from the figure, non-thermal method photocatalyst had broadened the spectra intensity through the visible region more than that the vapor thermal method. The band gap value of the $\text{Fe}_3\text{O}_4@\text{TiO}_2$ photocatalyst has the same band gap energy which is equal to 1.96 eV.

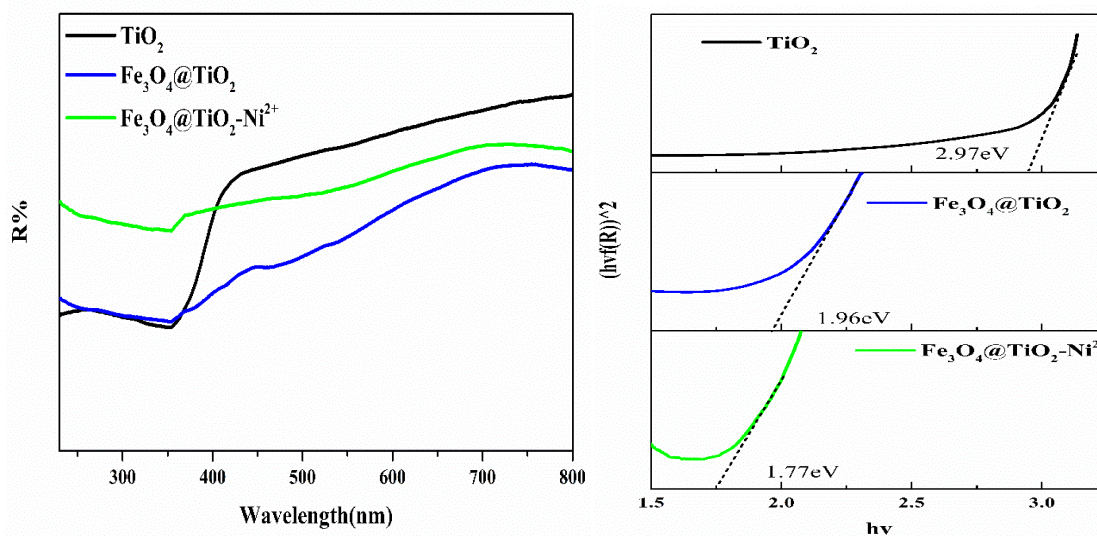


Figure 3.4: UV-DRS spectra and Tauc plots of the photocatalyst TiO₂, Fe₃O₄@TiO₂, Fe₃O₄@TiO₂-Ni²⁺ synthesized by non-thermal method

UV-Visible DRS spectra results of TiO₂, NiFe₂O₄@TiO₂ and NiFe₂O₄@TiO₂-Ni²⁺ were obtained between 300 and 800 nm. NiFe₂O₄ is known as a p-type semiconductor having narrow band gap which is known as magnetic material and photo-catalyst [38]. NiFe₂O₄ has increased the effectiveness in the visible region by coating with TiO₂ shell. Band gap of the NiFe₂O₄@TiO₂ composite was measured with the Tauc plot and shown in Table 1.3. Besides this, NiFe₂O₄@TiO₂ composite was load with Ni²⁺ ion to repress the e⁻/h⁺ back reaction rate especially in photo-catalytic and photo-electro-catalytic applications. By comparing the reflectance results with the Ni²⁺ load NiFe₂O₄@TiO₂, it can be seen that (from the figure 3.5) the reflectance value of NiFe₂O₄@TiO₂-Ni²⁺ photo-catalyst was increased prominently in the visible region. This increase can be associated with the decrease of the band gap.

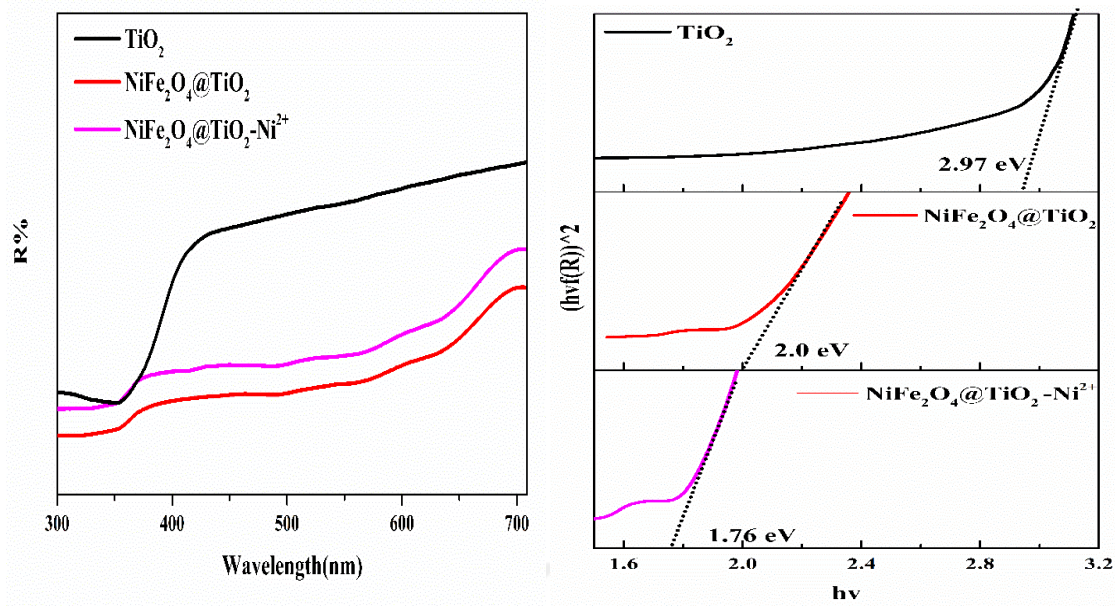


Figure 3.5: UV-DRS spectra and Tauc plots of the photocatalyst TiO_2 , $\text{NiFe}_2\text{O}_4@\text{TiO}_2$ and $\text{NiFe}_2\text{O}_4@\text{TiO}_2\text{-Ni}^{2+}$ synthesized by vapor thermal method

UV-DRS analysis of the non-thermal method $\text{NiFe}_2\text{O}_4@\text{TiO}_2$ and $\text{NiFe}_2\text{O}_4@\text{TiO}_2\text{-Ni}^{2+}$ photocatalyst was shown in Figure 3.6. The reflectance measurements depicted in graph showed different pattern when we compare the vapor thermal method photocatalysts. The band gap value of the $\text{NiFe}_2\text{O}_4@\text{TiO}_2$ photocatalyst had decrease after the Ni^{2+} loading. It is obvious that the band gap values for both of the synthesis method are almost equal to each other.

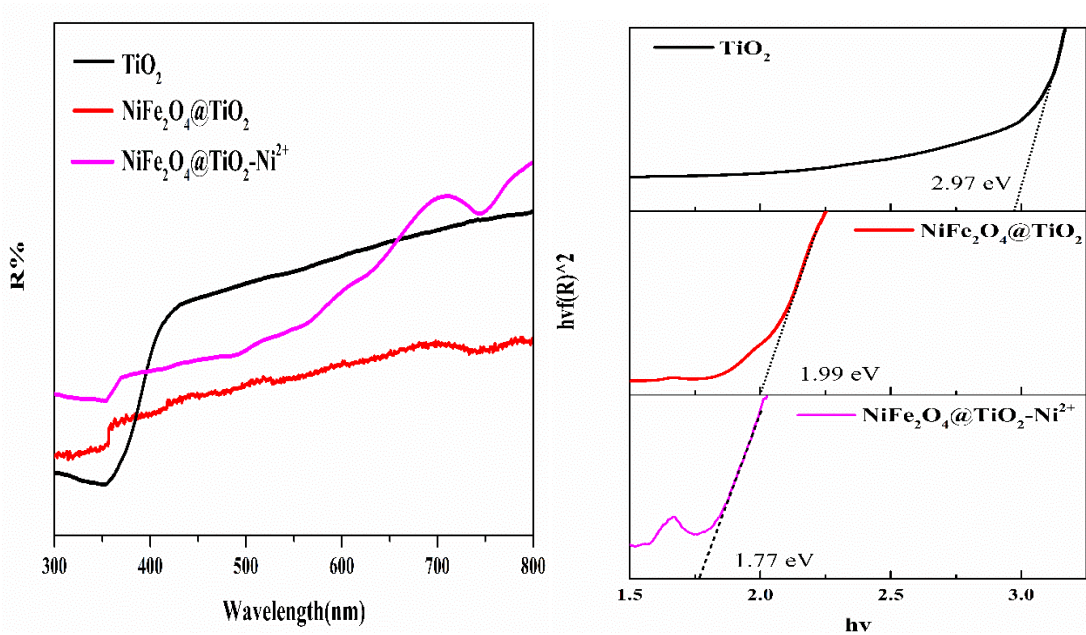


Figure 3.6: UV-DRS spectra and Tauc plots of the photocatalyst TiO_2 , $\text{NiFe}_2\text{O}_4@ \text{TiO}_2$ and $\text{NiFe}_2\text{O}_4@ \text{TiO}_2\text{-Ni}^{2+}$ synthesized by non-thermal method

Table 3.2: Obtained Band Gap Values of the prepared photocatalyst

Prepared Photocatalyst	Vapor Thermal Method Band Gap Values (eV)	Non-thermal Method Band Gap Values(eV)
Fe_3O_4	1.40	1.40
TiO_2	2.97	2.97
$\text{Fe}_3\text{O}_4@ \text{TiO}_2$	1.96	1.96
$\text{Fe}_3\text{O}_4@ \text{TiO}_2\text{-Ni}^{2+}$	1.80	1.77
NiFe_2O_4	1.56	1.56
$\text{NiFe}_2\text{O}_4@ \text{TiO}_2$	2.0	1.99
$\text{NiFe}_2\text{O}_4@ \text{TiO}_2\text{-Ni}^{2+}$	1.76	1.77

3.3 Scanning Electron Microscopy (SEM) Analysis Results

As synthesized four photocatalyst samples SEM analysis was performed. Figure 3.7 shows the typical SEM images of the $\text{Fe}_3\text{O}_4@ \text{TiO}_2$ and $\text{Fe}_3\text{O}_4@ \text{TiO}_2\text{-Ni}^{2+}$ nanocomposites. The images of prepared photocatalyst reveal that the shape of $\text{Fe}_3\text{O}_4@ \text{TiO}_2$ and $\text{Fe}_3\text{O}_4@ \text{TiO}_2\text{-Ni}^{2+}$ are a nanosphere. According to obtained images, the shape of the $\text{Fe}_3\text{O}_4@ \text{TiO}_2$ and $\text{Fe}_3\text{O}_4@ \text{TiO}_2\text{-Ni}^{2+}$ nanocomposites is spherical shape, with a diameter of 50 nm.

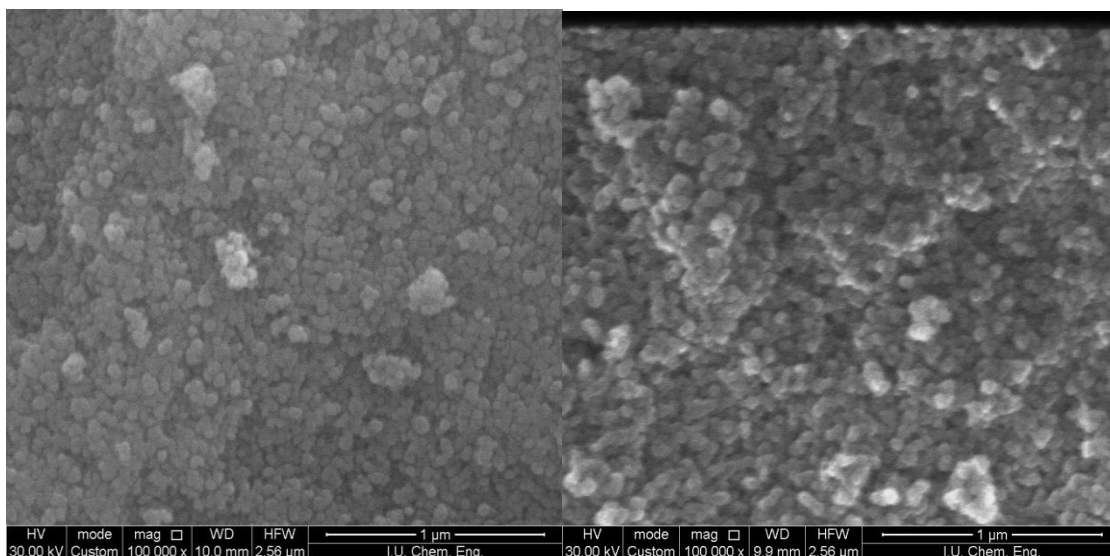


Figure 3.7: SEM images of the $\text{Fe}_3\text{O}_4@\text{TiO}_2$ and $\text{Fe}_3\text{O}_4@\text{TiO}_2\text{-Ni}^{2+}$ photo-catalyst, respectively

As synthesized four photo-catalyst samples SEM analysis was performed at different magnifications. Figure 3.8 shows the typical SEM images of the $\text{NiFe}_2\text{O}_4@\text{TiO}_2$ samples. The images of prepared photo-catalyst at different magnifications reveal that the shape of $\text{NiFe}_2\text{O}_4@\text{TiO}_2$ is a nanosphere same as $\text{Fe}_3\text{O}_4@\text{TiO}_2$. According to the obtained figure, the diameter of the photocatalyst is 62.5 nm. According to the obtained diameter, it is said that the catalyst surface of the $\text{NiFe}_2\text{O}_4@\text{TiO}_2$ is higher than the $\text{Fe}_3\text{O}_4@\text{TiO}_2$

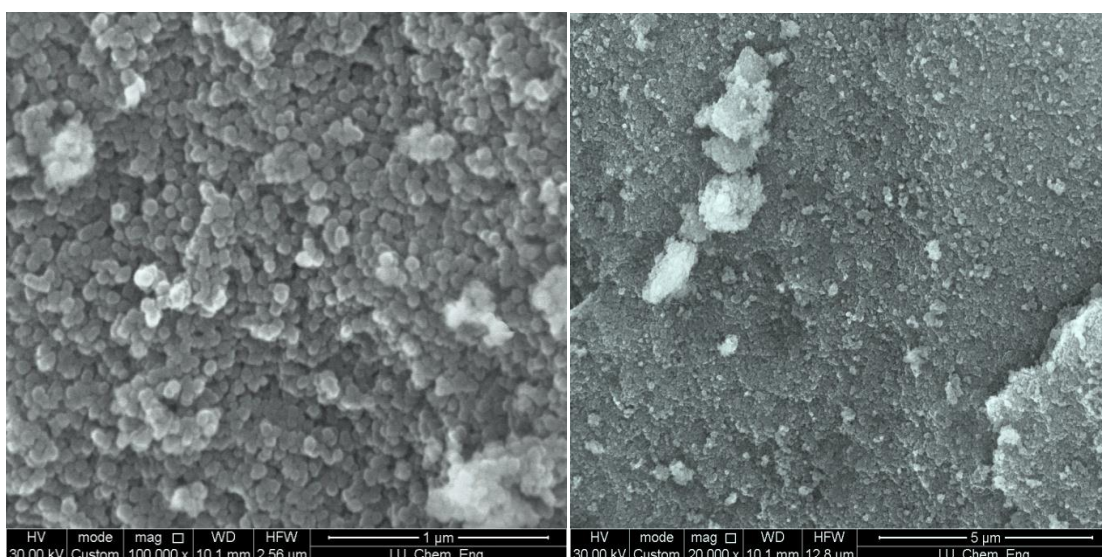


Figure 3.8: SEM images of the $\text{NiFe}_2\text{O}_4@\text{TiO}_2$

3.3.1 Energy Dispersive X-Ray Spectroscopy (EDS) Analysis

EDS is a chemical analysis method used in combination with SEM analysis technique. EDS analysis was performed to identify the chemical composition. The loading of the transition metal Ni^{2+} was used to suppress the recombination rate of the photoexcited e^-/h^+ pairs. It was depicted that loading could be managed successfully. As shown in Figure 3.9 that Ni^{2+} can be found inside the $\text{Fe}_3\text{O}_4@\text{TiO}_2\text{-Ni}^{2+}$ photocatalyst. The chemical synthesis ratio of the Ni^{2+} load $\text{Fe}_3\text{O}_4@\text{TiO}_2$ is $\text{Ni}^{2+}:\text{Ti}^{4+}=0.1:100$. Considering this ratio the weight ratio of the Ni^{2+} was found the same weight ratio which is 0.1 as can be seen in the weight ratio in Figure 3.9. It is clear that the Ni^{2+} loading was accomplished effectively.

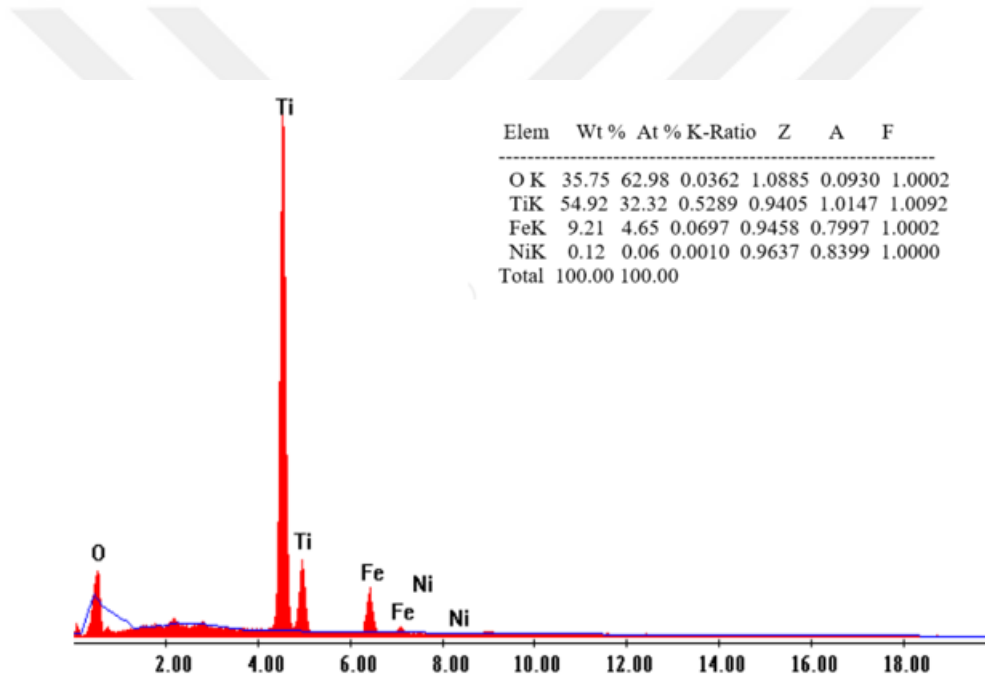


Figure 3.9: EDS Analysis result of the $\text{Fe}_3\text{O}_4@\text{TiO}_2\text{-Ni}^{2+}$ photocatalyst

In Figure 3.10 shows the SEM images of the region where the EDS analysis was performed. It is clear that Ni^{2+} loading formed perforated structure on the surface of the $\text{Fe}_3\text{O}_4@\text{TiO}_2$ structure. Same perforated regions had been observed on the $\text{NiFe}_2\text{O}_4@\text{TiO}_2$ surface.

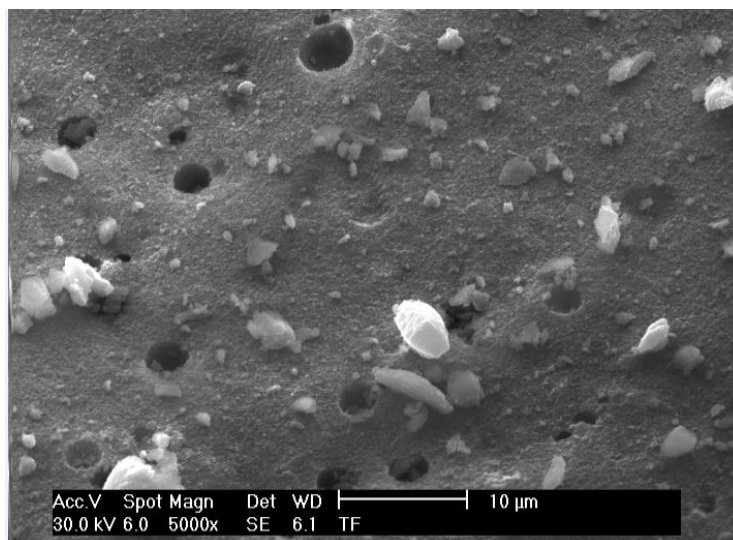


Figure 3.10: SEM images for the EDS Analysis performed for the $\text{Fe}_3\text{O}_4@\text{TiO}_2\text{-Ni}^{2+}$ photocatalyst

3.4 Raman Spectroscopy Results

Magnetite shows five main Raman bands is of a spinel structure which is three of them T_g , one E_g and one A_{1g} . Main peak positions for Fe_3O_4 is 300, 532 and 661 cm^{-1} that have been reported in the literature [66, 67]. At higher laser power, hematite can be formed and it is known that the sensitivity to laser power can exhibit different band positions especially for Fe_3O_4 [59]. Raman spectra of magnetic core Fe_3O_4 (magnetite) was performed and depicted in Figure 3.11.

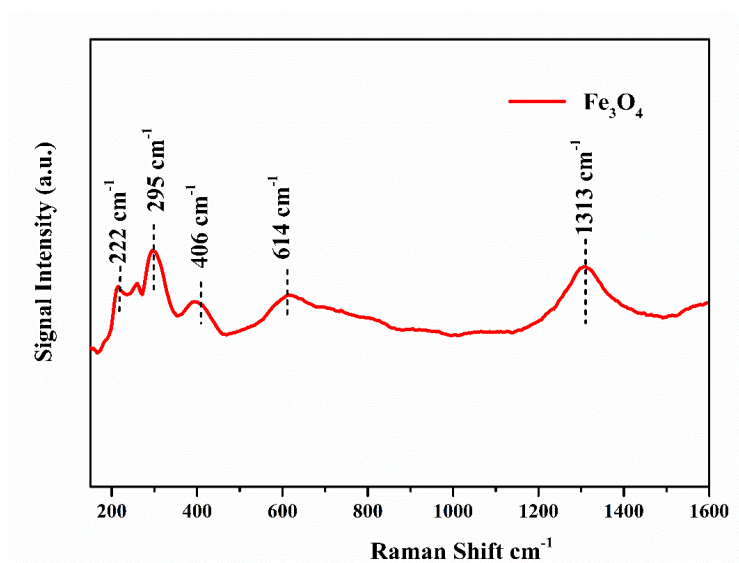


Figure 3.11: Raman spectra of the Fe_3O_4

Raman spectra analysis of prepared $\text{Fe}_3\text{O}_4@\text{TiO}_2$ and $\text{Fe}_3\text{O}_4@\text{TiO}_2\text{-Ni}^{2+}$ samples were performed. According to the Raman spectra of $\text{Fe}_3\text{O}_4@\text{TiO}_2$ core-shell composites the peaks obtained are the peaks of TiO_2 . Thus, we can attribute this result to the coating of Fe_3O_4 core with TiO_2 shell was successfully completed. The frequency of the Raman bands is well-known that TiO_2 has four characteristic peak which can be linked to the anatase phase 352, 425, 545 and 668 [62, 68].

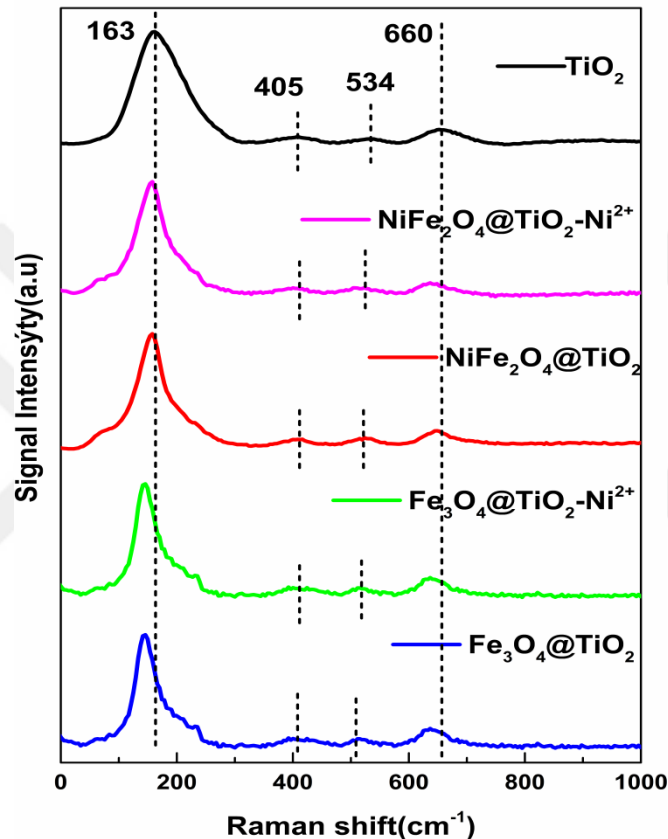


Figure 3.12: Raman spectra of the TiO_2 , $\text{Fe}_3\text{O}_4@\text{TiO}_2$, $\text{Fe}_3\text{O}_4@\text{TiO}_2\text{-Ni}^{2+}$, $\text{NiFe}_2\text{O}_4@\text{TiO}_2$ and $\text{NiFe}_2\text{O}_4@\text{TiO}_2\text{-Ni}^{2+}$ prepared by vapor thermal method

Raman spectra analysis of prepared samples was performed under laser power at 5mV. As shown in Figure 3.10, there are four main. These results point out that TiO_2 dominates the crystalline form of the photocatalyst which also showed that NiFe_2O_4 was coated with TiO_2 shell successfully. By comparing the Raman shift positions of the $\text{NiFe}_2\text{O}_4@\text{TiO}_2$ and pure TiO_2 , band position of the TiO_2 photocatalyst shifted to the left under the effect of the magnetic core NiFe_2O_4 . This result can be associated due to the fact that the molecular weight of Ni^{2+} (molecular mass: 58.6934 g/mole) ion has higher than Ti^{4+} ion

(molecular mass:47.867 g/mole). With this result the addition of Ni^{2+} on the NiFe_2O_4 @ TiO_2 composites shifted the band positions to the left[69]. It was observed that each contribution further decreased the signal intensity.

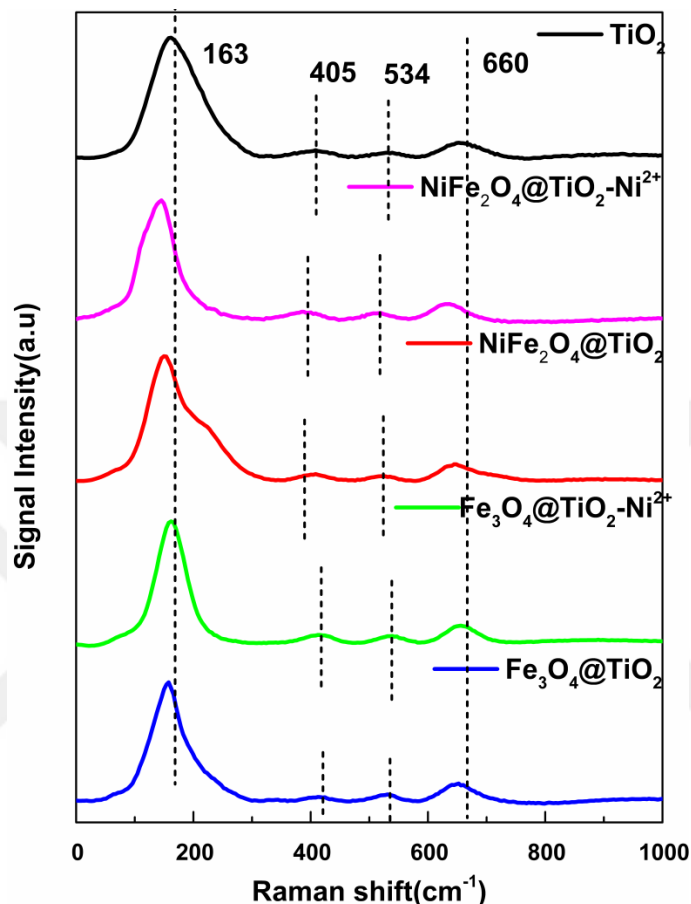


Figure3.13: Raman spectra of the TiO_2 , Fe_3O_4 @ TiO_2 , Fe_3O_4 @ TiO_2 - Ni^{2+} , NiFe_2O_4 @ TiO_2 and NiFe_2O_4 @ TiO_2 - Ni^{2+} prepared by non-thermal method

Raman spectra results of the photocatalyst materials synthesized by non-thermal method were depicted in the figure 3.12. It is clear to see that all samples have shown TiO_2 phase characteristic peak same as vapor thermal method photocatalyst. As requested, the magnetic cores were coated with TiO_2 semiconductor. Loading with Ni^{2+} was changed the Raman shift through the left. This change can be seen clearly for the NiFe_2O_4 @ TiO_2 photocatalyst loading with Ni^{2+} ion. The shifting through the left can be attributed to the molecular weight difference between the Ni^{2+} and Ti^{4+} ion. In conclusion, it is obvious that TiO_2 coating can be managed effectively for both of the synthesis technique

3.5 Photoelectrochemical Activity Measurement Results

- **Optimization of the Photo-Electrodes**

Photoelectrochemical activity measurement was performed using LSV, Chronoamperometry and Mott Schottky analysis. Before the photo-electrochemical activity measurements, the photo-electrodes were optimized to obtain the highest efficiency. Electrolyte optimization, thickness optimization and heat optimization were performed and the best results were chosen to perform the photoelectrochemical analysis.

- **Optimization of the Electrolyte**

Defining the electrolyte selection depends on the basic characteristics of the semiconductor material and also depends on the deposition technique. In this work, we used spin coating technique. If material stability is unknown, neutral medium is the best way to start[22].According to the literature the most stable medium for metal oxide semiconductor materials is that the alkaline medium[34, 60, 62, 70].In the light of this information, we used methanol, Na₂S, NaOH as electrolyte and performed chronoamperometry analysis. The highest current was obtained in the 0.1 M Na₂S medium. The photo-current values of Fe₃O₄@TiO₂ photo-catalyst in CH₃OH (methanol), NaOH and Na₂S mediums respectively is that 1.4, 1 and 13 $\mu\text{A}/\text{cm}^2$ under the visible light illumination.

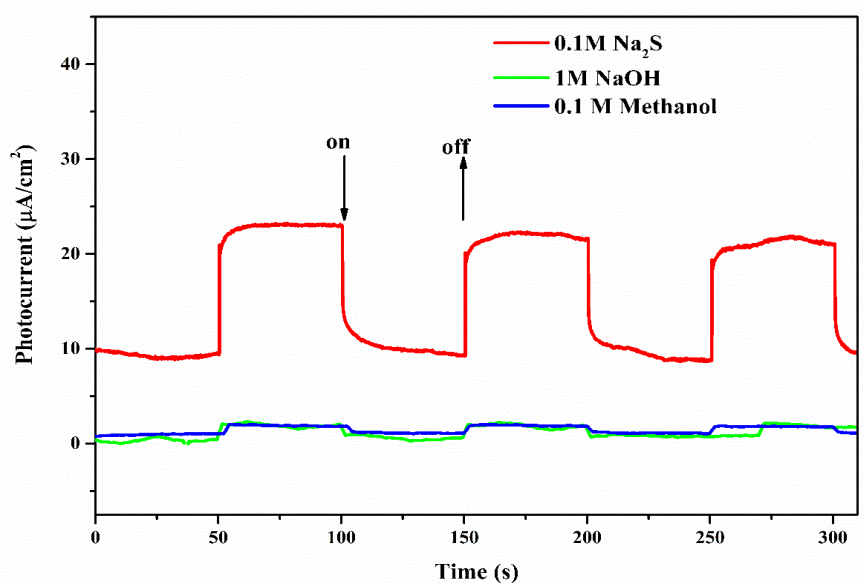


Figure3.14: Chronoamperometry analysis of the $\text{Fe}_3\text{O}_4@\text{TiO}_2$ photo-catalyst in the medium of methanol, Na_2S , and NaOH

- **Optimization of the Photo-Electrode Thickness**

After choosing the electrolyte, we had optimized the thickness of the photo-electrode. In our work, we used the spin coater instrument to deposit the photo-catalyst onto the ITO glass to prepare the working electrode. Thickness is an important factor to determine the optimal values for our photo-catalyst materials.

According to this result, the optimal layer thickness was chosen 25 which has been obtained the highest photo-current response under the visible light illumination.

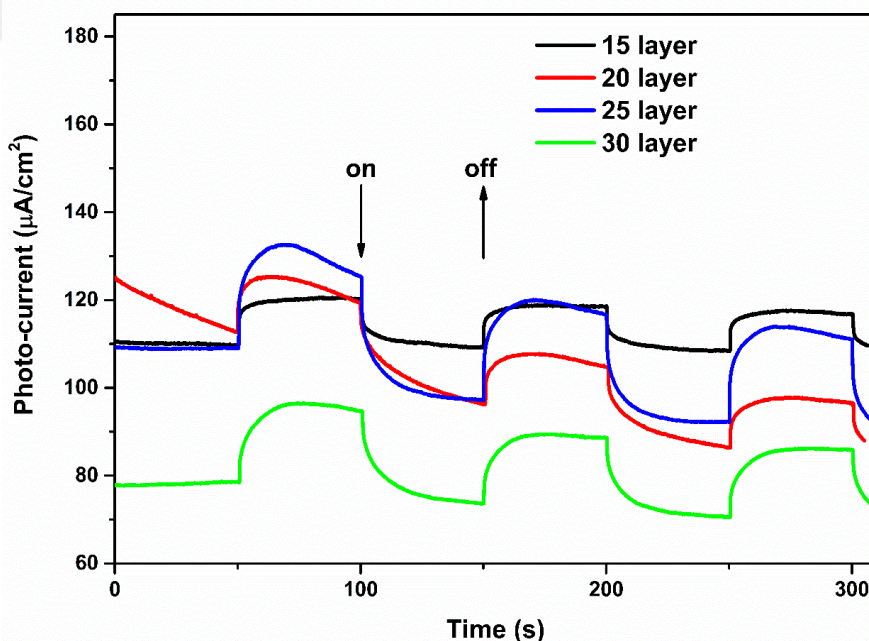


Figure3.15: Chronoamperometry analysis of the $\text{ITO}/\text{Fe}_3\text{O}_4@\text{TiO}_2$ photo-catalyst at 15, 25, 30 layer thickness. Used electrolyte 0.1M Na_2S at 0V vs. RHE

- **Optimization of the Annealing Temperature**

According to the literature, annealing temperature and annealing atmosphere is an essential feature that control the electrical, optical and structural properties of ITO thin films [71, 72]. Annealing temperature is an important criteria to obtain the optimal photo-current response in photo-electrochemical applications. In order to optimize the annealing temperature as-prepared photo-catalyst material was coated onto ITO glass at 25 layer

thickness and annealed at 300°C, 450°C and 550°C. Photo-current response of the electrodes at different temperatures was shown in Figure 3.14. According to Chronoamperometry measurement, as the annealing temperature has increased the photo-current density. The highest photo-current response was obtained at 550°C. Obtained photo-current response at 300°C, 450°C and 550°C temperature are 8, 9 and 16.2 $\mu\text{A}/\text{cm}^2$ respectively.

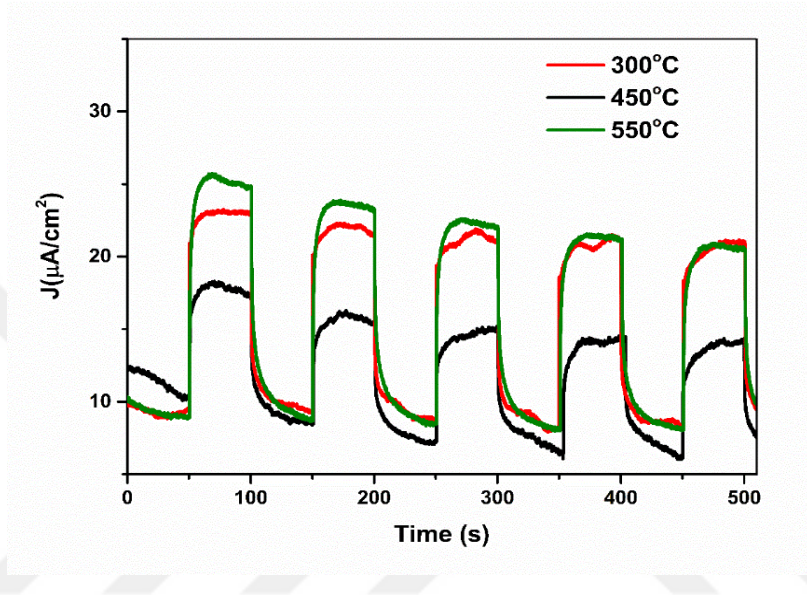


Figure 3.16: Effect of annealing temperature on the ITO/Fe₃O₄@TiO₂ photo-catalyst

3.5.1 Linear Sweep Voltammetry Results

Prepared photo-catalyst was deposited onto ITO glass according to the results of the obtained optimization criteria. For all of the photo-catalyst linear sweep voltammetry was performed. Obtained photo-current response was shown in figure 3.15. According to linear sweep voltammetry results synthesized photocatalyst are active in the visible light spectrum. When the light turned on, under the visible light illumination the Fe₃O₄@TiO₂ and Fe₃O₄@TiO₂-Ni²⁺ photocatalyst gives 20 and 13 $\mu\text{A}/\text{cm}^2$, respectively. This photo-current response is higher than the obtained data in similar studies [42, 73]. Metal ion loading have been comprehensively examined for expanding the photocatalytic and photo-electro-catalytic activities of TiO₂ based photocatalyst. In the studies performed, it was seen that the ion loading to the photocatalyst suppressed the electron-hole recombination and increase the photo-response in the visible region [3]. In the light of this information we have load our Fe₃O₄@TiO₂ photocatalyst and NiFe₂O₄@TiO₂ with

Ni²⁺ ion. This loading has been concluded that the photo-current response has decreased which should be due to the low band gap. Linear sweep voltammetry analysis results of the all prepared photocatalysts were shown in Figure 3.17 for vapor thermal method.

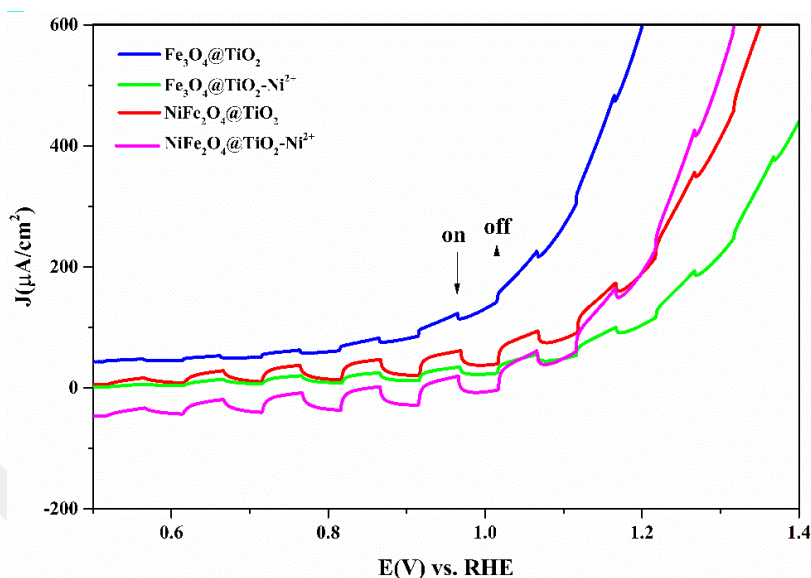


Figure 3.17: Linear Sweep Voltammetry Analysis under the visible light illumination. Electrolyte 0.1M Na₂S for vapor thermal method photocatalyst

LSV analysis was performed under the visible light. The same material synthesized with a simple non-thermal method and analyzed under the same conditions. Obtained results were shown in Figure 3.18. The results are harmonious with the chronoamperometry results.

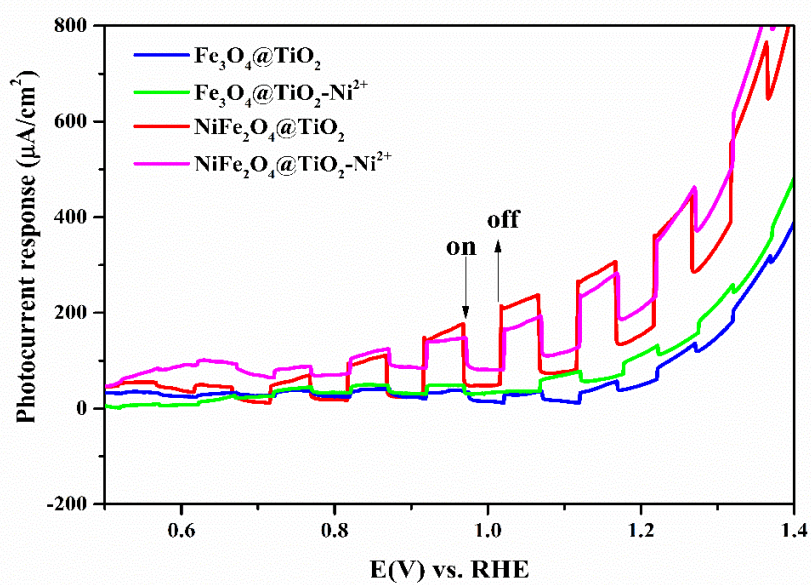


Figure 3.18: Linear Sweep Voltammetry Analysis of the $\text{Fe}_3\text{O}_4@\text{TiO}_2$, $\text{Fe}_3\text{O}_4@\text{TiO}_2\text{-Ni}^{2+}$, $\text{NiFe}_2\text{O}_4@\text{TiO}_2$ and $\text{NiFe}_2\text{O}_4@\text{TiO}_2\text{-Ni}^{2+}$ samples prepared by non-thermal method under the visible light illumination and light on-off conditions. (Electrolyte 0.1M Na_2S)

3.5.2 Chronoamperometry Analysis Results

Chronoamperometry examination was applied with the aim of scrutinize the photo-catalyst steadiness of the over time. Photo-current response of the all prepared photo-catalyst was shown in Figure 3.19. Chronoamperometry analysis was performed at 0V applied potential for all photo-catalysts. The obtained photo-current responses of the synthesized photo-catalysts are shown in Table 3.3. According to this result the highest photo-current was obtained from the $\text{NiFe}_2\text{O}_4@\text{TiO}_2\text{-Ni}^{2+}$ photo-catalyst. $\text{Fe}_3\text{O}_4@\text{TiO}_2$, $\text{Fe}_3\text{O}_4@\text{TiO}_2\text{-Ni}^{2+}$ gave almost same current value.

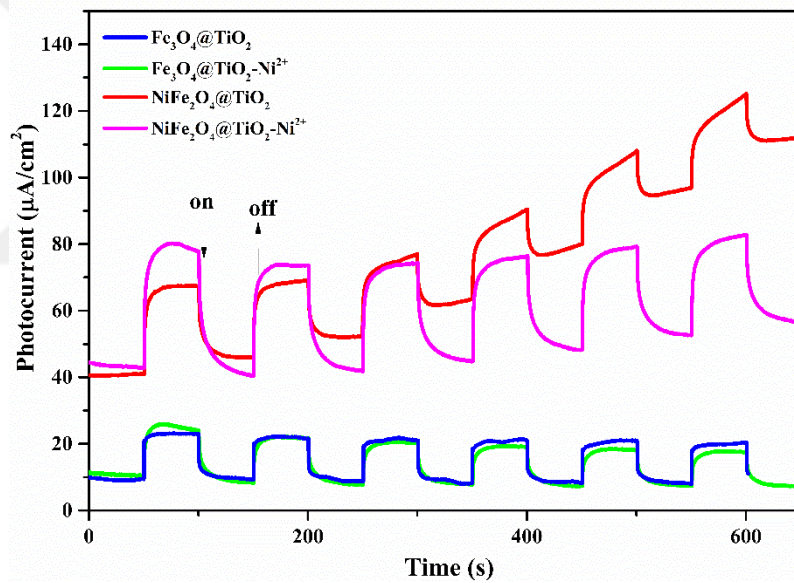


Figure3.19: Photo-current response of the $\text{Fe}_3\text{O}_4@\text{TiO}_2$, $\text{Fe}_3\text{O}_4@\text{TiO}_2\text{-Ni}^{2+}$, $\text{NiFe}_2\text{O}_4@\text{TiO}_2$ and $\text{NiFe}_2\text{O}_4@\text{TiO}_2\text{-Ni}^{2+}$ by vapor thermal method

The photo-current response of the $\text{NiFe}_2\text{O}_4@\text{TiO}_2$ and load with Ni^{2+} cations are higher than the $\text{Fe}_3\text{O}_4@\text{TiO}_2$ photo-catalyst synthesized by vapor thermal photocatalyst. Besides, we used a different synthesis method to increase the photo-current response of the prepared samples. Obtained results were depicted in Figure 3.20. Photo-current response of the $\text{NiFe}_2\text{O}_4@\text{TiO}_2$ sample showed higher photo-current response.

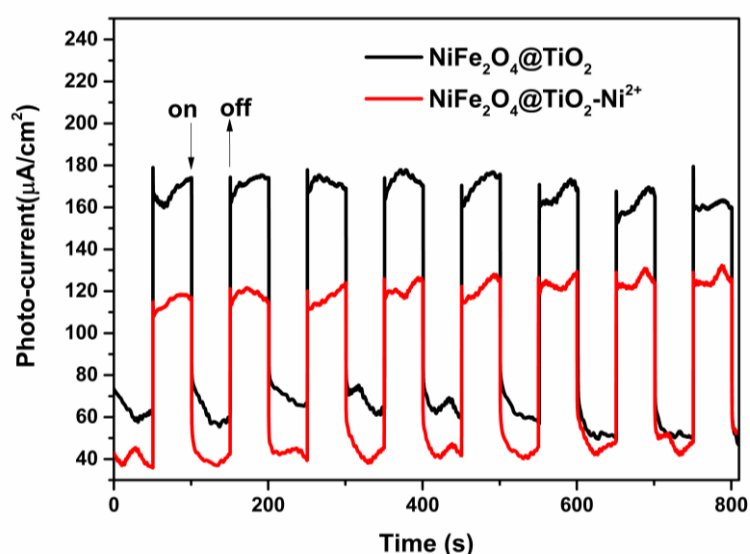


Figure 3.20: Photo-current response of the $\text{NiFe}_2\text{O}_4@\text{TiO}_2$ and $\text{NiFe}_2\text{O}_4@\text{TiO}_2\text{-Ni}^{2+}$ by non-thermal method

Table 3.3: Photo-current response results of the synthesized photo-catalysts

Vapor Thermal Method	Photo-current Response ($\mu\text{A}/\text{cm}^2$)	Non-thermal Method	Photo-current Response ($\mu\text{A}/\text{cm}^2$)
$\text{Fe}_3\text{O}_4@\text{TiO}_2$	13	$\text{Fe}_3\text{O}_4@\text{TiO}_2$	24
$\text{Fe}_3\text{O}_4@\text{TiO}_2\text{-Ni}^{2+}$	15	$\text{Fe}_3\text{O}_4@\text{TiO}_2\text{-Ni}^{2+}$	11
$\text{NiFe}_2\text{O}_4@\text{TiO}_2$	21	$\text{NiFe}_2\text{O}_4@\text{TiO}_2$	132
$\text{NiFe}_2\text{O}_4@\text{TiO}_2\text{-Ni}^{2+}$	37	$\text{NiFe}_2\text{O}_4@\text{TiO}_2\text{-Ni}^{2+}$	75

3.5.3 Mott-Schottky Analysis Results

Mott-Schottky analysis was performed in dark conditions. Donor densities of the photo-catalysts were calculated and shown in Table 3.4. The slope drawn on the linear region gave the flat band potential of the photo-catalyst. Beside this, the sign of the slope showed the characteristic semiconductor type of the photo-catalyst[44, 74].

Mott Schottky analysis was performed for the TiO_2 semiconductor material. TiO_2 has a pH dependence nature on the potential of flat band which generally shifts by the $0.059 \cdot \text{pH}$ [75]. According to obtained result, the E_{fb} of the TiO_2 was found -0.97V . The donor density was accurately considered from the Mott Schottky relation that is equal to

3.58×10^{18} . Obtained slope has a negative sign which proves the n-type characteristic of the TiO_2 .

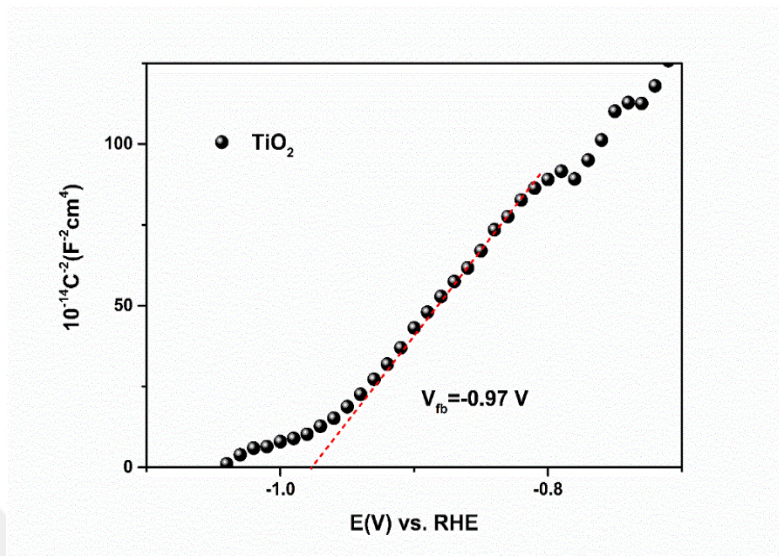


Figure 3.21: Mott-Schottky plot of the TiO_2

Mott-Schottky analysis was performed by Gamry potentiostat instrument and in the dark conditions. This experiment is an important tool to understand the characteristics of the analyzed material. According to analysis result, the sign of the slope is positive which proved that $\text{Fe}_3\text{O}_4@\text{TiO}_2$ is an n-type material. The n-type character can be attributed to the prepared core@shell sample which magnetic Fe_3O_4 core is coated with n-type TiO_2 successfully. The curve depicted in Figure 3.22 has a linear behavior where intercepts at x axis that is E_{fb} of the $\text{Fe}_3\text{O}_4@\text{TiO}_2$ sample. Besides, the donor density can be measured from the Mott Schottky relation explained in Section 2.2.9.3. The calculated donor density for $\text{Fe}_3\text{O}_4@\text{TiO}_2$ is that $2.0 \times 10^{18} \text{ cm}^{-3}$.

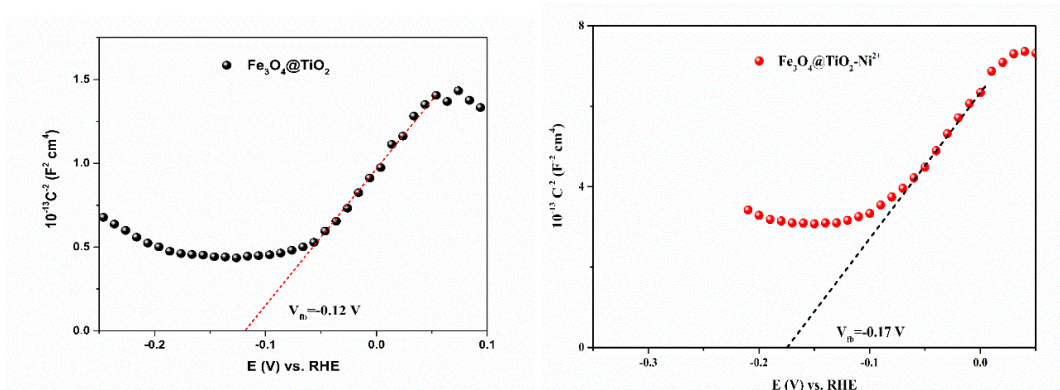


Figure 3.22: Mott-Schottky plot of the $\text{Fe}_3\text{O}_4@\text{TiO}_2$ and $\text{Fe}_3\text{O}_4@\text{TiO}_2\text{-Ni}^{2+}$ in the dark condition

Mott-Schottky analysis was performed for NiFe_2O_4 , $\text{NiFe}_2\text{O}_4@\text{TiO}_2$, $\text{NiFe}_2\text{O}_4@\text{TiO}_2\text{-Ni}^{2+}$ samples. NiFe_2O_4 is a p-type semiconductor material which has magnetic characteristic and this had been proved by Mott-Schottky analysis.

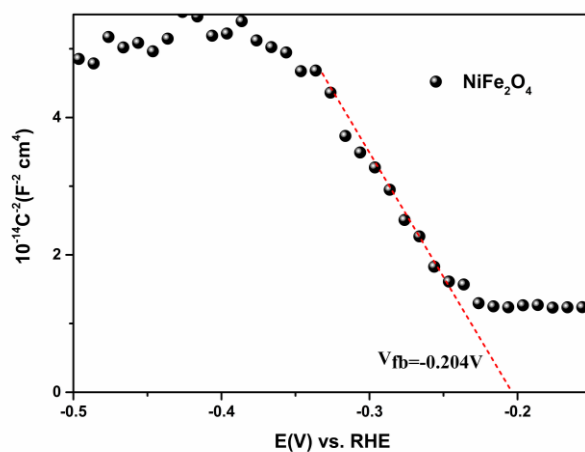


Figure 3. 23: Mott Schottky plot of the NiFe_2O_4

Table 3.4: Mott-Schottky Analysis Results of the samples

Synthesized Photocatalyst	Photo-current Response($\mu\text{A}/\text{cm}^2$)	Flat Band Potential (V)	Donor Density(cm^{-3})
$\text{Fe}_3\text{O}_4@\text{TiO}_2$	13	-0.12	$2.00\text{E}+18$
$\text{Fe}_3\text{O}_4@\text{TiO}_2\text{-Ni}^{2+}$	15	-0.17	$2.07\text{E}+18$
TiO_2	-	-0.97	$3.58\text{E}+18$
NiFe_2O_4	-	-0.20	$1.94\text{E}+18$
$\text{NiFe}_2\text{O}_4@\text{TiO}_2$	21	-0.21	$1.34\text{E}+18$
$\text{NiFe}_2\text{O}_4@\text{TiO}_2\text{-Ni}^{2+}$	37	-0.26	$1.30\text{E}+18$

3.6 Photo-catalytic Methylene Blue Degradation Results

- **Optimization of the Photocatalyst Amount**

The amount of the photocatalyst is a vital effect on photocatalytic decolorization experiments. Before the start the experiments we had optimized the photocatalyst amount. It is found that the degradation efficiency had increased till the photocatalyst amount reached the optimal value 0.5 g in 100 ml methylene blue solution. It is showed in the Figure 3.24 that the degradation efficiency result by comparing the different amount of photocatalyst

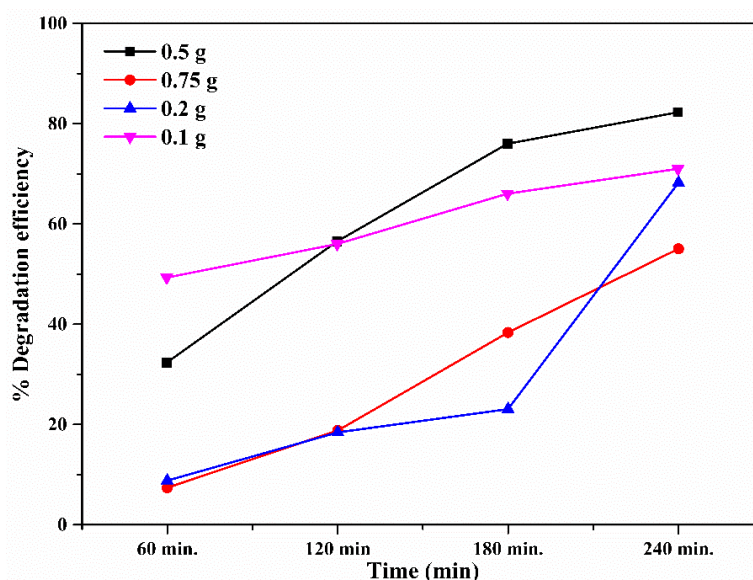


Figure 3.24: The optimization of the photocatalyst amount under simulated light irradiation

- **Photo-catalytic Methylene Blue Degradation Results Prepared By The Vapor Thermal Method**

Photo-catalytic methylene blue degradation analysis was performed by analyzing the absorbance values of the liquid samples which contains photo-catalyst and methylene blue solution at different time interval. To obtain the concentration values of the samples from the absorbance value (via the UV-visible spectroscopy) we used the calibration curve as shown in Figure 3.25.

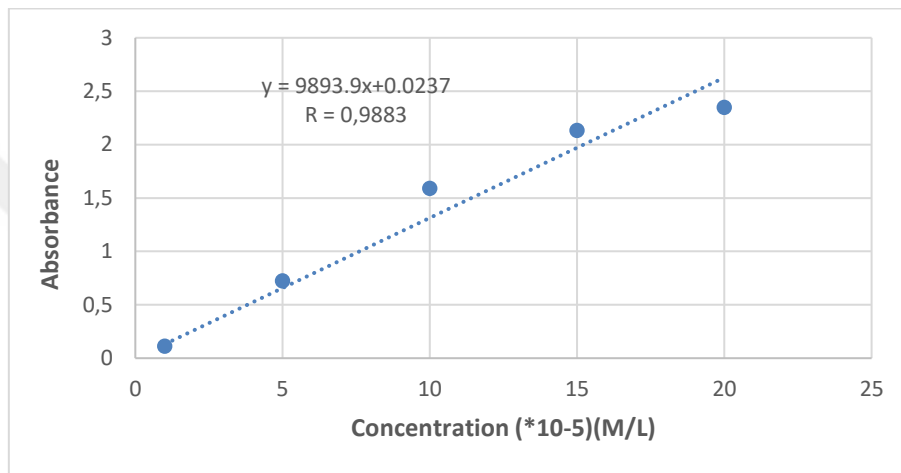


Figure 3.25: Calibration Curve

Calibration curve was obtained by using methylene blue solution having different concentration values. Methylene blue concentration decreases when the absorbance value has decreased. Methylene blue degradation process in the existence of photo-catalyst was performed under the simulated visible light. At different time interval the absorbance value was depicted in Figure 3.26. Degradation rates were calculated using the equation 2.6 described in chapter 2. It was depicted that obtained degradation efficiencies in Table 3.5 for the vapor thermal method photocatalysts.

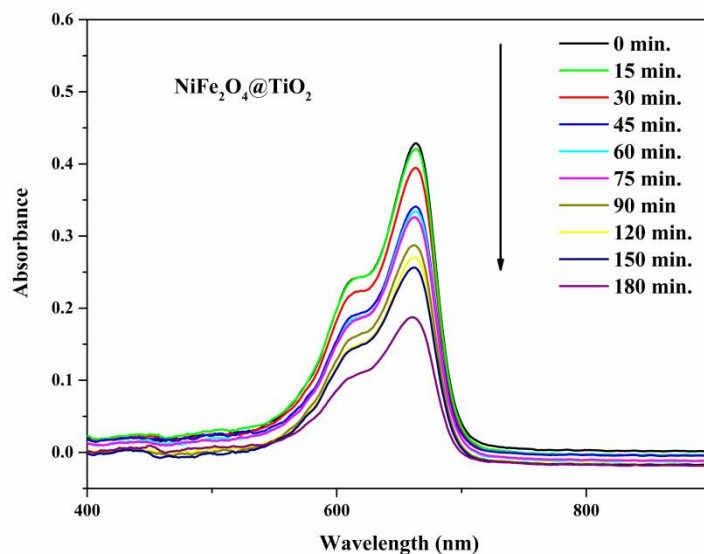


Figure 3.26: Absorbance spectra of the methylene blue solution photo-decolorization process over time in the existence of NiFe₂O₄@TiO₂ photocatalyst and degradation efficiency vs. time

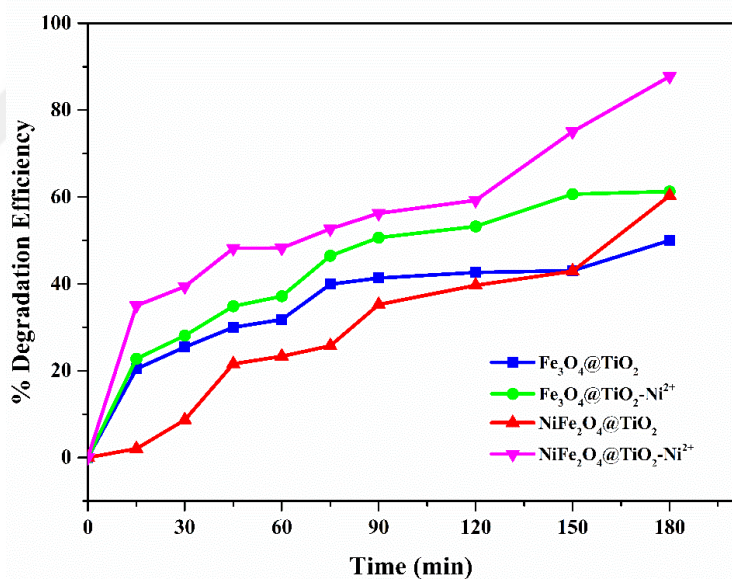


Figure 3.27: Degradation efficiency of the photocatalysts Fe₃O₄@TiO₂, Fe₃O₄@TiO₂-Ni²⁺, NiFe₂O₄@TiO₂, NiFe₂O₄@TiO₂-Ni²⁺ under the simulated visible light irradiation

Table 3.5: Degradation Efficiency of the Prepared Photocatalysts by Vapor Thermal Method

Synthesized Photocatalyst	Degradation Efficiency	Reaction Rate Constant ($k \times 10^{-3}$)	Correlation Coefficient (R^2)
$\text{Fe}_3\text{O}_4@\text{TiO}_2$	%50.3	4.0	0.9789
$\text{Fe}_3\text{O}_4@\text{TiO}_2\text{-Ni}^{2+}$	%61.2	5.0	0.9801
$\text{NiFe}_2\text{O}_4@\text{TiO}_2$	%60.3	4.0	0.9539
$\text{NiFe}_2\text{O}_4@\text{TiO}_2\text{-Ni}^{2+}$	%87.7	9.0	0.9855

- **Repetitive Use of Photocatalyst**

It is clear that to examine the repeatability of the photocatalyst, the recycle experiments were performed. At the end of the degradation, the photocatalysts were washed, dried to carry out a new degradation process. This analysis was made using the same photocatalyst sample for five times. The highest degradation rate photocatalyst $\text{NiFe}_2\text{O}_4@\text{TiO}_2\text{-Ni}^{2+}$ was used to investigate the durability and repeatability ratio of the samples. It is clear in Figure 3.28 that the degradation rates decreased when the recycle number increased over time.

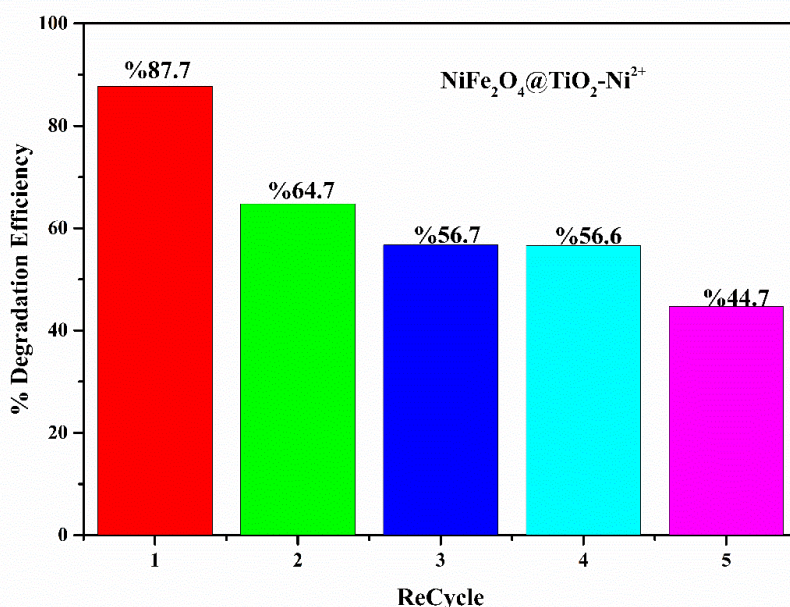


Figure3.28: The Results of the Recycling Studies for the $\text{NiFe}_2\text{O}_4@\text{TiO}_2\text{-Ni}^{2+}$ photocatalyst synthesized by vapor thermal method

- **Photo-catalytic Methylene Blue Degradation Results Prepared by Non-Thermal Method**

In this section, we prepared our designed four photocatalysts by a simple loading method and investigated photocatalytic activities by degrading the organic dye methylene blue solution. As a result of this experiments it appeared that the photocatalytic activities of the same photocatalysts showed higher performance. Methylene blue solution converted into water in a shorter time compared to the vapor thermal method. The degradation efficiencies of the non-thermal method samples were calculated and depicted in Table 3.6.

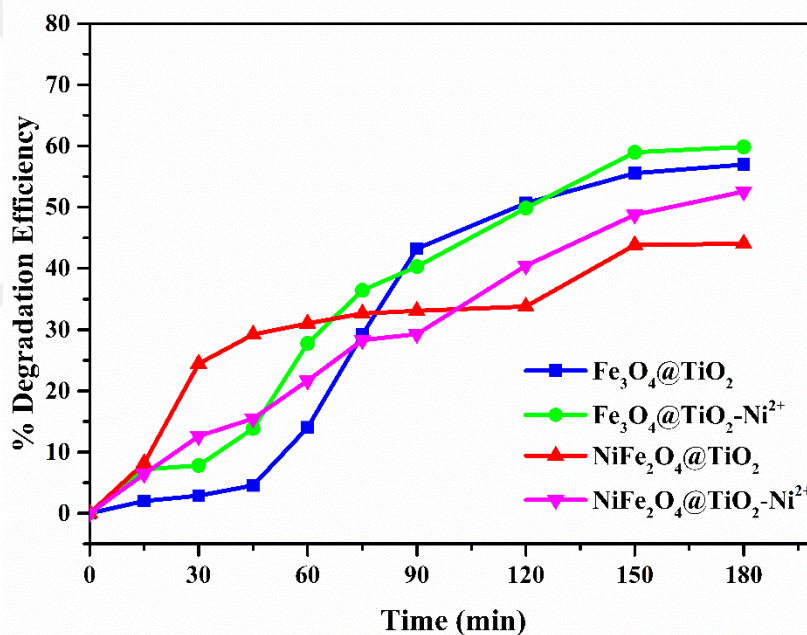


Figure3.29: Degradation efficiency of the $\text{Fe}_3\text{O}_4@\text{TiO}_2$, $\text{Fe}_3\text{O}_4@\text{TiO}_2\text{-Ni}^{2+}$, $\text{NiFe}_2\text{O}_4@\text{TiO}_2$, $\text{NiFe}_2\text{O}_4@\text{TiO}_2\text{-Ni}^{2+}$ samples prepared by non-thermal method under the simulated light irradiation

Table3.6: Degradation Efficiencies of the Prepared Photocatalysts by Non-Thermal Method

Synthesized Photocatalyst	Degradation Efficiency	Reaction Rate Constant ($k \times 10^{-3}$)	Correlation Coefficient (R^2)
$\text{Fe}_3\text{O}_4@ \text{TiO}_2$	%56.97	5.7	0.9974
$\text{Fe}_3\text{O}_4@ \text{TiO}_2\text{-Ni}^{2+}$	%59.83	5.7	0.9884
$\text{NiFe}_2\text{O}_4@ \text{TiO}_2$	%44.03	2.9	0.9382
$\text{NiFe}_2\text{O}_4@ \text{TiO}_2\text{-Ni}^{2+}$	%52.58	4.3	0.9938

4 CONCLUSION

Our main objective is that magnetic photocatalysts synthesis and characterization for efficient hydrogen generation. In this study, magnetic core $\text{Fe}_3\text{O}_4/\text{NiFe}_2\text{O}_4@ \text{TiO}_2$ shell photocatalyst were produced with two different synthesis methods. First, planned materials were produced with a vapor thermal method. The photocatalytic and photoelectrocatalytic efficiency of the samples were investigated. The photocatalytic activity was characterized by MB degradation reaction. Besides, the photoelectrochemical activity of the photocatalysts was analyzed by LSV, CA and Mott-Schottky analysis. The PEC analysis was performed to measure the H_2 production efficiencies of the samples. The same activity experiments were performed for the photocatalysts prepared by loading method.

XRD characterization was performed for the $\text{Fe}_3\text{O}_4@ \text{TiO}_2$ samples. According to the obtained XRD pattern, synthesized $\text{Fe}_3\text{O}_4@ \text{TiO}_2$ showed both TiO_2 phase and Fe_3O_4 phase characteristic peaks. The main peaks of the Fe_3O_4 were lesser and broader than the peaks of the TiO_2 in the $\text{Fe}_3\text{O}_4@ \text{TiO}_2$ XRD pattern. It can be recognized that the smaller and broader peaks shows the reducing of the crystallite size of the sample [76]. When the peaks of pure TiO_2 and $\text{Fe}_3\text{O}_4@ \text{TiO}_2$ are compared, the peaks of $\text{Fe}_3\text{O}_4@ \text{TiO}_2$ sample belongs to TiO_2 phase are sharper than the pure TiO_2 . This result can be associated with the calcination step of the $\text{Fe}_3\text{O}_4@ \text{TiO}_2$ sample applied in the synthesis process which causes the enhancement in crystallinity. Same situation was obtained for the $\text{NiFe}_2\text{O}_4@ \text{TiO}_2$ XRD pattern. Broadening of the peak (101) is associated the crystallite size of the TiO_2 anatase phase. However, the peaks which obtained at 2θ degree of 55.18° and 62.96° can be attached as (211) and (002) planes of rutile phase, relatively[77]. Moreover, we can say that Fe_3O_4 controls the formation of TiO_2 phase from anatase to rutile. This can be attributed that annealing temperature can affect the phase formation of the TiO_2 . Azeez etc. al claimed in their study that when the calcination temperature was enhanced to 500°C , the triple phase mixture was obtained (which were anatase, rutile and brookite)[78]. The crystallite size was obtained using the full width at half maximum (FWHM) of the (101) peak for both $\text{Fe}_3\text{O}_4@ \text{TiO}_2$ and $\text{NiFe}_2\text{O}_4@ \text{TiO}_2$. This can be associated with the heat treatment applied at beginning of the synthesis process of the $\text{NiFe}_2\text{O}_4@ \text{TiO}_2$ sample.

UV-DRS analysis results were used to obtain the band gap values of the prepared photocatalysts for both vapor thermal and non-thermal method. Using Tauc plots, we estimated the band gap energy level of the samples. With TiO₂ coating the band gap value of the Fe₃O₄ and NiFe₂O₄ magnetic cores was increased. Generally, the higher wavelength is related the smaller band gap. Our main objective is to synthesize smaller band gap photocatalysts which is active in the visible region [40]. Photocatalysts which have obtained by vapor thermal and non-thermal method shows visible light active characteristics according to UV-DRS spectra. Ni²⁺ loading had decreased the band gap values of the photocatalysts.

SEM analysis was applied to elaborate the size and morphology of the Fe₃O₄@TiO₂ and NiFe₂O₄@TiO₂. Obtained results showed that the particles synthesized by vapor thermal method were spherical shape with a diameter of 50 nm. Ni²⁺ ion loading could not have made any difference from the Fe₃O₄@TiO₂ nanocomposite. Moreover, NiFe₂O₄@TiO₂ photocatalyst have the diameter of 62.5 nm which is higher than the Fe₃O₄@TiO₂ material and it has spherical shape.

EDS analysis was accomplished to observe the atomic compositions of the Fe₃O₄@TiO₂-Ni²⁺ photocatalyst. The obtained result proved that Ni²⁺ loading could be managed successfully. Hence, the loading ratio of the Ni²⁺ is too low, the quantitative compounds could be identified properly.

Raman analysis was measured to examine the vibrational and morphological characteristics of the samples both of the vapor thermal and non-thermal method. The obtained results showed that our samples were entirely coated with TiO₂ semiconductor. All the peaks have showed the characteristic TiO₂ peaks. Moreover, loading with a transition metal changed the peak positions through the left because of the molecular weight of the Ni²⁺ cations higher than the Ti⁴⁺ ion.

Photoelectrochemical activity experiments were accomplished to examine the H₂ production activity using the linear sweep voltammetry and chronoamperometry analysis. When we investigate the PEC activity results, the materials synthesized by vapor thermal method showed lower activity than the loading method samples. Loading with Ni²⁺ ion of the samples also increased the PEC activity of the samples synthesized by vapor thermal method. Loading with Ni²⁺ ion decreased the band gap value of the photocatalyst.

Therefore, the photocatalytic efficiency of the sample increased because of the reduction of band gap energy which boosts the absorption capacity in the visible light spectrum. And also, the suppression effect of the Ni²⁺ metal can drop the recombination reaction between the electron and hole. Moreover, the donor densities of the samples were obtained from Mott-Schottky analysis increased by Ni²⁺ loading and this enhanced the photo-current response of the samples. The highest photocurrent response was obtained from the NiFe₂O₄@TiO₂-Ni²⁺ photocatalyst synthesized by vapor thermal method. It is believed that if the active regions which provide the transfer of the electrons are closed, this results in the reduction of the photocurrent response[24]. Moreover, the higher photocurrent response indicates the effective electron-hole separation efficiency as the current increases [79]. The photo-currents obtained by the non-thermal method differed from the loading method. The highest photo-current results obtained from the NiFe₂O₄@TiO₂ which was 6.3 times higher than the vapor method photocatalyst material. Different synthesis method affects the results. Moreover, in non-thermal method did not apply any heat treatment to the photocatalysts[72]. However, the Ni²⁺ ion decreased the photocurrent response. This result can be associated with the transfer of the electron and hole had decreased with the closure of the active regions in photocatalyst surface.

Photocatalytic methylene blue degradation experiments were performed under the simulated solar light illumination. Firstly, the amount of the photocatalyst was optimized and 0.5 g was calculated as the optimal value for the photocatalytic degradation experiments. Synthesized photocatalysts were compared for vapor thermal and non-thermal method samples. Experiments showed that the degradation efficiencies of the samples have different result. Vapor thermal method photocatalysts convert the methylene blue dye almost 87% to the water especially the NiFe₂O₄@TiO₂-Ni²⁺ material. However, non-thermal method photocatalyst exhibited lesser degradation efficiency. The photocatalyst surface area is an effective way to increase the degradation efficiency because a higher surface area offers better physicochemical properties and this features also own the better quantum and degradation efficiency[80]. Moreover, it can be considered that the diameter of the NiFe₂O₄@TiO₂ is bigger than the Fe₃O₄@TiO₂ photocatalyst. It can be associated to the enhancement. Obtained results have showed that the photocatalytic activities of the vapor thermal method photocatalysts are of higher efficiency compared to the non-thermal method photocatalyst. The non-thermal method

samples converted the methylene blue dye approximately 50% for 4 different materials. Ni²⁺ ion loading had enhanced the degradation efficiency. The highest degradation rate could be obtained from the Fe₃O₄@TiO₂-Ni²⁺ photocatalyst which is the degradation efficiency equal to 59.93% (as can be seen from Figure 3.28). NiFe₂O₄@TiO₂ modified photocatalyst revealed low photocatalytic activity and converted the methylene blue dye to the water lesser than 50%.

According to the obtained results, the photocatalyst modified with magnetic Fe₃O₄ showed low photocatalytic activity. This is mainly linked with that the CB of the Fe₃O₄ magnetic core is lower than the TiO₂ shell structure and through the photo excitation reaction generated e⁻/h⁺ pairs can come together again in magnetic core resulting the decrease in photocatalytic activity[81].

Table 4.1 shows similar study results found in the literature using the same materials to compare our results for the photoelectrochemical splitting of water molecule reactions for hydrogen generation. Moreover, Table 4.2 shows the similar dye degradation experiments results comparing with the literature works which used the same photocatalyst materials.

Table 4. 1: Literature Review of the Prepared Photocatalyst for PEC experiments

Photoelectrocatalyst	Method	Sacrificial reagents	Light source	Band gap	Current Density	Ref.
$\text{Fe}_3\text{O}_4/\text{TiO}_2/\text{Ag}_2\text{Si}_2\text{O}_7$	Solvothermal	3wt% NaCl	AM 1.5 Illumination 40 mW cm ⁻²	1.58 eV	9.4 mA/cm ²	[73]
$\text{g-C}_3\text{N}_4/\text{Fe}_3\text{O}_4/\text{TiO}_2$	Sol-gel	0.2 M Na ₂ SO ₄	>400 nm, cutoff filter, 500 W Xe arc Lamp		20mA	[42]
$\text{NiFe}_2\text{O}_4/\text{TiO}_2$	Hydrothermal method	0.5 M Na ₂ SO ₄	AM 1.5 Illumination 40 mW cm ⁻²	1.84 eV	4.13mA/cm ²	[40]
$\text{NiFe}_2\text{O}_4/\text{GO}$	Co-precipitation	0.5 M Na ₂ SO ₄	450 W Xe Lamp		0.2mA/cm ²	[82]
Magnetic3D@TiO₂	Solvothermal	0.1 M Na ₂ SO ₄	8W Mercury Lamb		≈ 0.2μA	[83]
$\text{Fe}_3\text{O}_4/\text{SiO}_2/\text{BiOBr}$	Sol-gel	0.1 M Na ₂ SO ₄	300 W Xe Lamp	2.70 eV	≈ 3μA	[79]
a) $\text{Fe}_3\text{O}_4/\text{TiO}_2$ b) $\text{Fe}_3\text{O}_4/\text{TiO}_2\text{-Ni}^{2+}$ c) $\text{NiFe}_2\text{O}_4/\text{TiO}_2$ d) $\text{NiFe}_2\text{O}_4/\text{TiO}_2\text{-Ni}^{2+}$	Vapor Thermal and Non-thermal	0.1M Na ₂ S	300W Xe Lamp-(>400 nm, cutoff filter)	a)1.96eV b)1.80eV c)2.0eV d)1.76eV	VT - NT a)13 - 24 mA/cm ² b)15 - 11mA/cm ² c)21 - 132mA/cm ² d)37 - 75mA/cm ²	This Work

Table 4.2: Literature Review of the Prepared Photocatalyst for MB degradation experiments

Photocatalyst	Method	Target Component	Light source	Working Conditions	Performance	Ref.
$\text{Fe}_3\text{O}_4/\text{TiO}_2$	Co-precipitation	RhB	300W Hg Lamp-UV illumination	RhB=28.7ppm Catalyst solution=0.455g/L	98.3% degradation Illumination time=75min	[84]
$\text{Fe}_3\text{O}_4/\text{TiO}_2$	Heteroagglomeration	MB	UV-Sun light illumination	MB=3.20ppm Catalyst solution=0.8g/L	92%(UV);89%-(Sun) Illumination time=360min	[85]
$\text{g-C}_3\text{N}_4/\text{Fe}_3\text{O}_4/\text{TiO}_2$	Sol-gel	MB and DNBP	500W Xe Lamp-Visible light	MB=10ppm Catalyst solution=30mg	100% Illumination time=120min	[42]
$\text{Fe}_3\text{O}_4/\text{TiO}_2$	Co-precipitation	MB	Sun Light	MB=1.05g/L Catalyst solution=0.5g/L	93% Illumination time=60 min	[62]
$\text{Fe}_3\text{O}_4/\text{TiO}_2$	Solvothermal	RhB	250W Hg Lamp-UV illumination	RhB=10-5M Catalyst solution=0.82g/L	~80% Illumination time=120 min	[39]
$\text{NiFe}_2\text{O}_4/\text{TiO}_2$	Reverse micelle method	MO	UV Light	MO=8ppm Catalyst solution=0.8g/L	84% Illumination time=420 min	[86]
$\text{Fe}_3\text{O}_4/\text{SiO}_2/\text{TiO}_2$	Solvothermal	MB	UV Light	MB=10ppm Catalyst solution=1g/L	100% Illumination time=50 min	[87]
$\text{NiFe}_2\text{O}_4/\text{TiO}_2/\text{W}^{4+}$	Reverse micelle method and hydrolysis reaction	MO	UV Light	MO=8ppm Catalyst solution=0.8g/L	80% Illumination time=60 min	[88]
$\text{ZnFe}_2\text{O}_4/\text{TiO}_2$	Sol-gel	MO	Visible Light	MO=10 ppm Catalyst solution=5g/L	93% Illumination time=180 min.	[89]
$\text{Fe}_3\text{O}_4/\text{TiO}_2\text{-Ni}^{2+}$	Vapor Thermal and Non-thermal	MB	300W Xenon Lamb-Visible Light	MB=10 ppm Catalyst solution=0.5g/L	VT=50%-NT=59% Illumination time=180 min	This Work
$\text{NiFe}_2\text{O}_4/\text{TiO}_2\text{-Ni}^{2+}$	Vapor Thermal and Non-thermal	MB	300W Xe Lamb->400 nm	MB=10 ppm Catalyst solution=0.5g/L	VT=87%-NT=57% Illumination =180 min	This Work

REFERENCES

- [1] Herrmann J-M. Heterogeneous photocatalysis: fundamentals and applications to the removal of various types of aqueous pollutants. *Catalysis today*. 1999;53:115-29.
- [2] Acar C, Dincer I, Zamfirescu C. A review on selected heterogeneous photocatalysts for hydrogen production. *International Journal of Energy Research*. 2014;38:1903-20.
- [3] Ni M, Leung MK, Leung DY, Sumathy K. A review and recent developments in photocatalytic water-splitting using TiO₂ for hydrogen production. *Renewable and Sustainable Energy Reviews*. 2007;11:401-25.
- [4] Alfano O, Bahnemann D, Cassano A, Dillert R, Goslich R. Photocatalysis in water environments using artificial and solar light. *Catalysis today*. 2000;58:199-230.
- [5] Bahnemann D. Photocatalytic water treatment: solar energy applications. *Solar energy*. 2004;77:445-59.
- [6] Fujishima A, Rao TN, Tryk DA. Titanium dioxide photocatalysis. *Journal of photochemistry and photobiology C: Photochemistry reviews*. 2000;1:1-21.
- [7] Ibhadon A, Fitzpatrick P. Heterogeneous photocatalysis: recent advances and applications. *Catalysts*. 2013;3:189-218.
- [8] Yasmina M, Mourad K, Mohammed SH, Khaoula C. Treatment heterogeneous photocatalysis; Factors influencing the photocatalytic degradation by TiO₂. *Energy Procedia*. 2014;50:559-66.
- [9] Fujishima A, Zhang X, Tryk DA. Heterogeneous photocatalysis: from water photolysis to applications in environmental cleanup. *International journal of hydrogen energy*. 2007;32:2664-72.
- [10] Photocatalysis H. *From Fundamentals to Green Applications*. Springer, Berlin; 2016.
- [11] Kudo A, Miseki Y. Heterogeneous photocatalyst materials for water splitting. *Chemical Society Reviews*. 2009;38:253-78.
- [12] Dincer I. Green methods for hydrogen production. *International journal of hydrogen energy*. 2012;37:1954-71.
- [13] Singh R, Dutta S. A review on H₂ production through photocatalytic reactions using TiO₂/TiO₂-assisted catalysts. *Fuel*. 2018;220:607-20.
- [14] Liao C-H, Huang C-W, Wu J. Hydrogen production from semiconductor-based photocatalysis via water splitting. *Catalysts*. 2012;2:490-516.
- [15] Nikolaidis P, Poullikkas A. A comparative overview of hydrogen production processes. *Renewable and sustainable energy reviews*. 2017;67:597-611.
- [16] Acar C, Dincer I. Comparative assessment of hydrogen production methods from renewable and non-renewable sources. *International journal of hydrogen energy*. 2014;39:1-12.
- [17] Barka N, Qourzal S, Assabbane A, Nounah A, Ait-Ichou Y. Factors influencing the photocatalytic degradation of Rhodamine B by TiO₂-coated non-woven paper. *Journal of Photochemistry and Photobiology A: Chemistry*. 2008;195:346-51.
- [18] Ismail AA, Bahnemann DW. Photochemical splitting of water for hydrogen production by photocatalysis: a review. *Solar Energy Materials and Solar Cells*. 2014;128:85-101.
- [19] Navarro R, Del Valle F, De La Mano JV, Álvarez-Galván M, Fierro J. Photocatalytic water splitting under visible light: Concept and catalysts development. *Advances in Chemical Engineering*. 2009;36:111-43.
- [20] Shi Z, Wen X, Guan Z, Cao D, Luo W, Zou Z. Recent progress in photoelectrochemical water splitting for solar hydrogen production. *Annals of Physics*. 2015;358:236-47.
- [21] Joy J, Mathew J, George SC. Nanomaterials for photoelectrochemical water splitting—review. *International Journal of Hydrogen Energy*. 2018;43:4804-17.
- [22] Chen Z, Dinh HN, Miller E. *Photoelectrochemical water splitting*: Springer; 2013.

- [23] Lianos P. Production of electricity and hydrogen by photocatalytic degradation of organic wastes in a photoelectrochemical cell: the concept of the photofuelcell: a review of a re-emerging research field. *Journal of Hazardous Materials*. 2011;185:575-90.
- [24] Kuyumcu ÖK, Boz İ. Synergistic effect of PtO and M²⁺ (Cu²⁺, Ni²⁺, Co²⁺) on photo (electro) catalytic activity of TiO₂ nanorod array thin films. *Journal of Photochemistry and Photobiology A: Chemistry*. 2015;301:32-9.
- [25] Li R, Li C. Photocatalytic water splitting on semiconductor-based photocatalysts. *Advances in Catalysis: Elsevier*; 2017. p. 1-57.
- [26] Sakthivel S, Kisch H. Daylight photocatalysis by carbon-modified titanium dioxide. *Angewandte Chemie International Edition*. 2003;42:4908-11.
- [27] Asahi R, Morikawa T, Ohwaki T, Aoki K, Taga Y. Visible-light photocatalysis in nitrogen-doped titanium oxides. *science*. 2001;293:269-71.
- [28] Liu S-H, Syu H-R. One-step fabrication of N-doped mesoporous TiO₂ nanoparticles by self-assembly for photocatalytic water splitting under visible light. *Applied energy*. 2012;100:148-54.
- [29] Ohno T, Mitsui T, Matsumura M. Photocatalytic activity of S-doped TiO₂ photocatalyst under visible light. *Chemistry letters*. 2003;32:364-5.
- [30] Bamwenda GR, Tsubota S, Nakamura T, Haruta M. Photoassisted hydrogen production from a water-ethanol solution: a comparison of activities of Au · TiO₂ and Pt · TiO₂. *Journal of Photochemistry and Photobiology A: Chemistry*. 1995;89:177-89.
- [31] Sakata Y, Matsuda Y, Yanagida T, Hirata K, Imamura H, Teramura K. Effect of metal ion addition in a Ni supported Ga₂O₃ photocatalyst on the photocatalytic overall splitting of H₂O. *Catalysis letters*. 2008;125:22-6.
- [32] Jang JS, Kim HG, Lee JS. Heterojunction semiconductors: a strategy to develop efficient photocatalytic materials for visible light water splitting. *Catalysis today*. 2012;185:270-7.
- [33] Saraswat SK, Rodene DD, Gupta RB. Recent advancements in semiconductor materials for photoelectrochemical water splitting for hydrogen production using visible light. *Renewable and Sustainable Energy Reviews*. 2018;89:228-48.
- [34] Madhumitha A, Preethi V, Kanmani S. Photocatalytic hydrogen production using TiO₂ coated iron-oxide core shell particles. *International Journal of Hydrogen Energy*. 2018;43:3946-56.
- [35] de Lacheisserie ÉDT, Gignoux D, Schlenker M. *Magnetism: fundamentals: Springer Science+ Business Media*; 2005.
- [36] Getzlaff M. *Fundamentals of magnetism: Springer Science & Business Media*; 2007.
- [37] Dom R, Subasri R, Radha K, Borse PH. Synthesis of solar active nanocrystalline ferrite, MFe₂O₄ (M: Ca, Zn, Mg) photocatalyst by microwave irradiation. *Solid State Communications*. 2011;151:470-3.
- [38] Taffa DH, Dillert R, Ulpe AC, Bauerfeind KC, Bredow T, Bahnemann DW, et al. Photoelectrochemical and theoretical investigations of spinel type ferrites (M_xFe_{3-x}O₄) for water splitting: a mini-review. *Journal of Photonics for Energy*. 2016;7:012009.
- [39] Xin T, Ma M, Zhang H, Gu J, Wang S, Liu M, et al. A facile approach for the synthesis of magnetic separable Fe₃O₄@ TiO₂, core-shell nanocomposites as highly recyclable photocatalysts. *Applied Surface Science*. 2014;288:51-9.
- [40] Kim HS, Kim D, Kwak BS, Han GB, Um M-H, Kang M. Synthesis of magnetically separable core@ shell structured NiFe₂O₄@ TiO₂ nanomaterial and its use for photocatalytic hydrogen production by methanol/water splitting. *Chemical Engineering Journal*. 2014;243:272-9.
- [41] Ma P, Jiang W, Wang F, Li F, Shen P, Chen M, et al. Synthesis and photocatalytic property of Fe₃O₄@ TiO₂ core/shell nanoparticles supported by reduced graphene oxide sheets. *Journal of Alloys and Compounds*. 2013;578:501-6.

- [42] Wei X-N, Wang H-L. Preparation of magnetic g-C₃N₄/Fe₃O₄/TiO₂ photocatalyst for visible light photocatalytic application. *Journal of Alloys and Compounds*. 2018;763:844-53.
- [43] Chi Y, Yuan Q, Li Y, Zhao L, Li N, Li X, et al. Magnetically separable Fe₃O₄@ SiO₂@ TiO₂-Ag microspheres with well-designed nanostructure and enhanced photocatalytic activity. *Journal of hazardous materials*. 2013;262:404-11.
- [44] Yusoff N, Kumar SV, Pandikumar A, Huang N, Marlinda A, An'amt M. Core-shell Fe₃O₄-ZnO nanoparticles decorated on reduced graphene oxide for enhanced photoelectrochemical water splitting. *Ceramics International*. 2015;41:5117-28.
- [45] Chang C-J, Lee Z, Chu K-W, Wei Y-H. CoFe₂O₄@ ZnS core-shell spheres as magnetically recyclable photocatalysts for hydrogen production. *Journal of the Taiwan Institute of Chemical Engineers*. 2016;66:386-93.
- [46] Rauf M, Ashraf SS. Fundamental principles and application of heterogeneous photocatalytic degradation of dyes in solution. *Chemical engineering journal*. 2009;151:10-8.
- [47] Theerthagiri J, Chandrasekaran S, Salla S, Elakkiya V, Senthil R, Nithyadharseni P, et al. Recent developments of metal oxide based heterostructures for photocatalytic applications towards environmental remediation. *Journal of Solid State Chemistry*. 2018;267:35-52.
- [48] Ajmal A, Majeed I, Malik RN, Idriss H, Nadeem MA. Principles and mechanisms of photocatalytic dye degradation on TiO₂ based photocatalysts: a comparative overview. *Rsc Advances*. 2014;4:37003-26.
- [49] Bizani E, Fytianos K, Poullos I, Tsiroidis V. Photocatalytic decolorization and degradation of dye solutions and wastewaters in the presence of titanium dioxide. *Journal of Hazardous Materials*. 2006;136:85-94.
- [50] Riga A, Soutsas K, Ntampeglitis K, Karayannis V, Papapolymerou G. Effect of system parameters and of inorganic salts on the decolorization and degradation of Procion H-exl dyes. Comparison of H₂O₂/UV, Fenton, UV/Fenton, TiO₂/UV and TiO₂/UV/H₂O₂ processes. *Desalination*. 2007;211:72-86.
- [51] Caliman AF, Cojocaru C, Antoniadis A, Poullos I. Optimized photocatalytic degradation of Alcian Blue 8 GX in the presence of TiO₂ suspensions. *Journal of Hazardous Materials*. 2007;144:265-73.
- [52] Muruganandham M, Swaminathan M. Solar photocatalytic degradation of a reactive azo dye in TiO₂-suspension. *Solar Energy Materials and Solar Cells*. 2004;81:439-57.
- [53] Macedo L, Zaia D, Moore G, de Santana H. Degradation of leather dye on TiO₂: a study of applied experimental parameters on photoelectrocatalysis. *Journal of Photochemistry and Photobiology A: Chemistry*. 2007;185:86-93.
- [54] Haarstrick A, Kut OM, Heinzle E. TiO₂-assisted degradation of environmentally relevant organic compounds in wastewater using a novel fluidized bed photoreactor. *Environmental science & technology*. 1996;30:817-24.
- [55] Kerkez Ö, Boz İ. Photo (electro) catalytic activity of Cu²⁺-modified TiO₂ nanorod array thin films under visible light irradiation. *Journal of Physics and Chemistry of Solids*. 2014;75:611-8.
- [56] Xu Y-h, Liang D-h, Liu D-z. Preparation and characterization of Cu₂O-TiO₂: efficient photocatalytic degradation of methylene blue. *Materials Research Bulletin*. 2008;43:3474-82.
- [57] Ebnasajjad S. Surface and material characterization techniques. *Handbook of Adhesives and Surface Preparation*: Elsevier; 2011. p. 31-48.
- [58] Ferraro JR. *Introductory raman spectroscopy*: Elsevier; 2003.
- [59] De Faria D, Venâncio Silva S, De Oliveira M. Raman microspectroscopy of some iron oxides and oxyhydroxides. *Journal of Raman spectroscopy*. 1997;28:873-8.
- [60] Rekhila G, Bessekhoud Y, Trari M. Visible light hydrogen production on the novel ferrite NiFe₂O₄ 2013.
- [61] Orazem ME, Tribollet B. Electrochemical impedance spectroscopy. *Angew Chem Int Ed*. 2009;48:1532-4.

- [62] Govindhan P, Pragathiswaran C, Chinnadurai M. A magnetic Fe₃O₄ decorated TiO₂ nanoparticles application for photocatalytic degradation of methylene blue (MB) under direct sunlight irradiation. *Journal of Materials Science: Materials in Electronics*. 2018;29:6458-69.
- [63] Nabiyouni G, Fesharaki MJ, Zolotovskiy A. Preparation, magnetic studies and band structure calculation of NiFe₂O₄ nanoparticles. *Task Quart*. 2010;15:107-19.
- [64] He Z, Xia Y, Tang B, Su J. Fabrication and photocatalytic property of magnetic NiFe₂O₄/Cu₂O composites. *Materials Research Express*. 2017;4:095501.
- [65] Chen H-W, Ku Y, Kuo Y-L. Effect of Pt/TiO₂ characteristics on temporal behavior of o-cresol decomposition by visible light-induced photocatalysis. *Water Research*. 2007;41:2069-78.
- [66] Balkanski M, de Cerqueira Leite RC, Porto SP. *Proceedings of the Third International Conference on Light Scattering in Solids, Campinas, Brazil, July 25-30, 1975: Flammarion Medecine-Sciences; 1976.*
- [67] Dunnwald J, Otto A. The application of Ramon spectroscopy to the study of atmo-spheric rust systems. *Corros Sci*. 1989;1167.
- [68] Hu Y, Liu Y, Qian H, Li Z, Chen J. Coating colloidal carbon spheres with CdS nanoparticles: microwave-assisted synthesis and enhanced photocatalytic activity. *Langmuir*. 2010;26:18570-5.
- [69] Chihaoui S, Koubaa M, Cheikhrouhou-Koubaa W, Cheikhrouhou A, Guermazi H. Effect of Ni doping on the structural, vibrational, optical and magnetic properties of YMnO₃. 4FeO₃. 6-xNi_xO₃ (0 ≤ x ≤ 0.1) nanoparticles. *Journal of Alloys and Compounds*. 2019;771:327-34.
- [70] Gao X, Liu X, Zhu Z, Wang X, Xie Z. Enhanced photoelectrochemical and photocatalytic behaviors of MFe₂O₄ (M = Ni, Co, Zn and Sr) modified TiO₂ nanorod arrays 2016.
- [71] Alam M, Cameron D. Investigation of annealing effects on sol-gel deposited indium tin oxide thin films in different atmospheres. *Thin Solid Films*. 2002;420:76-82.
- [72] Boratto MH, Congiu M, dos Santos SB, Scalvi LV. Annealing temperature influence on sol-gel processed zirconium oxide thin films for electronic applications. *Ceramics International*. 2018;44:10790-6.
- [73] Chen H, Chen N, Feng C, Gao Y. Synthesis of a novel narrow-band-gap iron (II, III) oxide/titania/silver silicate nanocomposite as a highly efficient and stable visible light-driven photocatalyst. *Journal of colloid and interface science*. 2018;515:119-28.
- [74] Wang X, Lizong D. Well-dispersed zero-valent iron supported on Fe₃O₄/gC₃N₄ composites via a facile approach with versatile photoredox catalysis. *Journal of Nanoparticle Research*. 2018;20:317.
- [75] Kezzim A, Nasrallah N, Abdi A, Trari M. Visible light induced hydrogen on the novel hetero-system CuFe₂O₄/TiO₂. *Energy Conversion and Management*. 2011;52:2800-6.
- [76] Schwertmann U, Cambier P, Murad E. Properties of goethites of varying crystallinity. *Clays and Clay minerals*. 1985;33:369-78.
- [77] Xuan S, Jiang W, Gong X, Hu Y, Chen Z. Magnetically separable Fe₃O₄/TiO₂ hollow spheres: fabrication and photocatalytic activity. *The Journal of Physical Chemistry C*. 2008;113:553-8.
- [78] Azeez F, Al-Hetlani E, Arafa M, Abdelmonem Y, Nazeer AA, Amin MO, et al. The effect of surface charge on photocatalytic degradation of methylene blue dye using chargeable titania nanoparticles. *Scientific reports*. 2018;8.
- [79] Yao YR, Huang WZ, Zhou H, Yin HY, Zheng YF, Song XC. A novel Fe₃O₄@ SiO₂@ BiOBr photocatalyst with highly active visible light photocatalytic properties. *Materials Chemistry and Physics*. 2014;148:896-902.
- [80] Lee KM, Lai CW, Ngai KS, Juan JC. Recent developments of zinc oxide based photocatalyst in water treatment technology: a review. *Water research*. 2016;88:428-48.
- [81] Channei D, Phanichphant S. Fe₃O₄/SiO₂/CeO₂ core-shell magnetic nanoparticles as photocatalyst. *J Nanosci Nanotechnol*. 2014;14:7756-62.

- [82] Shen J, Li X, Huang W, Li N, Ye M. One-pot polyelectrolyte assisted hydrothermal synthesis of NiFe₂O₄-reduced graphene oxide nanocomposites with improved electrochemical and photocatalytic properties. *Journal of Materials Research*. 2014;29:2211-9.
- [83] Santhosh C, Malathi A, Daneshvar E, Kollu P, Bhatnagar A. Photocatalytic degradation of toxic aquatic pollutants by novel magnetic 3D-TiO₂@ HPGA nanocomposite. *Scientific reports*. 2018;8:15531.
- [84] Jiang W, Zhang X, Gong X, Yan F, Zhang Z. Sonochemical synthesis and characterization of magnetic separable Fe₃O₄-TiO₂ nanocomposites and their catalytic properties. *International Journal of Smart and Nano Materials*. 2010;1:278-87.
- [85] Fisli A, Saridewi R, Dewi SH, Gunlazuardi J. Preparation and characterization of Fe₃O₄/TiO₂ composites by heteroagglomeration. *Advanced Materials Research: Trans Tech Publ*; 2013. p. 131-7.
- [86] Rana S, Srivastava R, Sorensson M, Misra R. Synthesis and characterization of nanoparticles with magnetic core and photocatalytic shell: anatase TiO₂-NiFe₂O₄ system. *Materials Science and Engineering: B*. 2005;119:144-51.
- [87] Joo J, Ye Y, Kim D, Lee J, Jeon S. Magnetically recoverable hybrid TiO₂ nanocrystal clusters with enhanced photocatalytic activity. *Materials Letters*. 2013;93:141-4.
- [88] Sunkara B, Misra R. Enhanced antibactericidal function of W⁴⁺-doped titania-coated nickel ferrite composite nanoparticles: a biomaterial system. *Acta Biomaterialia*. 2008;4:273-83.
- [89] Cheng P, Li W, Zhou T, Jin Y, Gu M. Physical and photocatalytic properties of zinc ferrite doped titania under visible light irradiation. *Journal of Photochemistry and Photobiology A: Chemistry*. 2004;168:97-101.

ÖZGEÇMİŞ

Adı Soyadı: SEDA YILMAZ

Doğum Yeri: İSTANBUL

Yabancı Dil: İngilizce

E-Posta: seda.ylmz.sd@gmail.com

sedadavulcu@gmail.com

Öğrenim Durumu:

Derece	Bölüm/Program	Üniversite/Lise	Mezuniyet Yılı
Lise	Anadolu	İstanbul Atatürk Anadolu Lisesi	2011
Üniversite	Kimya Mühendisliği	Marmara Üniversitesi	2016

Bilimsel Eserler:

Ulusal Dergilerde Yayımlanan Makale Bilgileri

1. DUYGU AKYÜZ, RANA MUHAMMED ZUNAİN AYAZ, SEDA YILMAZ, ÖZLEM UĞUZ, CEVAT SARIOĞLU, FATMA KARACA, ALİ RIZA ÖZKAYA, ATIF KOCA, METAL CHALCOGENIDE BASED PHOTOCATALYSTS WITH HETEROATOM LOAD REDUCED GRAPHENE OXIDE FOR PHOTOCATALYTIC AND PHOTOELECTROCHEMICAL HYDROGEN PRODUCTION, INTERNATIONAL JOURNAL OF HYDROGEN ENERGY,2019

Ulusal Konferans Bilgileri

1. **SEDA YILMAZ**, ÖZGE KERKEZ KUYUMCU, DUYGU AKYÜZ, RANA MUHAMMED ZUNAİN AYAZ, ATIF KOCA, (2019), PHOTO(ELECTRO)CATALYTIC ACTIVITY OF THE MAGNETICALLY MODIFIED TiO₂ NANOPARTICLES, INTERNATIONAL CONFERENCE ON SUSTAINABLE ENERGY AND ENERGY CALCULATIONS (ICSEEC), Muğla, TURKEY.
2. **SEDA YILMAZ**, ÖZGE KERKEZ KUYUMCU, DUYGU AKYÜZ, RANA MUHAMMED ZUNAİN AYAZ, ATIF KOCA, (2019), SYNTHESIS OF MAHGNETICALLY SEPARABLE VISIBLE LIGHT DRIVEN PHOTOCATALYSTS FOR H₂ GENERATION, INTERNATIONAL HYDROGEN TECNOLOGIES CONGRESS (IHTEC), Edirne, TURKEY

